Azerbaijan Technical University

MACHINE SCIENCE
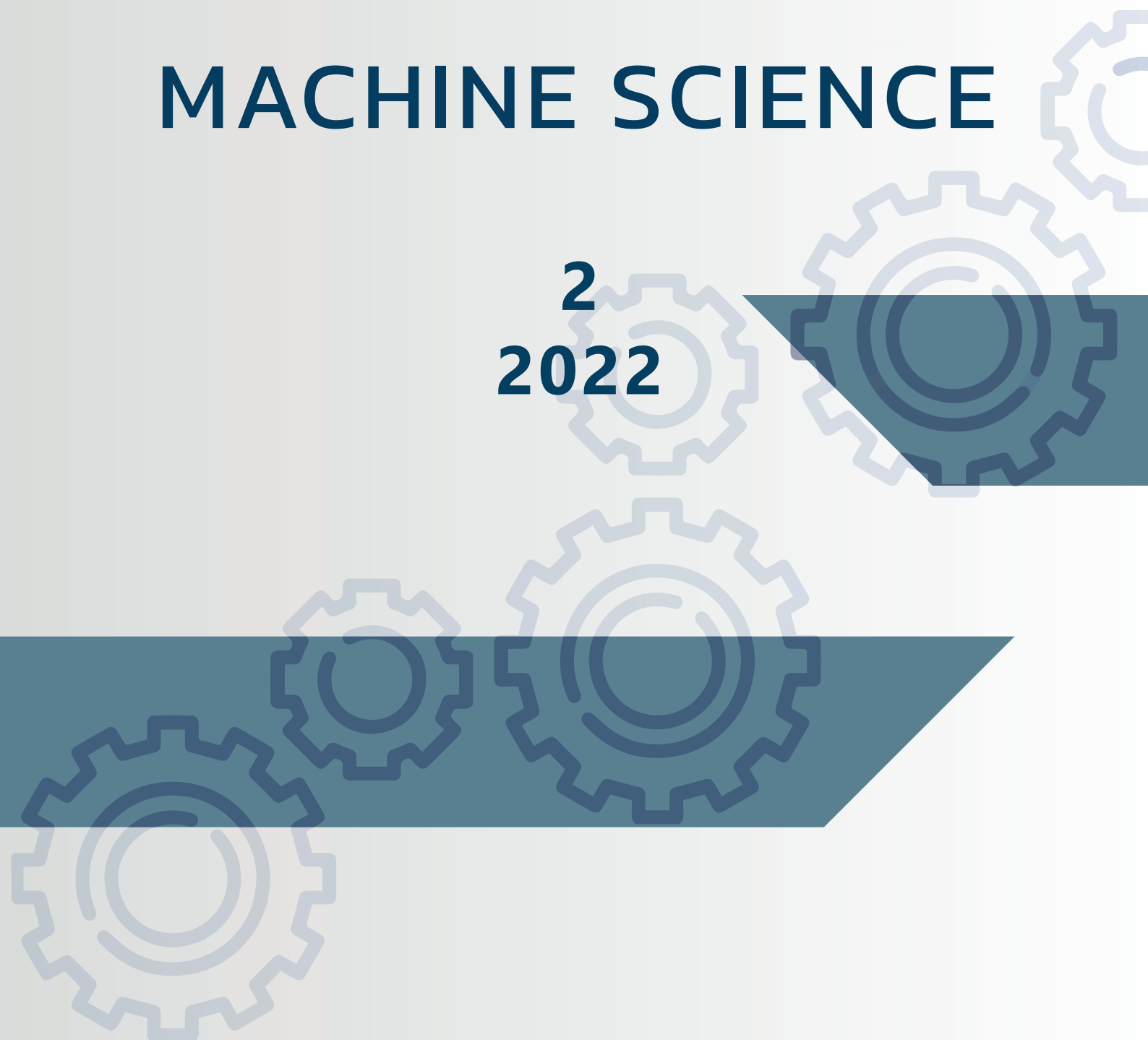
2
2022

International scientific–technical journal

Editorial address: *Redaksiyanın ünvanı:* *Адрес редакции:*	Baku, AZ1073, H.Javid ave., 25. AzTU Tel: (+994 12) 539 12 25 E-mail: msj@aztu.edu.az	© Machine Science, 2022 **ISSN:** 2227-6912 **E-ISSN:** 2790-0479

Contents 3

FINITE DIFFERENCE METHOD FOR STATIC AND DYNAMIC ANALYSIS: EULER-BERNOULLI BEAM ON WINKLER FOUNDATION AND VIBRATING MOTION OF SINGLE DEGREE OF FREEDOM SYSTEM

Gülçin TEKİN[1*], Fethi KADIOĞLU[2]

[1*]Department of Civil Engineering, Yıldız Technical University, Davutpaşa Campus, Istanbul, Turkey
[2]Department of Civil Engineering, Istanbul Technical University, Ayazağa Campus, Istanbul, Turkey

E-mail: gulcint@yildiz.edu.tr [1], fkadioglu@itu.edu.tr [2]

Abstract: The Finite Difference Method (FDM) is one of the most powerful numerical solution techniques and has the ability to handle most types of analysis in structural mechanics. In this study, examples of physical modeling of vibrational motion of a single-degree-of-freedom-system (SDOF) under the effect of a harmonic external load are examined by considering the effects of different system parameters. In its simplest form, the problem is represented by a second order differential equation with constant coefficient. The relevant equation is solved analytically and at the same time, the compatibility of the results is tested using the finite-difference method. In addition, the analysis of the beam resting on the elastic foundation is considered. The analytical solution of the fourth order differential equation is obtained and the finite-difference method is used in order to obtain its numerical solution. Different numerical example problems are considered for the above mentioned two problems and the results are tested with the existing literature.

Keywords: *Finite-difference method, Beam-foundation interaction, Vibration, Numerical solution, Analytical Solution*

Introduction. In numerical analysis, the finite difference approximations of derivatives are simple, of rapid convergence and accurate to solve differential equations of which their analytical solutions are difficult or impossible to find. Finite difference methods (FDMs) transform partial differential equations (pdes) into a system of linear algebraic equations. In the FDMs, discrete approximations are used for the derivatives in the differential equation. These approximations are derived from the Taylor series expansions. Three of the approximations are Forward, Backward and Central differences. Commonly, the central difference formula is used due to fact that it yields better accuracy. The error for the central difference difference decreases quadratically as the step size decreases whereas for the forward/backward schemes the decrease is linear. The finite difference approximations relate the value of the dependent variable at a point in the solution region to its values at the neighboring points. The solution region is divided into *n* subintervals of length "*h*". In to get a good approximation, step size should be sufficiently small. Large step size increases simulation speed in practice, but create instabilities.

In engineering, beams are fundamental components and are widely used as an accurate and simple model for analysis of complex engineering structures. This study aims to investigate the analytic and the numerical solution of beam-type structures which are resting on an elastic foundation. For numerical solution, the FDM is used.

The first important studies on the behavior of elastic foundation presented by Winkler [1] in 1867 and as a result of these studies, Winkler hypothesis has been revealed. The Winkler model is most commonly used in practice, since the soil behavior is represented with a very simple approach. The general idea of the hypothesis is based on the fact that the foundation consists of infinitely close, elastic and linear springs. Under the effect of the uniformly distributed load, the ground reaction force is formulated briefly as follows:

$$q(z) \,=\, -kv(z)$$

where the spring coefficient "k" is known as the subgrade reaction coefficient. According to this hypothesis, the foundation reaction at any point of the elastic and prismatic beam under the influence of various loads is proportional to the deflection value at the same point of the beam under consideration. Here, q(z) is the reaction of the elastic foundation and v(z) is the displacement in the vertical direction. Assumption of the Winkler hypothesis is that a force acting on the foundation causes deformation only at the point where it acts. In other words, Winkler considered the elastic foundation as a system of vertical springs that are not affected by each other, are infinitely close to each other and can move freely by compression. In Winkler's model, the only parameter that shows the character of the foundation is the parameter "k". For this reason, the Winkler model is also referred to as a single parameter foundation model.

Many beam theories have been developed based on various assumptions. The simplest and the most commonly used by researchers is named as Euler-Bernoulli beam theory with the following kinematic assumptions: the cross-section is infinitely rigid in its own plane, the cross-section of a beam remains plane and normal to the deformed axis of the beam after deformation.

A large number of studies can be found in the literature on the analysis of beams with various theories and geometries. However, during the past two decades, the researcher's attention has been drawn increasingly to the beam-foundation interaction problems. Develi [2] has investigated the vibration problem for a finite length of Timoshenko beam on Vlasov foundation and Winkler foundation. In this study, the elastic curve function is obtained from the differential equations of the beam. Comparison is made for Timoshenko beam and Euler-Bernoulli beam and it is observed that the displacement, shear force and bending moment values are close to each other. Eisenberger and Bielak [3] have considered externally loaded free-end beams on a two-parameter elastic foundation. It has been observed that the interaction with foundation depends on the beam length, the bending stiffness of the beam and the foundation stiffness parameters. Ike [4] considered Euler-Bernoulli beams on Winkler foundation by the point collocation method. The beams subjected to uniformly distributed loads are considered. It is observed that the values of deflection and bending moment at the mid-point of the beam decreased with the increase of the subgrade reaction modulus. Doğan [5] has examined the homogeneous and non-homogeneous conditions of foundation for weightless beams. In the numerical solutions, different loading types and foundation coefficients are considered. Sign changes for vertical displacement are observed in the samples examined for tension and compression conditions. Karamahmutoğlu [6] focused on the analysis of sheet- pile walls and beams on elastic foundation by using the finite-difference method. The Winkler foundation model is used as the foundation model. The results are compared with the available examples in the literature. Heteyni [7] worked on the Winkler foundation model. In this study, deflection and bending moment values are obtained for different points of finite and infinite beams under different loading conditions.

A further analysis is considered to discuss the dynamic response of a linear single-degree-of-freedom (SDOF) oscillator. Structures respond to earthquake excitation as either simple or complex oscillators. SDOF systems are used to represent the simple oscillators whereas multi-degree-of-freedom (MDOF) systems are used to represent complex oscillators.The motion of the linear SDOF system under harmonic load is solved analytically and also the FDM is used to determine the displacement response time histories of linear SDOF systems. Various studies in the earthquake engineering literature devoted to the dynamic response analysis of systems under different types of dynamic loads [8-12].

Methodology.
Central Finite-Difference Method
The Taylor Series of a real or complex f(z) function with any order derivative, in the range ($a-r$, $a+r$), where 'a' is a real or complex number, is defined as:

$$f\ a\ +f'\ a\ \ z-a\ +\frac{f\ ^{2}\ z}{2!}\ z-a\ ^{2}+...+\frac{f\ ^{n}\ z}{n!}\ z-a\ ^{n} \tag{1}$$

If f(z) function is expanded using the Taylor Series at the points $z_{i-1} = z_i - \Delta z$ and $z_{i+1} = z_i + \Delta z$, the following equations are obtained:

$$f\ z_{i-1}\ =f\ z_i\ -f'\ z_i\ \Delta z+\frac{f\ ^{2}\ z_i}{2!}\ \Delta z\ ^{2}-\frac{f\ ^{3}\ z_i}{3!}\ \Delta z\ ^{3}+\frac{f\ ^{4}\ z_i}{4!}\ \Delta z\ ^{4}+... \tag{2}$$

$$f\ z_{i+1}\ =f\ z_i\ +f'\ z_i\ \Delta z+\frac{f\ ^{2}\ z_i}{2!}\ \Delta z\ ^{2}+\frac{f\ ^{3}\ z_i}{3!}\ \Delta z\ ^{3}+\frac{f\ ^{4}\ z_i}{4!}\ \Delta z\ ^{4}+... \tag{3}$$

These expressions can be arranged as follows:

$$f_{i-1} = f_i - f_i'\Delta z+\frac{f_i^{2}}{2!}\ \Delta z\ ^{2}-\frac{f_i^{3}}{3!}\ \Delta z\ ^{3}+\frac{f_i^{4}}{4!}\ \Delta z\ ^{4}+... \tag{4}$$

$$f_{i+1} = f_i + f_i'\Delta z+\frac{f_i^{2}}{2!}\ \Delta z\ ^{2}+\frac{f_i^{3}}{3!}\ \Delta z\ ^{3}+\frac{f_i^{4}}{4!}\ \Delta z\ ^{4}+... \tag{5}$$

Subtracting (4) from (5) and considering the first three terms on the right, the first derivative expression for the z_i point is obtained as follows:

$$f_i' = \frac{f_{i+1} - f_{i-1}}{2\ \Delta z} \tag{6}$$

Again, if the expressions (4) and (5) are added side by side and the first three terms are considered, the second derivative expression for the z_i point is obtained as follows:

$$f_i^{(2)} = \frac{f_{i-1} - 2f_i + f_{i+1}}{\Delta z\ ^{2}} \tag{7}$$

Let's expand the funciton f(z) into the series at the points $z_{i-2} = z_i - 2\Delta z$ and $z_{i+2} = z_i + 2\Delta z$:

$$f\ z_{i-2}\ =f\ z_i\ -f'\ z_i\ 2\Delta z+\frac{f\ ^{2}\ z_i}{2!}\ 2\Delta z\ ^{2}-\frac{f\ ^{3}\ z_i}{3!}\ 2\Delta z\ ^{3}+\frac{f\ ^{4}\ z_i}{4!}\ 2\Delta z\ ^{4}+... \tag{8}$$

$$f\ z_{i+2}\ =f\ z_i\ +f'\ z_i\ 2\Delta z+\frac{f\ ^{2}\ z_i}{2!}\ 2\Delta z\ ^{2}+\frac{f\ ^{3}\ z_i}{3!}\ 2\Delta z\ ^{3}+\frac{f\ ^{4}\ z_i}{4!}\ 2\Delta z\ ^{4}+... \tag{9}$$

The arranged version of these expressions is:

$$f_{i-2} = f_i - f_i'\,2\Delta z+\frac{f_i^{2}}{2!}\ 2\Delta z\ ^{2}-\frac{f_i^{3}}{3!}2\ \Delta z\ ^{3}+\frac{f_i^{4}}{4!}\ 2\Delta z\ ^{4}+... \tag{10}$$

$$f_{i+2} = f_i + f_i'\,2\Delta z+\frac{f_i^{2}}{2!}\ 2\Delta z\ ^{2}+\frac{f_i^{3}}{3!}\ 2\Delta z\ ^{3}+\frac{f_i^{4}}{4!}\ 2\Delta z\ ^{4}+... \tag{11}$$

The expression (4) is multiplied by (-2), and the expression (5) is multiplied by (+2) and added side by side and considering the first five terms:

$$-2f_{i-1}+2f_{i+1} = 4f_i'+4\frac{f_i^{3}}{3!}\ \Delta z\ ^{3} \tag{12}$$

The expression (10) is multiplied by (-1), and the expression (11) by (+1) and summed side by side and considering the first five terms:

$$-f_{i-2} + f_{i+2} = 2f_i' \ 2\Delta z \ + 2\frac{f_i^{\ 3}}{3!} \ 2\Delta z^{\ 3} \tag{13}$$

If (12) is subtracted from the expression (2.13), the third derivative expression for the z_i point is obtained as follows:

$$f_i^{(3)} = \frac{-f_{i-2} + 2f_{i-1} - 2f_{i+1} + f_{i+2}}{2 \ \Delta z^{\ 3}} \tag{14}$$

If (4) and (5) expressions are multiplied by (+4) and summed side by side and the first five terms are considered:

$$4f_{i-1} + 4f_{i+1} = 8f_i + 8\frac{f_i^{\ 2}}{2!} \ \Delta z^{\ 2} + 8\frac{f_i^{\ 4}}{4!} \ \Delta z^{\ 4} \tag{15}$$

The expressions (10) and (11) are summed side by side and the first five terms are considered:

$$f_{i-2} + f_{i+2} = 2f_i + 2\frac{f_i^{\ 2}}{2!} \ 2\Delta z^{\ 2} + 8\frac{f_i^{\ 4}}{4!} \ 2\Delta z^{\ 4} \tag{16}$$

If (16) is subtracted from (15), the fourth derivative expression for the z_i point is obtained as follows:

$$f_i^{(4)} = \frac{f_{i-2} - 4f_{i-1} + 6f_i - 4f_{i+1} + f_{i+2}}{\Delta z^{\ 4}} \tag{17}$$

Analytical Solution of Euler-Bernoulli Beam on Elastic Foundation

The fourth-order differential equation for the Euler-Bernoulli beam on the Winkler foundation (see Figure 1) can be expressed as:
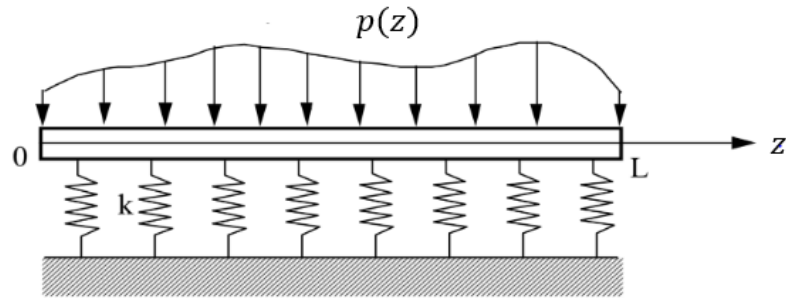
Fig. 1. Beam–elastic foundation interaction

$$EI_x \frac{d^4v}{dz^4} + kv \ z \ = p \ z \tag{18}$$

where E is the modulus of elasticity (Young's modulus) of the beam material, I_x is the moment of inertia of the section about the x-axis, k is the subgrade reaction coefficient (Winkler's modulus), $p(z)$ is the distributed load applied to the beam.

Firstly, the homogeneous solution of the differential equation is obtained as follows:

$$v_h \ z \ = e^{\beta z} \left[c_1 \cos \ \beta z \ + c_2 \cos \ \beta z \right] + e^{-\beta z} \left[c_3 \cos \ \beta z \ + c_4 \sin \ \beta z \right] \tag{19}$$

where c_1, c_2, c_3 and c_4 are integration constants and β is a problem constant in units of (1/m) calculated from the following relation:

$$\beta = \sqrt[4]{\frac{k}{4EI_x}} \tag{20}$$

The particular solution depends on the load and it is given as follows for the uniformly distributed load:

$$v_p\ z\ = \frac{p}{k} \tag{21}$$

Now the general solution is the sum of the homogeneous and particular solutions as follows:

$$v_g\ z\ = \frac{p}{k} + e^{\beta z}\left[c_1\cos\ \beta z\ + c_2\cos\ \beta z\ \right] + e^{-\beta z}\left[c_3\cos\ \beta z\ + c_4\sin\ \beta z\ \right] \tag{23}$$

In order to determine the constants c_1, c_2, c_3 and c_4, it is necessary to use to the boundary conditions of the beam. In a simply supported finite beam with a length of L, the boundary conditions can be written as: $v(z=0) = 0$, $v(z=L) = 0$ and $v^{(2)}(z=0) = 0$, $v^{(2)}(z=L) = 0$. If the boundary conditions are adapted to Equation (2.23), the integration constants c_1, c_2, c_3 and c_4 can be obtained as follows:

$$c_1 = -\frac{p\left[\sin\ \beta L\ ^2 - \cos\ \beta L\ + \cos\ \beta L\ e^{\beta L} - \cos\ \beta L\ e^{-\beta L} + \cos\ \beta L\ ^2 e^{-2\beta L} + \sin\ \beta L\ ^2 e^{-2\beta L}\right]}{k\left[\cos\ \beta L\ ^2 e^{-2\beta L} + \cos\ \beta L\ ^2 e^{2\beta L} + \sin\ \beta L\ ^2 e^{-2\beta L} + \sin\ \beta L\ ^2 e^{2\beta L} - 2\cos\ \beta L\ ^2 + 2\sin\ \beta L\ ^2\right]} \tag{24}$$

$$c_2 = -\frac{p\left[\sin\ \beta L\ e^{\beta L} - 2\cos\ \beta L\ \sin\ \beta L\ + \sin\ \beta L\ e^{-\beta L}\right]}{k\left[\cos\ \beta L\ ^2 e^{-2\beta L} + \cos\ \beta L\ ^2 e^{2\beta L} + \sin\ \beta L\ ^2 e^{-2\beta L} + \sin\ \beta L\ ^2 e^{2\beta L} - 2\cos\ \beta L\ ^2 + 2\sin\ \beta L\ ^2\right]} \tag{25}$$

$$c_3 = -\frac{p\left[\sin\ \beta L\ ^2 - \cos\ \beta L\ ^2 - \cos\ \beta L\ e^{\beta L} + \cos\ \beta L\ e^{-\beta L} + \cos\ \beta L\ ^2 e^{2\beta L} + \sin\ \beta L\ ^2 e^{2\beta L}\right]}{k\left[\cos\ \beta L\ ^2 e^{-2\beta L} + \cos\ \beta L\ ^2 e^{2\beta L} + \sin\ \beta L\ ^2 e^{-2\beta L} + \sin\ \beta L\ ^2 e^{2\beta L} - 2\cos\ \beta L\ ^2 + 2\sin\ \beta L\ ^2\right]} \tag{26}$$

$$c_4 = -\frac{p\left[\sin\ \beta L\ e^{\beta L} - 2\cos\ \beta L\ \sin\ \beta L\ + \sin\ \beta L\ e^{-\beta L}\right]}{k\left[\cos\ \beta L\ ^2 e^{-2\beta L} + \cos\ \beta L\ ^2 e^{2\beta L} + \sin\ \beta L\ ^2 e^{-2\beta L} + \sin\ \beta L\ ^2 e^{2\beta L} - 2\cos\ \beta L\ ^2 + 2\sin\ \beta L\ ^2\right]} \tag{27}$$

When these constants are substituted into Equation (2.23) and simplified, the deflection at the mid-point of the beam obtained as follows:

$$v_m = \frac{p\left[1 - \dfrac{2\cos\left(\dfrac{\beta L}{2}\right)\cosh\left(\dfrac{\beta L}{2}\right)}{\cos(\beta L) + \cos(\beta L)}\right]}{k} \tag{28}$$

The bending moment at the mid-point of the beam is obtained as follows:

$$M_m = \frac{p}{2\beta^2}\frac{\sinh\left(\dfrac{\beta L}{2}\right)\sin\left(\dfrac{\beta L}{2}\right)}{\cos(\beta L) + \cos(\beta L)} \tag{29}$$

Analytical Solution of Forced Vibration of a SDOF

The mass "m (in kg)" shown in Figure 2, is connected to both spring and the dashpot, the reaction against the external force on the spring increases proportional to the displacement of the body from the equilibrium position, meanwhile the reaction at the dashpot increases with the velocity of the mass.

The second-order differential equation for the equation of motion can be expressed as:

$$m\ddot{x} + c\dot{x} + kx = F\ t \tag{30}$$

In order to obtain the general solution of the differential relation, firstly the homogenous solution must be obtained. Let's rewrite equation (30) by making right hand side equal to zero. For the homogenous solution, the below exponential function is proposed:

$$x = e^{\lambda t} \tag{31}$$

Substituting this expression and its derivatives yields:

$$e^{\lambda t}\ m\lambda^2 + c\lambda + k\ = 0 \tag{32}$$
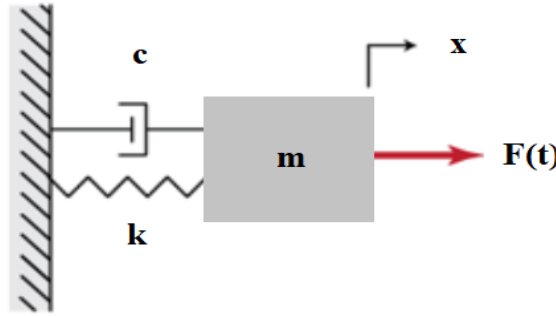
Fig. 2. Mass-spring-damper system
where F(t) is a time-dependent force in (N), k is the spring constant in (N/m), and c is the coefficient of the dashpot in (Ns/m).

Since $e^{\lambda t}$ can never be zero, a solution is possible provided $m\lambda^2 + c\lambda + k = 0$. Hence, two values of λ are:

$$\lambda_{1,2} = \frac{-c \pm \sqrt{c^2 - 4mk}}{2m} = -\frac{c}{2m} \pm \sqrt{\frac{c^2}{4m^2} - \frac{k}{m}} \tag{33}$$

Here the value which makes radical in (2.33) equal to zero is called critical damping coefficient, cc.

$$c_c = \sqrt{4mk} = 2\sqrt{mk} = 2m\omega_n \tag{34}$$

where ω_n is the natural circular frequency of vibration; its units are [rad/sec]. There are 3 possible combinations of λ_1 and λ_2 which must be considered. Here, ξ is defined as a damping ratio that is given as:

$$\xi = \frac{c}{c_c} \tag{35}$$

The cases of damping are categorized via ξ ;

• $\xi > 1$ or $c > cc$: Overdamped motion. The system turns back to its original position without oscillating.

- $\xi=1$ or $c=cc$: Critically damped motion. The system shows tendencies to come to equilibrium as quick as possible without oscillating.
- $\xi<1$ or $c<cc$: Underdamped motion. The system oscillates with a gradual decrements to zero.

Most engineering structures fall into this category $c<cc$. In this study, the system is considered as "underdamped". By considering a relationship between the mass, stiffness and damping ratio, revised versions of the equations in terms of the natural circular frequency and damping ratio can be formed as follows:

$$\ddot{x}+2\xi\omega_n\dot{x}+\omega_n^2 x=0 \tag{36}$$

and

$$\lambda_{1,2}=-\xi\omega_n\pm\sqrt{\xi\omega_n^2-\omega_n^2} \tag{37}$$

or

$$\lambda_{1,2}=-\xi\omega_n\pm\omega_n\sqrt{\xi^2-1} \tag{38}$$

Underdamped condition corresponds to the negative value of the quantity inside the square root which means that:

$$\lambda_{1,2}=-\xi\omega_n\pm i\omega_n\sqrt{1-\xi^2} \tag{39}$$

where, i is the complex number. And, $\omega_n\sqrt{1-\xi^2}=\omega_d$.

Substituting $\lambda_{1,2}$ values into $x=C_1 e^{\lambda_1 t}+C_2 e^{\lambda_2 t}$ where C_1 and $C2$ are arbitrary constants, the solution is:

$$x=e^{-\xi\omega_n t}\ C_1 e^{i\omega_d t}+C_2 e^{-i\omega_d t} \tag{40}$$

Equation (2.40) can be written as:

$$x=e^{-\xi\omega_n t}\ \cos\ \omega_d t\ C_1+C_2\ +\sin\ \omega_d t\ \ iC_1-iC_2 \tag{41}$$

by using $e^{i\theta}=\cos\theta+i\sin\theta$. If arbitrary constants are renamed as $B_1=C_1+C_2$ and $B_2=iC_1-iC_2$, homogenous part of the solution has become:

$$x_h=B_1 e^{-\xi\omega_n t}\cos\ \omega_d t\ +B_2 e^{-\xi\omega_n t}\sin\ \omega_d t \tag{42}$$

Homogenous solution will die out after a period of time due to friction. Let's suggest an external harmonic force has a form of $F(t)=F_0\sin(\Omega t)$. Here Ω is the angular velocity of mentioned force. The form of particular solution is,

$$x_p=A\sin\ \Omega t\ +B\sin\ \Omega t \tag{43}$$

By considering time derivatives of (2.43) and substituting $x_p, \dot{x}_p, \ddot{x}_p$ into the Equation (30) results in:

$$-Am\Omega^2-cB\Omega+kA\ \sin\ \Omega t\ +\ -Bm\Omega^2-cA\Omega+kB\ \cos\ \Omega t\ =F_0\sin\ \Omega t \tag{44}$$

The coefficients of $\sin(\Omega t)$ and $\cos(\Omega t)$ on each side of the equation must be equal to each other as follows:

$$-Am\Omega-cB\Omega+kA=F_0 \tag{45}$$

Gülçin TEKİN, Fethi KADIOĞLU
Finite difference method for static and dynamic analysis: Euler-Bernoulli beam on Winkler
foundation and vibrating motion of single degree of freedom system

$$-Bm\Omega^2 + cA\Omega + kB = 0 \tag{46}$$

As a result:

$$A = \frac{F_0 \; k - m\Omega^2}{k - m\Omega^2 \;^2 + \; \Omega c \;^2} \tag{47}$$

$$B = \frac{-F_0\Omega c}{k - m\Omega^2 \;^2 + \; \Omega c \;^2} \tag{48}$$

Recall, $x_g = x_h + x_p$

$$x \; t \; = B_1 e^{-\xi\omega_n t} \cos \; \omega_d t \; + B_2 e^{-\xi\omega_n t} \sin \; \omega_d t \; + A \sin \; \Omega t \; + B \cos \; \Omega t \tag{49}$$

As A and B parameters can be determined from known values, only unknowns are B_1 and B_2. Let initial conditions of the differential equation are $x(0) = x(0)$, and $\dot{x}(0) = \dot{x}(0)$

$$B_1 = x \; 0 \; - B \tag{50}$$

$$B_2 = \frac{\dot{x} \; 0 \; + \left[x \; 0 \; - B\right]\xi\omega_n - A\Omega}{\omega_d} \tag{51}$$

This is the general solution of the forced vibration of SDOF systems.

Numerical Examples and Discussion.
In this section, the first two examples are considered for the Euler-Bernoulli beam-elastic foundation interaction problems. And the last two examples are considered in order to discuss the effects of different parameters of the system on the vibration behavior. In order to show the efficiency of the FDM numerical solution technique, the analytical results are compared with the results of FDM.

Example 1
Vertical displacement and bending moment values at the mid-point of a simply supported beam under uniformly distributed load and resting on an elastic foundation are calculated analytically and the results are compared with the reference study in the literature and the results of FDM.

Properties of the cross-section of the beam;
$EI_x = 1,89 \times 10^6$ kNm^2
Foundation parameter;
$k = 6,92 \times 10^3$ t/m^2

The comparison results of the deflection and bending moment with the reference study [4] and the FDM are presented in Table 1. In order to use the central finite difference method for the solution, the beam is divided into four equal sub-intervals. By considering the boundary conditions of the simply supported beam, the sets of algebraic equations are constructed and unknowns are calculated. The maximum deflection value is also calculated by using the FDM. As seen from the following table, the results are close enough. The FDM gives satisfactory results with using large step size and saving time.

Table 1. The values of deflection and bending moment for the mid-point of the beam resting on elastic foundation

	v_{max} [m]	M_{max} [kNm]
Reference Study [4]	1,36 x 10^{-3}	23,9
Analytical Result	1,42 x 10^{-3}	23,7
FDM	1,20 x 10^{-3}	

Example 2

The variation of the deflection values at the midpoint for different subgrade reaction coefficients is discussed. The simply supported beam under the effect of uniformly distributed load resting on the elastic foundation is considered.

Properties of the cross-section of the beam;

$EI_x = 1,89 \times 10^6$ kNm^2

Foundation parameters;

$k_1 = 6 \times 10^3$ t/m^2 $k_2 = 12 \times 10^3$ t/m^2 $k_3 = 25 \times 10^3$ t/m^2

Midpoint deflection values are calculated for three different foundation parameters and the results are shown in Table 2. As expected, the deflection values decreased as the foundation stiffness increased.

Table 2. Deflection values for different coefficient of subgrade reaction

k (t/m^2)	6000	12000	25000
$v_{max}(m)$	$1,59 \times 10^{-3}$	$0,89 \times 10^{-3}$	$0,45 \times 10^{-3}$

Example 3

The external harmonic force $F(t) = 100 \cos(11t)$ N is applied to a stationary $150\ kg$ block is attached to the wall with the spring which has a $15\ kN/m$ spring constant and also connected to a dashpot which has $150\ Ns/m$ damping coefficient. Show graphically the convergence of FDM at the first 10 seconds for different time intervals as: $\Delta t = 0.02\ , 0.005\ s$ and $\Delta t = (0.1\ T) = 0.06283\ s$.

Initial conditions are, $x(0) = \dot{x}(0) = 0$
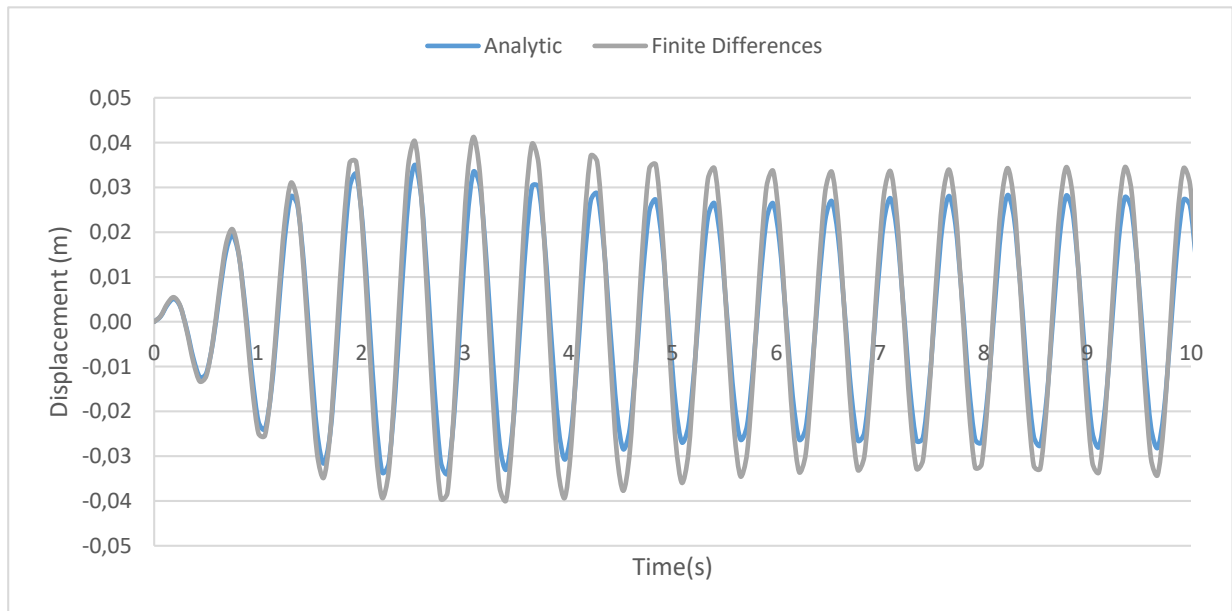
Fig. 3. Outputs of numerical solution versus analytic solution for $\Delta t = 0.1\ T$

It is obvious in Figure 3 that $\Delta t = 0.1\ T$ is not enough and time interval must be decreased to have better results. Now the analysis is performed for time interval $\Delta t = 0.02\ s$ and it is expected that the numerical analysis results to be more precise.
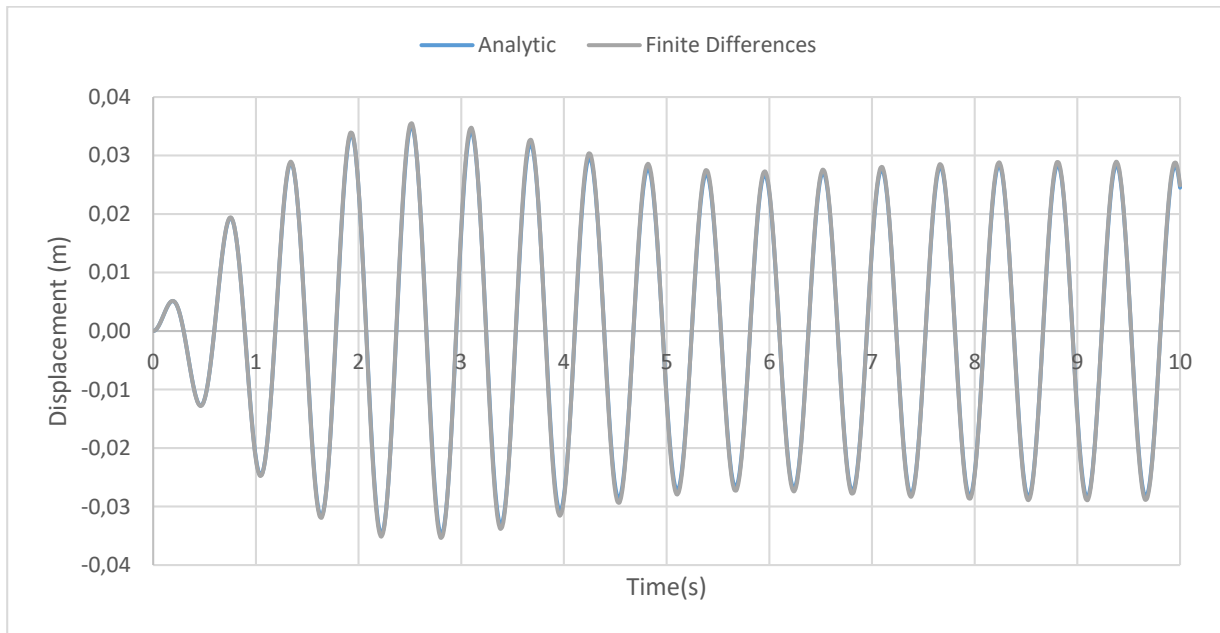
Fig. 4. Outputs of numerical solutions versus analytic solution for Δt = 0.02 s

When compared to $\Delta t = 0.1\,T$, we can say that the obtained displacements are quite precise as expected.

Although the analytical method gives the result exactly, it is understood that a numerical analysis can lead us to almost the same result performing simple analysis.
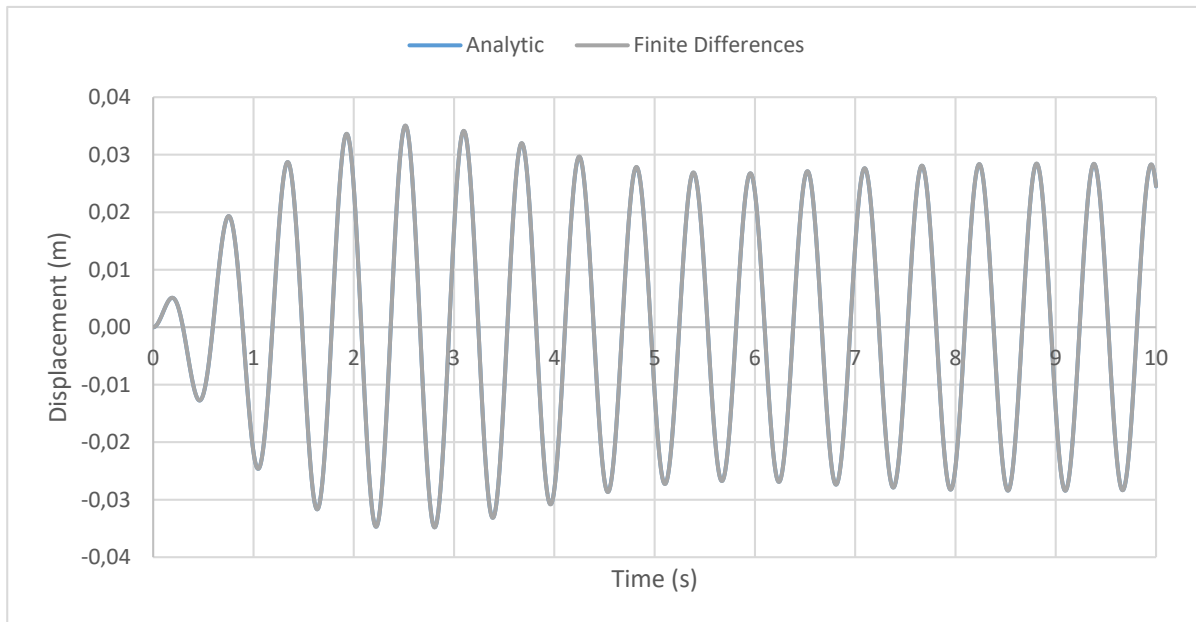
Fig. 5. Outputs of numerical solutions versus analytic solution for Δt = 0.005 s

Example 4

This example is considered in order to examine the effect of change in system period (*T*=1,1.5 and 2 s.) on the behavior of the vibrating system. In order to change the system's period, mass is going to be constant, but spring constant will change.
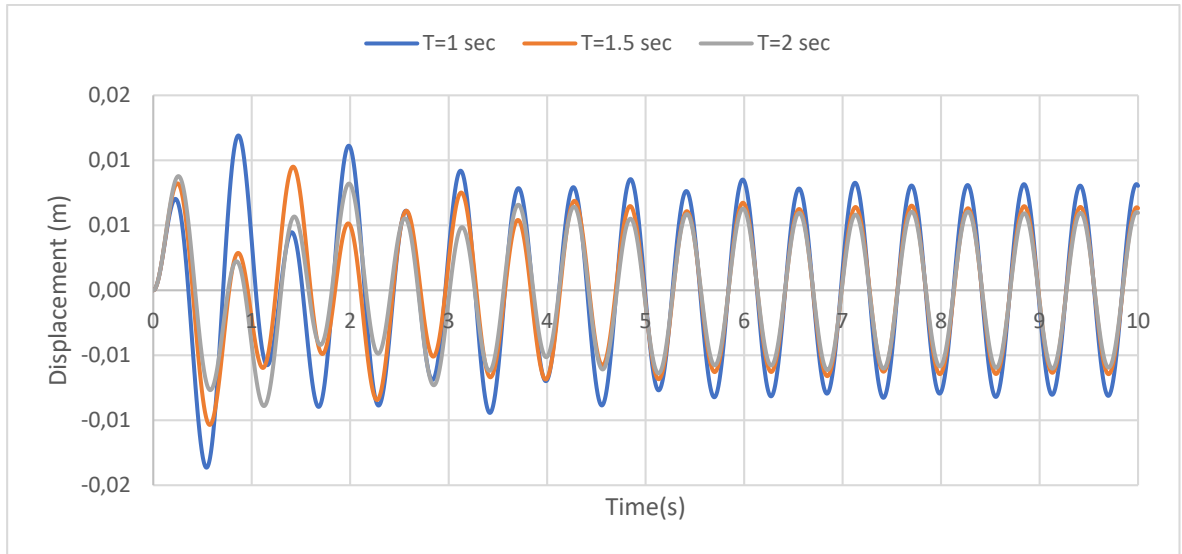
Fig. 6. Change of displacement for T=1, T=1.5 and T=2 seconds

As we expected, when the period increases, displacements are decreased.

Example 5

In this example, the behaviour of vibration of the system is analysed for different damping ratios as $\xi = 0.03$, $\xi = 0.5$ and $\xi = 0.9$. Let $\xi < 1$, as we investigated for underdamped system. Here, only the parameter c will be changed.

As the damping ratio increases, the amplitude of the vibration motions is decreased. In accordance with the definition of damping, increasing the damping coefficient leads to faster damping of the system and decreased displacement values.
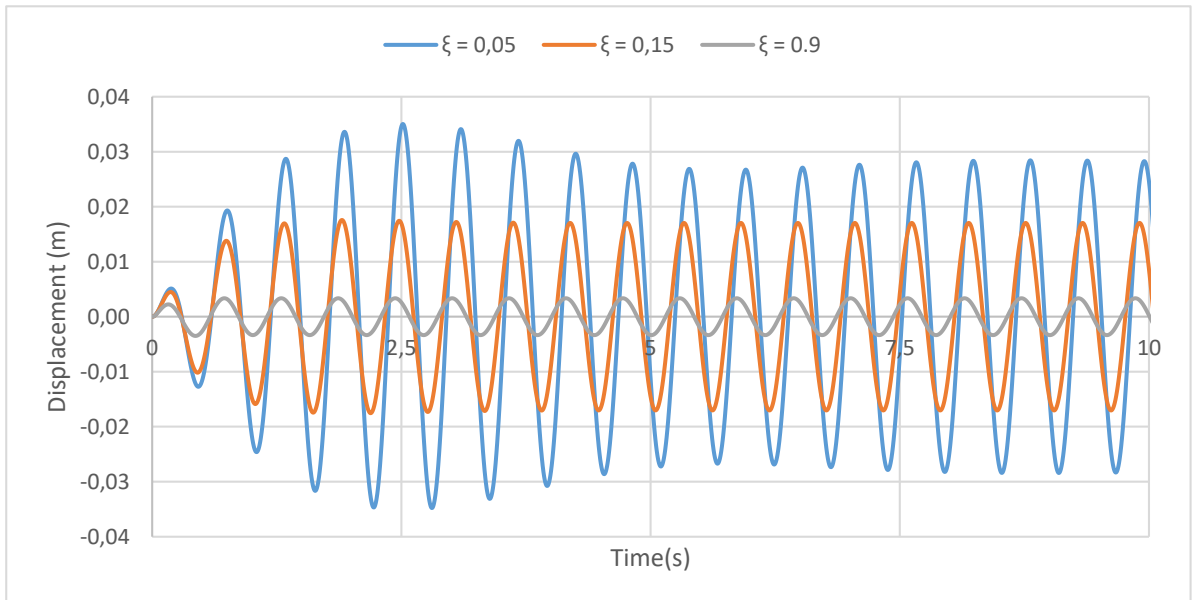
Fig. 7. Effect of different damping ratios as $\xi = 0.05$, $\xi = 0.15$ and $\xi = 0.9$

Conclusion. In this study, Euler-Bernoulli beam resting on elastic foundation is analyzed analytically and numerically by using the FDM. The maximum deflection and bending moment values are calculated for uniformly loaded simply supported beam and the results are compared with the literature. Sufficiently convergent results are obtained. In addition, the deflection values at the

mid-point of the beam are found for different subgrade modulus. As expected, when the subgrade reaction coefficient increased, the vertical displacement value at the midpoint of the beam decreased. In addition, vibrational motion analysis of a SDOF system under the effect of a harmonic external load is examined by considering the effects of different system parameters. An analytical solution of the problem is obtained in addition to the its numerical solution. In order to get a good approximation in FDM, step size should be sufficiently small. When the period of the system increases due to the change of the spring constant, the displacements are decreased as expected. In addition, it is observed that the displacements decrease in case the damping ratio increases.

REFERENCES

[1] Winkler, E. *Die Lehre von der Elastızıtat und Festiigkeit*. 1867, Prague.

[2] Develi, A. G.. *Elastik Zemin Üzerine Oturan Timoshenko Kirişinde Titreşim Problemi*. 2007, (Doctoral dissertation, Fen Bilimleri Enstitüsü).

[3] Eisenberger, M., and Bielak, J. *Finite beams on infinite two-parameter elastic foundations.* Computers & structures, 1992, 42(4), pp. 661-664.

[4] Ike, C.C. *Point collocation method for the analysis of Euler-Bernoulli beam on Winkler foundation.* International Journal of Darshan Institute on Engineering Research and Emerging Technologies (IJDI-ERET), 2018, 7(2), pp. 1-7.

[5] Doğan, O. *Elastik zemin üzerine oturan kirişler*, 1993, Doctoral dissertation.

[6] Karamahmutoğlu, M. A. (2000). *Elastik Zemine Oturan Kirişlerin ve Palplanş Perdelerin Sonlu Farklar Metodu ile Analizi* (Doctoral dissertation, Fen Bilimleri Enstitüsü).

[7] Hetényi, M., and Hetbenyi, M. I. *Beams on elastic foundation: theory with applications in the fields of civil and mechanical engineering.* 1946, (Vol. 16). Ann Arbor, MI: University of Michigan press.

[8] Chopra, A. K. *Dynamics of Structures: Theory and Applications to Earthquake Engineering*. 2001, Prentice-Hall Internal Series in Civil Engineering and Engineering Mechanics.

[9] Clough, R. W., and Penzien, J.. *Dynamics of Structures*, 2003, Computers & Structures, Inc.

[10] Decanini, L.D., Liberatore L., and Mollaioli F. *Characterization of Displacement Demand for Elastic and Inelastic SDOF Systems*. Soil Dynamics and Earthquake Engineering, 2003, pp. 455-471.

[11] Humar, J.L. *Dynamics of Structures*, 2002, Taylor & Francis.

[12] Kramer, S. L. *Geotechnical Earthquake Engineering*, 1996, Prentice-Hall Internal Series in Civil Engineering and Engineering Mechanics.

RESEARCH OF RECIPROCATING SPEED OF THE RODS SUSPENSION POINT IN THE LOW-SPEED OPERATION MODE OF THE MECHANICAL TRANSMISSION OF THE NEW CONSTRUCTIVE SOLUTION OF THE SUCKER-ROD PUMP

Beyali AHMEDOV[1], Isa KHALILOV[2], Anar HAJIYEV[3]

[1,2,3]Department of "Mechatronic and machine design", Azerbaijan Technical University, Baku, Azerbaijan

E-mail: ahmedov.beyali@mail.ru[1] , khalilov@aztu.edu.az[2] , anar_hajiyev_1991@mail.ru[3]

Abstract. The article investigates the problem of determining the number of swings of the rods suspension point of the new constructive solution of the sucker-rod pumping unit in the low-speed operation mode. It was determined that this small value of the speed causes a decrease in the maximum kinetic energy caused by the mechanical transmission of the rod well pump, and therefore, considering this energy parameter of the system as an analyzed parameter is of great practical importance. Therefore, in the article, as a criterion for the low-speed operation mode, a comparison of the maximum kinetic energy of the pumping unit and the useful energy spent on lifting of the liquid from the well was proposed. It was determined that with the increase in the diameter of the plunger, the useful energy used on lifting the liquid from the well increases, and accordingly, the share of kinetic energies in the total used energy balance increases accordingly.

Key words: *pumping unit, plunger, kinetic energy, reciprocating speed, operation mode.*

Introduction. At all stages of the economic development of many countries, the oil industry is the most important and attention-grabbing sector. It is impossible to develop the general development plan of the state and predict its future development stages without taking into account the situation and opportunities of this field. One of the most important places in the economic development of our republic is the extraction and transportation of the oil to the global world market. From this point of view, there is a great need to research and create new constructions of sucker-rod pumping units used in oil extraction [1, 2, 3].

Taking into account the mass of sucker-rod pumping unit in use, one of the urgent issues is either their improvement or the creation of new constructive solutions with a more perfect construction [6, 7, 8, 9, 10, 11].

Therefore, in order to ensure the stable operation of the mechanical drive of the sucker-rod pump and save energy, as well as to reduce the overall dimensions and increase the reliability at the Department of "Mechatronic and machine design" of Azerbaijan Technical University were developed the new constructive solution of beamless sucker-rod pumping unit [15], the originality of the construction is approved by Eurasian Patent Organization №039650 [4], 2022 and the Intellectual Property Agency of the Republic of Azerbaijan № a2019 0162, 2021 [5].

At Figure 1 shown the overview of the new constructive solution of the sucker-rod pumping unit. The new constructive solution of the sucker-rod pumping unit consist from frame (1), three-phase short-circuited asynchronous motor (2), V-belt drive (3), rigidly connected two-flow three-stage re-ducer (4), on the drive shaft of which on one side mounted double-shaped brake (5) and on the other side V-belt pulley (6), and on the driven shaft of its installed two cranks (7); guide blocks (8, 9), ropes (10) connected to the rods suspension point. The converting mechanism, which consists of two slider-crank linkage (12), converts the rotational motion of the crank into the

upstroke and down-stroke movement of the rod suspension point. The mechanical transmission has counterweights whose weight can be adjusted (14), located on a movable cross beam (13), which is connected with hinge joint to the connecting-rod.

The guide blocks are surrounded by a flexible rope, one end of which is connected to the mova-ble beam, and the other end is connected to the rods suspension point. In addition, the mechanical drive has a guide system consisting of two vertically located cylindrical tubes (15) and the movable beam. The mechanical transmission has articulated front (18) and rear (19) arms, which can be ad-justed by using (16,17) screw tensioners, a fixed cross beam (20) rigidly connected to the guide tubes. The screw tensioner (21) is connected to the frame of the construction, as well as to the joints with the front and rear arms [14, 16].

The working principle of mechanical transmission is as follows: After the three-phase asynchronous motor is started, the step pulley of the V-belt drive rotates and drives the driven pulley mounted on the drive shaft of the multi-step reducer. The required rotational motion is supplied to the driven shaft of the multi-stage reducer. At the same time, the cranks mounted on the driven shaft of the reducer also rotate; a movable cross beam and an adjustable counterweights located on it moves up and down. Guide blocks installed on the immovable transverse beam and front arm of the device surrounded by a flexible rope on both sides, in turn, participate in moving the rods suspension point, in other words, the piston of the well up and down. In this case, the stroke of the rods suspension point, its speed and acceleration are closer to the ideal law.

The laboratory model of the mechanical transmission which consist from transforming mechanism, ropes, cranks and a reducer, has been developed and tested.

a)   *b)*   *c)*
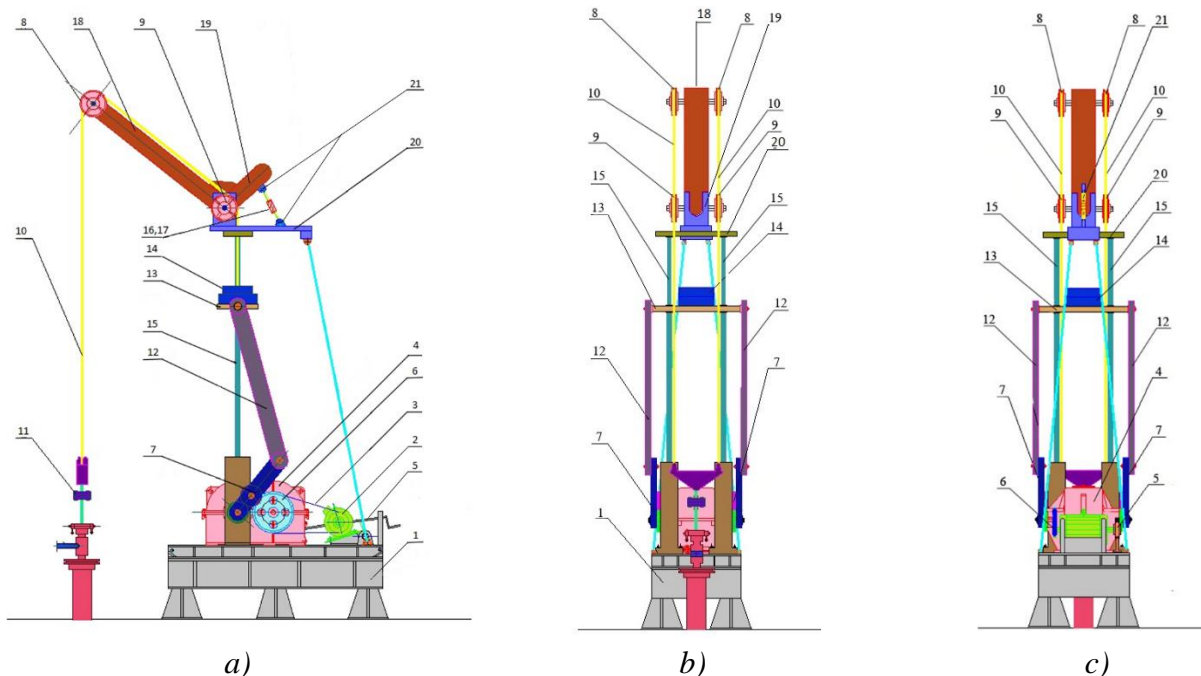
Fig. 1. New constructive solution of beamless pumping unit consisting of an
slider-crank mechanism and a rope-block system:
a - side view; b - front view; c - rear view

Formulation of the problem. During the operating sucker rod pump, the pumping unit is affected by the gravity force of the rods column, the gravity force of the liquid column, the resistance force caused by the friction of the rods column against the well walls (edge friction), the resistance force to the movement of the rod column due to friction inside the viscous fluid, the

friction force in the reducer and forces that create torque in the engine of the mechanical transmission. As a result of studies, it has been determined that the role of other forces (frictional forces in the joints, etc.) affecting the pumping unit is insignificant and their influence can be ignored.

The boundary friction force caused by the friction of the rods column against the walls of the pump-compressor pipes is determined depending on the diameters of the pipes and rods, well path and the lubrication properties of the fluid. At low speeds, the viscous (hydrodynamic) friction force is determined depending on the relative speed of the rod column and the liquid, as well as the viscosity of the liquid in the riser pipes.

At present, asynchronous motors with a short-circuited rotor with a high starting torque are used in the transmission of the pumping unit. It is known that these motors have rigid mechanical characteristics, that is, the angular speed of the electric motor rotor during operation is very little dependent on the load. Such engines have a significant power reserve to overcome possible overloads when starting the mechanical transmission of the sucker-rod pump, the balancing of its rotor practically doesn't depend on the number of swings per minute of the transmission. Therefore, it is considered that the speed of the rods column and the resistance forces generated during its movement do not depend on balancing. That is, the work of frictional forces is constant and not related to balansing.

Forces of gravity are potential forces, so the work done by gravity forces in one cycle of the pumping unit is always zero. Therefore, these forces don't depend on equilibrium [12, 13].

Research method. During the operation of the mechanical transmission of the sucker-rod pump, its rods column, plunger pump, pulleys, cross beams, connection rod, cranks, balancing counterweights, gears of the reducer, belts and the rotor of the electric motor are in motion. Therefore, the kinetic energy of the mechanical transmission of the sucker-rod pump consists of the sum of the kinetic energies of these elements [6, 7, 9, 10]:

$$E_{ms} = E_{rd} + E_{pul} + E_{beam} + E_{cr} + E_{crank} + E_{cw} + E_{gd} + E_{belt} + E_{rot}$$

It is known that sucker-rod pumping units work at low speeds. That is, the number of swings per minute of the rod suspension point doesn't exceed 10….15 min^{-1}. Therefore, this small value of the speed causes a decrease in the maximum kinetic energy caused by the mechanical transmission of the sucker-rod pump, and therefore it has great practical importance to consider this energy parameter of the system as an analyzed parameter.

Therefore, the article suggests comparing the maximum kinetic energy of the pumping unit and the useful energy spent on lifting the liquid from the well as a criterion of the low-speed operation mode.

In order to simplify the calculations and make the results obtained more convenient for engineering calculations, we assume that the mass of the rods column and counterweights are significantly greater than the mass of other parts of the pumping unit. Therefore, we can determine the kinetic energy of the system for the proposed new constructive solution of the beamless sucker-rod pumping unit as follows:

$$E_{ms} = E_{rd} + E_{cw}$$

there E_{rd}, E_{cw} - are the kinetic energies of the rods column, the cross beam, and the counterweights, respectively.

Beyali AHMEDOV, Isa KHALILOV, Anar HAJIYEV
Research of reciprocating speed of the rods suspension point in the low-speed operation mode of the
mechanical transmission of the new constructive solution of the sucker-rod pump

Kinetic energy of a rods column of the new constructive solution of the sucker-rod pumping unit:

$$E_{rd} = \frac{\rho_{rd} \cdot A_{rd} \cdot L \cdot v^2}{2} = \frac{\rho_{rd} \cdot \frac{\pi \cdot d_{rd}^2}{4} \cdot L \cdot (\omega \cdot r)^2}{2} = \frac{\rho_{rd} \cdot \frac{\pi \cdot d_{rd}^2}{4} \cdot L \cdot (2 \cdot \pi \cdot n)^2 \left(\frac{S_{rd}}{2}\right)^2}{2} =$$

$$= \frac{\rho_{rd} \cdot d_{rd}^2 \cdot L \cdot \pi^3 n^2 \cdot S_{rd}^2}{8}$$

there ρ_{rd} - rods material density; A_{rd} - cross-sectional area of the rod; L - well depth; v -speed of the rods suspension point; n -number of the swings of the rods suspension point; S -stroke of the rods suspension point.

For the movable counterweight balancing method, we use the condition of equality of the performed work during the upstroke and downstroke movement of the rods suspension point to determine the kinetic energy generated by the action of counter loads. Thus, for movable counterweight balancing method, the work spent by the engine during the upstroke and downstroke movement of the rods suspension point is:

$$A_{up} = (G_{rd} + G_{lq})S_{rd} - G_{cw}S_{cw} \tag{1}$$

$$A_{dw} = -G_{rd}S_{rd} + G_{cw}S_{cw} \tag{2}$$

If we take the work done during the upstroke and downstroke movement equally to each other

$$(G_{rd} + G_{lq})S_{rd} - G_{cw}S_{cw} = -G_{rd}S_{rd} + G_{cw}S_{cw}$$

If $S_{rd} = S_{cw} = 2r$ and $S_r = 2R$, then

$$r\left(G_{rd} + \frac{G_{lq}}{2}\right) - G_{cw}r = 0$$

If we finde weight of the movable counterweights from the last expression:

$$G_{cw} = \left(G_{rd} + \frac{G_{lq}}{2}\right) \tag{3}$$

Then the kinetic energy generated by the action of movable counterweights:

$$E_{cw} = \frac{\left(\left(G_{rd} + \frac{G_{lq}}{2}\right)\right)v^2}{2} = \frac{\left(\rho_{rd} \cdot \frac{\pi \cdot d_{rd}^2}{4} \cdot L + \rho_{lq}\frac{\pi \cdot D_{pl}^2}{8}H_d\right)v^2}{2} =$$

$$= \frac{\left(2\rho_{rd} \cdot d_{rd}^2 \cdot L + \rho_{lq}D_{pl}^2H_d\right)\pi^3 n^2 S_{rd}^2}{16} \tag{4}$$

Therefore, we can define the kinetic energy of the system for the proposed new constructive solution of the beamless sucker-rod pumping unit as follows:

$$E_{ms} = \frac{\rho_{rd} \cdot d_{rd}^2 \cdot L \cdot \pi^3 n^2 \cdot S_{rd}^2}{8} + \frac{\left(2\rho_{rd} \cdot d_{rd}^2 \cdot L + \rho_{lq}D_{pl}^2H_d\right)\pi^3 n^2 S_{rd}^2}{16} = \tag{5}$$

Beyali AHMEDOV, Isa KHALILOV, Anar HAJIYEV

Research of reciprocating speed of the rods suspension point in the low-speed operation mode of the mechanical transmission of the new constructive solution of the sucker-rod pump

$$= \frac{\left(4\rho_{rd} \cdot d_{rd}^2 \cdot L + \rho_{lq}D_{pl}^2 H_d\right)\pi^3 \cdot n^2 \cdot S_{rd}^2}{16}$$

And the useful energy used to lifting of liquid:

$$E_{us} = \left(G_{lq} - G_{as}\right)S_{rd} = \frac{\pi}{4} \cdot D_{pl}^2 \cdot S_{rd}\left(\rho_{lq} \cdot L - \rho_{as} \cdot H_d\right)g \tag{6}$$

there ρ_{rd} - density of lifting liquid; ρ_{as} - density of lifting liquid at annular space; D_{pl} -diametr of the plunger; H_d - dynamic level height.

If we assume that the kinetic energy of the system is significantly less than the useful energy, then to determine the minimum number of swings of the rods suspension point of the sucker-rod pumping unit, we take the following expression

$$n = \sqrt{\frac{4 \cdot D_{pl}^2 \cdot \left(\rho_{lq} \cdot L - \rho_{as} \cdot H_d\right) \cdot g}{\left(4\rho_{rd} \cdot d_{rd}^2 \cdot L + \rho_{lq}D_{pl}^2 H_d\right) \cdot \pi^2 \cdot S_{rd}}} \tag{7}$$

For example, if the density of the liquid is 900 kg/m³, the density of the rod material is 7800 kg/m³, well depth is 1000 m, the diameter of the plunger is 70 mm, the diameter of the rod column is 19 mm, density of lifting liquid at annular space is 800 kg/m³, the dynamic level is 200 m, if the stroke of the rods suspension point is 3,0 m, then the maximum number of oscillations per minute, which ensures the low speed operation mode of the pumping unit, will be 4,87. For comparison, the number of oscillations per minute in the static mode according to the Cauchy criterion corresponds to 16,7, which is significantly greater than its minimum value [14, 16, 17].
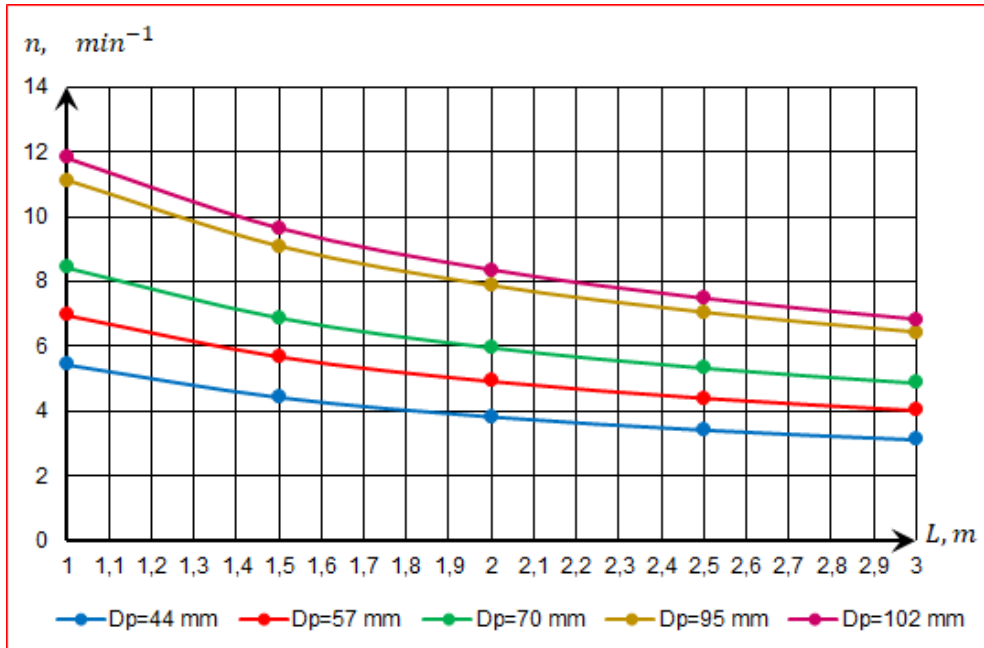
Fig. 2. Graph of the dependence of the reciprocating speed characterizing the low-speed operation mode of the sucker-rod pumping unit on the stroke of the rods suspension point

Figure 2 shows the graph of the dependence of the reciprocating speed characterizing the low-speed operation mode of the sucker-rod pumping unit on the stroke of the rods suspension point. As

can be seen from the graph, with the increase in the diameter of the plunger, the useful energy used to lift the liquid from the well increases, and accordingly, the share of kinetic energies in the total balance of the energy used increases accordingly.

Results and conclusions. In the article, analytical expressions were proposed to determine the minimum reciprocating speed of the rods suspension point in the low-speed operation mode of the mechanical transmission of the new constructive solution of the sucker-rod pump. It was determined that the low-speed of the rods suspension point causes the decrease in the maximum kinetic energy caused by the mechanical transmission of the sucker-rod pump, and therefore it is of great practical importance to consider this energy parameter of the system as an analyzed parameter. Therefore, in the article, as a criterion for the low-speed operation mode, a comparison of the maximum kinetic energy of the pumping unit and the useful energy spent on lifting of the liquid from the well was proposed. It was determined that with the increase in the diameter of the plunger, the useful energy used on lifting the liquid from the well increases, and accordingly, the share of kinetic energies in the total used energy balance increases accordingly.

REFERENCES

[1]. Takacs, G. *Sucker-Rod Pumping Handbook*. Elsevier Science, 2015, p. 598.

[2]. Elias, S.K., Rutácio O.C. *Sucker Rod Pumping: Design, Operation and Maintenance*. Independently published, 2020, p. 430.

[3]. Zakharov, B. S. *Special types of sucker-rod pumps.* Chemical and Petroleum Engineering. 2008, V44, 3, pp. 217-223.

[4]. Abdullaev, A.I., Nadjafov, A.I., Ahmedov, B.B., Chalabi, I.G., Abdullaev, A.A., Hajiyev, A.B. *Mechanical drive of sucker-rod pumps. Eurasian invention patent № 039650. EAPO 2022.02.21.* https://www.eapo.org/ru/patents/reestr/patent.php?id=39650

[5]. Abdullaev, A.I., Nadjafov, A.I., Ahmedov, B.B., Chalabi, I.G., Abdullaev, A.A., Hajiyev, A.B. *Mechanical drive of sucker-rod pumps. Patent of Intellectual Property Agency of the Republic of Azerbaijan*, № İ 2021 0113, a2019 0162, 2021.

[6]. Ahmedov, B.B., Hajiyev, A.B., Mustafayev, V.S. *Estimation of the equality of the beamless sucker-rod oil pumping unit by the value of the consumption current*. Nafta-Gaz journal. 2021, 9, pp. 571-578.

[7]. Ahmedov, B.B., Hajiyev A.B. *Assessment of dynamic forces in new construction design for beamless sucker-rod pumping units*. Nafta-Gaz journal. 2020, 5, pp. 299-310.

[8]. Ahmadov, B.B., Hajiyev, A.B. (2019) *Evaluation of elastic deformations in the elements of newly developed design solution for sucker-rod pumping unit*. Azerbaijan Oil Industry Journal. 2019, 2, pp. 33-37.

[9]. Ahmedov, B. *Assessment of dynamic efforts taking into account of inertial and vibrating loads in deaxial pumping units*. Journal of Petroleum Exploration and Production Technology. 2020, 10(4), pp. 1401-1409.

[10]. Ahmedov, B., Najafov, A., Abdullaev, A. *Balancing of cyclically changing load with newly designed mechanical drive for sucker-rod pumps*. Oil GAS European Magazine, 4/2019, pp. 112-115.

[11]. Najafov, A.M. *The exploratiry designing of mechanical drive of sucker-rod pumps*. Palmarium Academic Publishing (Germany), 2019, p. 156.

[12]. Ahmedov, B.B., Najafov, A.M, Abdullayev, A.H, Chalabi, I.G, Veliev, F. *Calculation of toothed gear mechanisms in machines and assemblies considering the effect of lubricants*. Eastern European Journal Enterprise Technologies. 2018, 5/7 (95), pp. 43-54.

Beyali AHMEDOV, Isa KHALILOV, Anar HAJIYEV

Research of reciprocating speed of the rods suspension point in the low-speed operation mode of the mechanical transmission of the new constructive solution of the sucker-rod pump

[13]. Ahmedov, B.B, Najafov, A.M, Abdullayev, A.I. *Determination of the kinematic parameters of the new constructive solution of the beamless sucker-rod pump.* Journal of Structural Enginering & Applied Mechanics. 2018, 1(3), pp. 128-135.

[14]. Khalilov, I.A., Kerimov, S.Kh., Rzaeva, G.M. *Method of lever mechanism synthesis, assuring specified motion law.* Vestnik Mashinostroeniya. 2017, 3, pp. 3-5.

[15]. Hajiyev, A. (17-19 June, 2020). *About new constructive solution of sucker-rod oil pumping unit.* Topical issues of rational use of natural resources: Scientific conference abstracts. (St. Petersburg Mining University), 2020, pp. 29-30.

[16]. Romero, O. J., Almeida P. *Numerical simulation of the sucker-rod pumping system.* Ingeniería e Investigación. 2014, 34 (3), 4-11.

[17]. Fakher, S., Khlaifat, A., Hossain, M., Nameer, H. *A comprehensive review of sucker rod pumps' components, diagnostics, mathematical models, and common failures and mitigations.* Journal of Petroleum Exploration and Production Technology. 2021, 11(10), pp. 3815-3839.

ON THE MATRIX GENERALIZATION OF THE THEORY OF MACHINING ACCURACY

Nizami YUSUBOV[1*], Heyran ABBASOVA[2], Ramil DADASHOV[3], Ibrahim SALMANOV[4]

[1*,2,3]Department of Machine Building Technology, Azerbaijan Technical University, Baku, Azerbaijan
[4] Shipbuilding and Ship Repair Engineering, Azerbaijan State Marine Academy, Baku, Azerbaijan

E-mail: nizami.yusubov@aztu.edu.az[1],[*] abbasova.heyran@aztu.edu.az[2]
dadashov@aztu.edu.az[3], ibraqim.salmanov@gmail.com[4]

Abstract: The article provides a matrix generalization of distortion models and scattering fields of dimensions performed during turning with a spatial arrangement of the tool, taking into account the simultaneous action of all components of the cutting forces of the setting tool and elastic deformations of the technological system in all coordinate directions. A full-factor model of dimension distortion for single-carriage adjustment has been developed, which allows taking into account not only plane-parallel movements of technological subsystems, but also their angular movements around base points. Thus, the Eq. developed for the total displacement vectors $\overline{u_i}$ is proposed to be taken as the basis for a full-factor model of the machining error. The presented analytical models describe only plane-parallel displacements of contacting bodies. It is shown that in order to take into account the whole complex of displacements in them, i.e. and angular displacements, it is sufficient to replace the plane-parallel displacement vectors of each contacting body $\overline{r_i}$.

Keywords: matrix generalization of the theory of accuracy, turning, distortion models, models of scattering fields, performed dimensions, coordinate displacements of the technological system, compliance matrix of technological system, machining error

Introduction. Machining accuracy is predetermined by a whole complex of random and regular factors, their mutual influence and interaction: dimensional wear of the cutting tool (Δ_w), temperature deformations ($\Sigma\Delta_t$) and geometric inaccuracies of the technological system links ($\Sigma\Delta_m$), errors in the installation of workpieces on the machine ($\Delta\varepsilon_i$) and its settings for the size being performed (Δ_s), spread of allowances and physical and mechanical properties of workpieces, etc. [1, 2]. The machining accuracy has its numerical expression through the machining error, which characterizes the degree of discrepancy between the real part and the ideal scheme underlying the machining method. All elementary error components can be divided into two groups:

- independent or weakly dependent on cutting conditions: Δ_s, Δ_w, $\Delta\varepsilon_i$, $\Sigma\Delta_m$, $\Sigma\Delta_t$;
- determined by cutting conditions: Δy.

The first group of errors is not of interest in the development of a simulation model intended for designing a technological process. These components in the simulation model participate as constants, the values of which are taken from the extensive reference literature [2].

A special place in modeling the accuracy of machining is occupied by the elementary error Δy, which occurs due to the elastic displacements of the technological system under the action of cutting forces. Its value is directly determined by the cutting conditions and the characteristics of the technological system. Therefore, it is the main control object, which requires a strict mathematical description.

The foundations of accuracy modeling were laid by A.P. Sokolovsky and K.V. Votinov [3]. Further study of these issues was carried out by B.S. Balakshin, V.S. Korsakov, B.M. Bazrov [4].

Since the machining error is characterized by a number of different indicators, two groups of machining error models can be distinguished:

- dimension distortion model;
- model of scattering field of dimension.

For the simplest case of turning, the scheme for the formation of dimension distortion was formed by V.S. Korsakov (Fig. 1.).
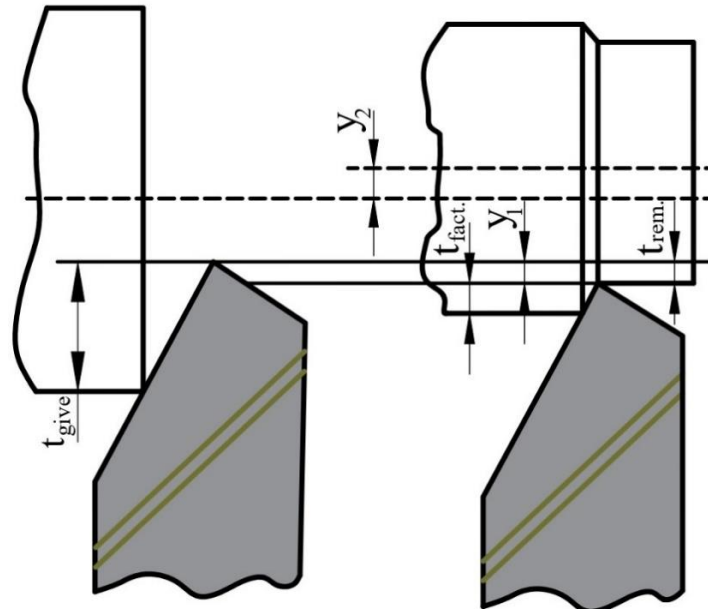
Fig.1. Scheme of elastic displacements of the technological system during turning [3]

Under the action of cutting forces, the links of the technological system are displaced from the initial (unloaded) state, which ultimately causes a violation of the relative position of cutting edge of the tool and the workpiece surface established by the adjustment. Since the technological system in the range of loads inherent in the cutting process is a linear elastically deformable system, he proposed a formula for the value of the mutual displacement of the tool and workpiece: $y = y_1 + y_2$, which makes it possible to calculate the dimension distortion in the diametrical direction depending on the machining conditions.

When machining a batch of workpieces, the cutting force changes as a result of uneven depth of cut (due to the variability of the size of the workpieces in the batch) and the instability of the mechanical properties of the material of the workpieces. The instability of the cutting force leads to the inconstancy of the amount of elastic compression, and, consequently, the size of the part in the batch. B.S. Balakshin formulated the principle of taking into account fluctuations in the allowance when calculating the machining error [3].

V.S. Korsakov proposed analytical dependencies to determine the error of the performed dimension of single-tool turning. He proposed to determine the scattering field of the dimension being performed in a given section as the difference between the largest and smallest values of the residual (not removed due to elastic displacements) depth of cut. However, he takes into account only fluctuations in the allowance and hardness of the material being machined, and these are not all the factors that determine the scattering of elastic deformations.

K.V. Votinov introduced into the scattering field model, along with the traditional component, determined by the allowance fluctuations, a new one, determined by the depth of cut. However, the coefficients in this formula are determined experimentally, and therefore the entire dependence is empirical.

Formulation of the problem. The component of the machining error that occurs due to the elastic displacement of the elements of the technological system under the influence of cutting forces, which is often called the deformation component, is the most controllable during the machining process and at the design stage. By varying the cutting conditions, the geometry of the cutting tool,

24

the cutting material, the initial error, one can significantly influence the magnitude of the machining error. Therefore, the mathematical model of the deformation component of the machining error is *the basis of the computational theory of machining accuracy*.

It is generally accepted that the model of the deformation component of the machining error can be built using the theory of linear deformable systems [5]. However, when describing the properties of a deformable system, in our case it is a technological system, the question arises about the degree of detail of the description. The L.P. Medvedev model takes into account one characteristic of the system - its total rigidity, while the B.M. Bazrov model takes into account the rigidity of all elements of the system [3, 5]. The second approach is absolutely correct methodically and leads to a strict logical statement of the problem, however, in this case the model becomes very cumbersome and cannot be analyzed analytically. In addition, the practical determination of the rigidity of each element is associated with significant difficulties.

Therefore, it is proposed, in accordance with the methodology of B.M. Bazrov, to decompose the technological system into its component parts, but limit it to the level of subsystems, and the number of subsystems should be minimal [5]. Taking into account the specifics of automatic lathe machining (sufficient rigidity of the part, its predominant cantilever fastening), it is proposed to distinguish the following subsystems:

- spindle - chuck (collet) - part;
- carriage – holder – tool.

For each of these subsystems, it can be considered that, under the influence of cutting forces, it experiences elastic displacement as a single element. The rigidity of such a subsystem can be easily determined experimentally using a modified production method [5]. The production method makes it possible to evaluate the rigidity during machining and therefore simultaneously takes into account the dynamics of the deformation process.

The true dynamic characteristics of the rigidity of the machine tool and other elements of the technological system (amplitude-frequency and amplitude-frequency-phase characteristics) more accurately describe the resistance of deformable elements during the application and removal of the load [6]. However, their values for automatic turning equipment are not available in the reference literature, and the methods of experimental evaluation have been worked out only for the simplest cases.

Distortion of performed dimension. In accordance with the formulation of the problem, we decompose into two subsystems:

- subsystem 0: "spindle-chuck-part" (rigidity along the coordinate axes Y and X respectively j_{y0} and j_{x0});
- subsystem 1: "carriage-holder-tool" (rigidity along the coordinate axes Y and X respectively j_{y1} and j_{x1}).

Then the calculation scheme of V.S. Korsakov (Fig. 1) is converted to the form shown in Fig. 2.

Under the action of force P_{y0} subsystem 0 has displacement y_0, and subsystem 1 under the action of reaction P_{y1} has displacement y_1. Considering each subsystem as elastically deformable, we obtain:

- for displacements of subsystem 0 along the Y and X axes, respectively:

$$y_0 = \frac{P_y}{j_{yo}}, \qquad x_0 = \frac{P_x}{j_{xo}}$$

- for displacements of subsystem 1 along the Y and X axes:

$$y_1 = -\frac{P_y}{j_{y1}}, \qquad x_1 = -\frac{P_x}{j_{x1}}$$
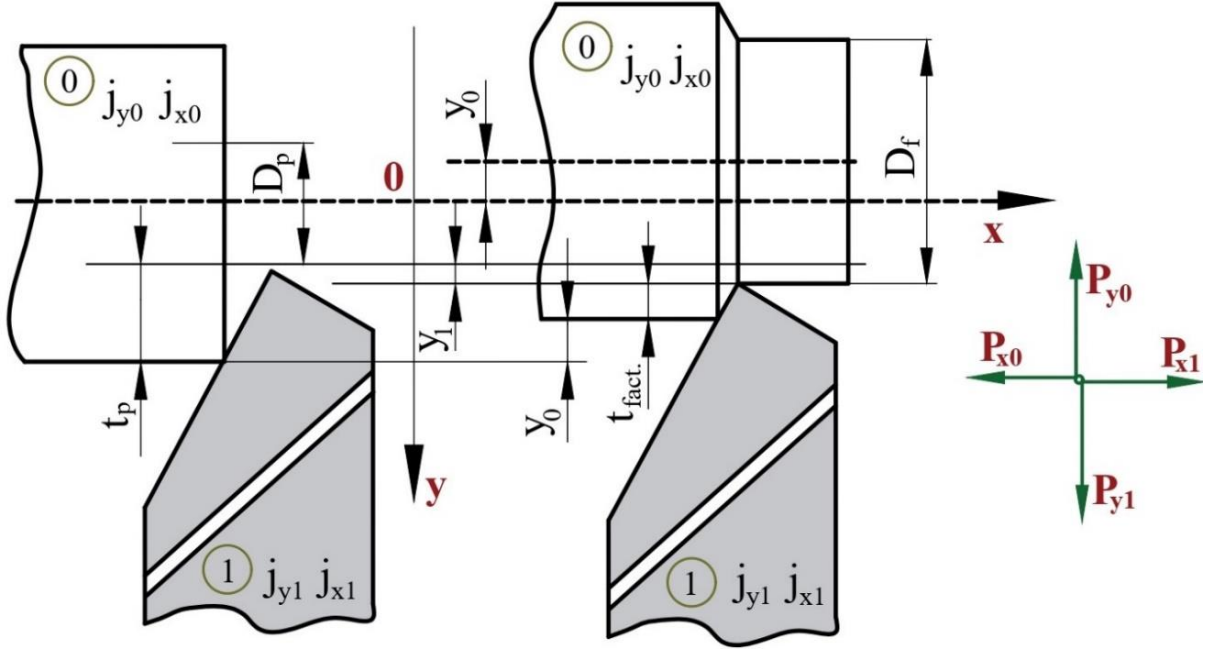
Fig. 2. Design scheme for elastic displacements of subsystems of technological system in turning

Performing the vector summation of these displacements in accordance with the design scheme, we obtain the distortions of the performed dimensions along each axis with respect to the static setting:

$$y = y_0 - y_1 = P_y \left(\frac{1}{j_{y0}} + \frac{1}{j_{y1}} \right) = \frac{P_y}{j_{y01}}; \qquad x = x_0 - x_1 = P_x \left(\frac{1}{j_{x0}} + \frac{1}{j_{x1}} \right) = \frac{P_x}{j_{x01}} \qquad (1)$$

where j_{y01} and j_{x01} are the total rigidity of the technological system along the coordinate axes Y and X, respectively:

$$\frac{1}{j_{y01}} = \frac{1}{j_{y0}} + \frac{1}{j_{y1}}; \qquad \frac{1}{j_{x01}} = \frac{1}{j_{x0}} + \frac{1}{j_{x1}} \qquad (2)$$

Using the cutting forces $P_y = C_{p_y} t^{x_{p_y}} S^{y_{p_y}}$, $P_x = C_{p_x} t^{x_{p_x}} S^{y_{p_x}}$ model and denoting the actual depth of cut t_f to distort dimensions, we get:

$$y = \frac{C_{p_y} t_{tm}^{x_{p_y}} S^{y_{p_y}}}{j_{y01}}; \qquad x = \frac{C_{p_x} t_{tm}^{x_{p_y}} S^{y_{p_x}}}{j_{x01}} \qquad (3)$$

As follows from the design scheme (Fig. 2), the actual depth of cut t_f is expressed through the calculated t:

$$t_f = t - y_0 - y_1 = t - y \qquad (4)$$

Then from (3) we arrive at the system of transcendental Eqs.:

$$\begin{cases} y = \dfrac{C_{p_y}(t-y)^{x_{p_y}} S^{y_{p_y}}}{j_{y01}} \\ x = \dfrac{C_{p_x}(t-y)^{x_{p_x}} S^{y_{p_x}}}{j_{x01}} \end{cases} \qquad (5)$$

26

Since the condition y<< t is valid for the case of cutting edge machining, it is possible to get rid of transcendence in expressions (5) by linearization:

$$(t - y)^{x_{py}} = t^{x_{py}} \left(1 - \frac{y}{t}\right)^{x_{py}} \approx t^{x_{py}} \left(1 - \frac{y}{t} x_{py}\right)$$

Solving the resulting linear Eq. with respect to y, we obtain:

$$y = \frac{1}{1 + \frac{C_{py} t^{x_{py}-1} S^{p_y}}{j_{y01}} \cdot x_{py}} \cdot \frac{C_{py} t^{x_{py}} S^{p_y}}{j_{y01}} \tag{6}$$

Since, under real conditions of turning, the elastic displacements of the technological system are much less than the allowance to be removed (calculated depth of cut), the influence of the correction in the denominator can be neglected (see Table 1).

Table 1. Influence of the correction in the denominator in formula (6) [5].

№	Machining conditions	$\frac{C_{py} t^{x_{py}-1} S^{y_{py}}}{j_{y01}} \cdot x_{py}$
1	External turning of structural steel with a carbide cutter on a 1K62 machine, t = 2 mm, S = 0.15 mm/rev	0,065
2	Rough turning, t = 4 mm, S = 0.6 mm/rev	0,11
3	Turning with a high speed tool, t = 2 mm	0,025

Thus, for cutting edge machining, we can take the dependence:

$$y \approx \frac{C_{py} t^{x_{py}} S^{y_{py}}}{j_{y01}} \quad ; \qquad x \approx \frac{C_{px} t^{x_{px}} S^{y_{px}}}{j_{x01}} \tag{7}$$

The resulting expressions are close to the L.P. Medvedev model [5]. However, the total rigidity of the technological system along the coordinate axes Y and X works here, which have a clear physical meaning and, taking into account expressions (2), allow a rigorous experimental determination, for example, using a modified production method [5].

Scattering field of performed dimension. Expressions (7) make it possible to calculate the distortions of the performed dimensions, that is, to estimate the error of the static adjustment. These expressions can be used to calculate the adjustment size. However, a more relevant characteristic of the accuracy of the performed dimension is the magnitude of the scattering field.

The works of B.S. Balakshin and V.S. Korsakov laid the foundations for the calculation of the scattering field, they also identified the main factors that predetermine the occurrence of scattering fields (fluctuations in the allowance and strength properties of the material being machined in a batch of parts).

In production, the machining of a batch of parts is carried out not on one machine, but on a certain group of machines (one model), which also have a spread in their characteristics. Therefore, the stiffness value in model (7) also has a spread. According to GOST 43-85, 18097-88, 6820-75 lathes of normal accuracy have an allowable variation in rigidity of about 20% [7]. The spread of the strength properties of workpieces is also regulated: for rolled products, the tolerance for ultimate strength σ_b is *20%* [2, 5].

Therefore, the main technological factors causing the appearance of scattering fields can be called [1, 3, 5]:

- machining allowance fluctuations $\quad t \in \left[t - \frac{\Delta t}{2}; \ t + \frac{\Delta t}{2}\right]$ (8)

- variability in mechanical properties (e.g. hardness) of workpieces within a batch

$$C_{tm} \in C, \left[1 - \frac{v}{2}; \ 1 + \frac{v}{2}\right] \tag{9}$$

- variation in rigidity of different machines of the same model

$$j_{tm} \in j, \left[1 - \frac{\Delta j}{2}; \ 1 + \frac{\Delta j}{2}\right] \tag{10}$$

Such a mathematical representation of possible fluctuations in the properties of the technological system indicates the way for calculating the magnitude of the scattering field.

To determine the scattering field of the dimension being performed (its dynamic component), it is necessary to find the limiting values of the dimension distortion.

$$y_{max} = \frac{C_{p_y}\left(1+\frac{v}{2}\right)\left(t+\frac{\Delta t}{2}\right)^{x_{p_y}} S^{y_{p_y}}}{j_{y01}\left(1-\frac{\Delta j}{2}\right)} \tag{11}$$

$$y_{min} = \frac{C_{p_y}\left(1-\frac{v}{2}\right)\left(t-\frac{\Delta t}{2}\right)^{x_{p_y}} S^{y_{p_y}}}{j_{y01}\left(1+\frac{\Delta j}{2}\right)} \tag{12}$$

As a result, for the scattering field we obtain:

$$\Delta y = \frac{C_{p_y} t^{x_{p_y}} S^{y_{p_y}}}{j_{y01}} \cdot \left[\frac{\left(1+\frac{v}{2}\right)\left(1+\frac{\Delta t}{2t}\right)^{x_{p_y}}}{\left(1-\frac{\Delta j}{2}\right)} - \frac{\left(1-\frac{v}{2}\right)\left(1-\frac{\Delta t}{2t}\right)^{x_{p_y}}}{\left(1+\frac{\Delta j}{2}\right)}\right] \tag{13}$$

For the obtained dependence (13), linearization is admissible, since $0.5v \ll 1, \ 0.5\Delta j \ll 1$ and for cutting edge machining, $\Delta t/2t < 1$ is true. Therefore, one can write:

$$\left(1 - \frac{\Delta t}{2t}\right)^{x_{p_y}} \approx 1 - \frac{x_{p_y}\Delta t}{2t}; \qquad \frac{1}{1-\frac{\Delta j}{2}} \approx 1 + \frac{\Delta j}{2}; \qquad \frac{1}{1+\frac{\Delta j}{2}} \approx 1 - \frac{\Delta j}{2}$$

After substitution into (13) we obtain:

$$\Delta y = \frac{C_{p_y} t^{x_{p_y}} S^{y_{p_y}}}{j_{y01}} \left[\left(1 + \frac{v}{2}\right)\left(1 + \frac{\Delta j}{2}\right)\left(1 + x_{p_y}\frac{\Delta t}{2t}\right) - \left(1 - \frac{v}{2}\right)\left(1 - \frac{\Delta j}{2}\right)\left(1 - x_{p_y}\frac{\Delta t}{2t}\right)\right]$$

Considering that ν, Δj and Δt are small values, after discarding the values of the second order of smallness and introducing the designation Δj+ν=ω for the total spread of the properties of the technological system, we have for the diametrical dimension:

$$\Delta y \approx \frac{C_{p_y} t^{x_{p_y}-1} S^{y_{p_y}}}{j_{y01}} \left[\omega t + x_{p_y}\Delta t\right] \tag{14}$$

Similarly for the linear dimension:

$$\Delta x \approx \frac{C_{p_x} t^{x_{p_x}-1} S^{y_{p_x}}}{j_{x01}} \left[\omega t + x_{p_x}\Delta t\right] \tag{15}$$

As you can see, the value of the scattering field depends not only on the fluctuations of the allowance, but has a term with the value of the allowance to be removed. Thus, these formulas are an analytical representation of the K.V.Votinov model, which predicted the existence of such a relationship.

For common cutting conditions, the dependence of cutting forces on depth is very close to linear: the exponents x_{p_y} and x_{p_x} for longitudinal turning with a carbide cutter are of the order of 0.9.

Therefore, it is permissible to use models linearized in t:

$$\Delta y \approx \frac{c_{p_y} s^{y_{p_y}}}{j_{y01}} [\omega t + \Delta t] \tag{16}$$

$$\Delta x \approx \frac{c_{p_x} s^{y_{p_x}}}{j_{x01}} [\omega t + \Delta t] \tag{17}$$

Matrix models. Models of distortion of the performed dimensions (7) of the scattering field (14, 15) are built under the assumption that the displacements of technological subsystems in the *y* direction are formed by the component of the cutting force p_y, and in the *x* direction - only p_x. This assumption is valid for rigid parts of small dimensions and with a ratio of overall dimensions L = D. In general cases, all components of the cutting force affect the coordinate displacements of technological subsystems. That is why the rigidity of the spindle and tailstock is taken into consideration, the rotation of the spindle is considered and the center of rotation is calculated [5]. These influences can be taken into account based on the general laws of analytical mechanics [3].

Since the cutting force during turning is a vector in three-dimensional space and the elastic displacements of technological subsystems under the action of this force are also described by a spatial vector, generalizing the coordinate Eqs. (7) to distort the dimensions performed, we can proceed to the vector Eq. [8-18]:

$$\bar{g} = \bar{c} \cdot \bar{p} \tag{18}$$

where g – vector of elastic displacement of the technological system; $\bar{p} = \begin{pmatrix} p_x \\ p_y \\ p_z \end{pmatrix}$ - vector of

cutting force; $\bar{c} = \begin{pmatrix} c_{xx} & c_{xy} & c_{xz} \\ c_{yx} & c_{yy} & c_{yz} \\ c_{zx} & c_{zy} & c_{zz} \end{pmatrix}$ - compliance matrix of technological system.

In the coordinate Eq.s (1, 2, 3, 5), the compliance of the technological system is characterized by its reciprocal value - rigidity (along the coordinate directions j_{yo1} and j_{xo1}). In terms of rigidity, the matrix *c* can be represented as:

$$\bar{c} = \begin{pmatrix} \frac{1}{j_{xx}} & \frac{1}{j_{xy}} & \frac{1}{j_{xz}} \\ \frac{1}{j_{yx}} & \frac{1}{j_{yy}} & \frac{1}{j_{yz}} \\ \frac{1}{j_{zx}} & \frac{1}{j_{zy}} & \frac{1}{j_{zz}} \end{pmatrix} \tag{19}$$

where j_{xx} and j_{yy} correspond to the stiffness along the x (j_{x01}) and y (j_{y01}) axis in the coordinate Eq.s. In the vector Eq. of the cutting force, one can use the traditional notation for the cutting theory for the coordinate components P_x, P_y, P_z.

$$p_i = c_i t^{x_i} s^{y_i} v^{z_i} \quad (i = \text{x, y, z}) \tag{20}$$

Taking into account the introduced notation (19, 20), expression (18) is a vector model of the distortion of the performed dimension. The distortion of the diametral dimension (distortion in the y direction) is described by the second component of the vector $\bar{g}$:

$$g_y = y = \frac{c_y t^{x_y} s^{y_y} v^{z_y}}{j_{yy}} + \frac{c_x t^{x_x} s^{y_x} v^{z_x}}{j_{yx}} + \frac{c_z t^{x_z} s^{y_z} v^{z_z}}{j_{yz}} \qquad (21)$$

the distortion of the linear dimension is described by the first component of the vector $\bar{g}$:

$$g_x = x = \frac{c_x t^{x_x} s^{y_x} v^{z_x}}{j_{xx}} + \frac{c_y t^{x_y} s^{y_y} v^{z_y}}{j_{xy}} + \frac{c_z t^{x_z} s^{y_z} v^{z_z}}{j_{xz}} \qquad (22)$$

Eqs. (21, 22) are a matrix generalization of coordinate Eqs. (7). The first terms in the generalized Eqs. represent the right-hand sides of Eqs. (7) and describe the direct influence of the cutting force component of the same name (force P_y on the diametral dimension - y, force P_x on the linear dimension - x). The remaining terms describe the indirect influence of other components of the cutting force.

To form a vector model of the scattering field, we consider, by analogy with expressions (11, 12), taking into account the notation (8, 9, 10), the expressions for fluctuations in the cutting force:

$$\max \; p_i = c_i \left(1 + \frac{v}{2}\right)\left(t + \frac{\Delta t}{2}\right)^{x_i} s^{y_i} v^{z_i} \quad (i = x, y, z) \qquad (23)$$

$$\min \; p_i = c_i \left(1 - \frac{v}{2}\right)\left(t - \frac{\Delta t}{2}\right)^{x_i} s^{y_i} v^{z_i} \quad (i = x, y, z) \qquad (24)$$

The maximum compliance of the technological system is described by the following matrix:

$$\max \; \bar{c} = \begin{pmatrix} \frac{1}{j_{xx}\left(1-\frac{\varepsilon}{2}\right)} & \frac{1}{j_{xy}\left(1-\frac{\varepsilon}{2}\right)} & \frac{1}{j_{xz}\left(1-\frac{\varepsilon}{2}\right)} \\ \frac{1}{j_{yx}\left(1-\frac{\varepsilon}{2}\right)} & \frac{1}{j_{yy}\left(1-\frac{\varepsilon}{2}\right)} & \frac{1}{j_{yz}\left(1-\frac{\varepsilon}{2}\right)} \\ \frac{1}{j_{zx}\left(1-\frac{\varepsilon}{2}\right)} & \frac{1}{j_{zy}\left(1-\frac{\varepsilon}{2}\right)} & \frac{1}{j_{zz}\left(1-\frac{\varepsilon}{2}\right)} \end{pmatrix} = \frac{1}{\left(1-\frac{\varepsilon}{2}\right)}\begin{pmatrix} \frac{1}{j_{xx}} & \frac{1}{j_{xy}} & \frac{1}{j_{xz}} \\ \frac{1}{j_{yx}} & \frac{1}{j_{yy}} & \frac{1}{j_{yz}} \\ \frac{1}{j_{zx}} & \frac{1}{j_{zy}} & \frac{1}{j_{zz}} \end{pmatrix} \qquad (25)$$

For minimal compliance, the matrix is transformed to the form:

$$\min \; \bar{c} = \begin{pmatrix} \frac{1}{j_{xx}\left(1+\frac{\varepsilon}{2}\right)} & \frac{1}{j_{xy}\left(1+\frac{\varepsilon}{2}\right)} & \frac{1}{j_{xz}\left(1+\frac{\varepsilon}{2}\right)} \\ \frac{1}{j_{yx}\left(1+\frac{\varepsilon}{2}\right)} & \frac{1}{j_{yy}\left(1+\frac{\varepsilon}{2}\right)} & \frac{1}{j_{yz}\left(1+\frac{\varepsilon}{2}\right)} \\ \frac{1}{j_{zx}\left(1+\frac{\varepsilon}{2}\right)} & \frac{1}{j_{zy}\left(1+\frac{\varepsilon}{2}\right)} & \frac{1}{j_{zz}\left(1+\frac{\varepsilon}{2}\right)} \end{pmatrix} = \frac{1}{\left(1+\frac{\varepsilon}{2}\right)}\begin{pmatrix} \frac{1}{j_{xx}} & \frac{1}{j_{xy}} & \frac{1}{j_{xz}} \\ \frac{1}{j_{yx}} & \frac{1}{j_{yy}} & \frac{1}{j_{yz}} \\ \frac{1}{j_{zx}} & \frac{1}{j_{zy}} & \frac{1}{j_{zz}} \end{pmatrix} \qquad (26)$$

The vector analogue of Eq. (11) - the maximum distortion of the dimension being performed - will be described, taking into account the notation (23 - 26), as follows:

$$\max \bar{g} = \frac{1}{\left(1-\frac{\varepsilon}{2}\right)}\bar{c}\begin{pmatrix} c_x\left(1+\frac{v}{2}\right)\left(t + \frac{x_x}{2}\Delta t\right)s^{y_x}v^{z_x} \\ c_y\left(1+\frac{v}{2}\right)\left(t + \frac{x_y}{2}\Delta t\right)s^{y_y}v^{z_y} \\ c_z\left(1+\frac{v}{2}\right)\left(t + \frac{x_z}{2}\Delta t\right)s^{y_z}v^{z_z} \end{pmatrix} = \frac{1+\frac{v}{2}}{1-\frac{\varepsilon}{2}}\bar{c}\left[\begin{pmatrix} c_x t s^{y_x}v^{z_x} \\ c_y t s^{y_y}v^{z_y} \\ c_z t s^{y_z}v^{z_z} \end{pmatrix} + \right.$$

$$+\frac{1}{2}\begin{pmatrix} c_x x_x \Delta t s^{y_x} v^{z_x} \\ c_y x_y \Delta t s^{y_y} v^{z_y} \\ c_z x_z \Delta t s^{y_z} v^{z_z} \end{pmatrix} \Bigg] = \frac{1+\frac{v}{2}}{1-\frac{\varepsilon}{2}}\bar{c}\left[\begin{pmatrix} c_x s^{y_x} v^{z_x} \\ c_y s^{y_y} v^{z_y} \\ c_z s^{y_z} v^{z_z} \end{pmatrix} + +\frac{\Delta t}{2}\begin{pmatrix} c_x x_x s^{y_x} v^{z_x} \\ c_y x_y s^{y_y} v^{z_y} \\ c_z x_z s^{y_z} v^{z_z} \end{pmatrix}\right] = \frac{1+\frac{v}{2}}{1-\frac{\varepsilon}{2}}\bar{c}\left[t\overline{p_t} + \frac{\Delta t}{2}\overline{p_{\Delta t}}\right] \quad (27)$$

Where vector $\overline{p_t} = \begin{pmatrix} c_x s^{y_x} v^{z_x} \\ c_y s^{y_y} v^{z_y} \\ c_z s^{y_z} v^{z_z} \end{pmatrix}$ characterizes the degree of influence of the depth of cut t,

vector $\overline{p_{\Delta t}} = \begin{pmatrix} x_x c_x s^{y_x} v^{z_x} \\ x_y c_y s^{y_y} v^{z_y} \\ x_z c_z s^{y_z} v^{z_z} \end{pmatrix}$ characterizes the degree of influence of allowance fluctuations.

Similarly, for the minimum distortion of the performed dimension, one can immediately write out the vector expression:

$$min\,\overline{g} = \frac{1-\frac{v}{2}}{1+\frac{\varepsilon}{2}}\bar{c}\left[t\overline{p_t} - \frac{\Delta t}{2}\overline{p_{\Delta t}}\right] \quad (28)$$

By analogy with expressions (14, 15), we obtain a vector expression for the scattering field:

$$\Delta g = \frac{1+\frac{v}{2}}{1-\frac{\varepsilon}{2}}\bar{c}\left[t\overline{p_t} + \frac{\Delta t}{2}\overline{p_{\Delta t}}\right] - \frac{1-\frac{v}{2}}{1+\frac{\varepsilon}{2}}\bar{c}\left[t\overline{p_t} - \frac{\Delta t}{2}\overline{p_{\Delta t}}\right] = \bar{c}\left\{t\overline{p_t}\left(\frac{1+\frac{v}{2}}{1-\frac{\varepsilon}{2}} - \frac{1-\frac{v}{2}}{1+\frac{\varepsilon}{2}}\right) + \frac{\Delta t}{2}\overline{p_{\Delta t}}\left(\frac{1+\frac{v}{2}}{1-\frac{\varepsilon}{2}} + \frac{1-\frac{v}{2}}{1+\frac{\varepsilon}{2}}\right)\right\} =$$

$$\left| \begin{array}{c} \dfrac{1+\frac{v}{2}+\frac{\varepsilon}{2}+\frac{v\varepsilon}{4}-1+\frac{v}{2}+\frac{\varepsilon}{2}-\frac{v\varepsilon}{4}}{1-\frac{\varepsilon^2}{4}} = v + \varepsilon = \omega \\[2mm] \dfrac{1+\frac{v}{2}+\frac{\varepsilon}{2}+\frac{v\varepsilon}{4}-1-\frac{v}{2}-\frac{\varepsilon}{2}-\frac{v\varepsilon}{4}}{1-\frac{\varepsilon^2}{4}} = 2 \end{array} \right| = \bar{c}\{\omega t\overline{p_t} + \Delta t\overline{p_t}\} \quad (29)$$

Expression (29) is a matrix generalization of the model of the scattering field of the performed dimensions. The transition to a specific dimension is reduced to considering the corresponding coordinate of the vector Δg. For example, for the magnitude of the scattering field of the diametrical dimension, the relation is true:

$$\Delta y = \Delta g_y \quad (30)$$

for a linear dimension we get:

$$\Delta x = \Delta g_x \quad (31)$$

Full-factor model of dimensional distortion. All models of machining error (distortions in dimensions, scattering fields of dimensions) formed in (7), (14, 15), (18), (29) take into account only plane-parallel movements of the subsystems of the technological system along the coordinate axes of the Cartesian coordinate system X, Y, Z. Such an approach to modeling the process of formation of machining errors is acceptable for parts that have overall dimensions of the same order in all coordinate directions. However, in practice, it is not uncommon for turning operations to machine parts with overall dimensions that differ significantly in different directions. For example, long shafts (predominant linear dimension), disks and flanges (predominant diametrical dimension). In these cases, a significant contribution to the machining error can be made by the rotation of the workpiece, especially in the directions of the prevailing overall dimensions.

The need to take into account the angular displacements of the workpiece under the action of

cutting forces was pointed out in the works of A.P.Sokolovsky, V.S.Korsakov, D.D.Medvedev and others. [3]. They offer even the simplest analytical dependences for calculating these angular displacements. However, all these dependences are of a particular nature, they include a number of parameters, the determination of which in practice is associated with insurmountable difficulties. For example, the center of rotation of the spindle is generally a virtual object that cannot be practically measured. Most importantly, these models do not agree with the general laws of the mechanics of elastically deformable systems. Therefore, they cannot be used to build a unified theory of machining accuracy, taking into account the possible angular displacements of the subsystems of the technological system.

As is known from analytical mechanics, a body in space has 6 degrees of freedom:

-3 plane-parallel movements along the coordinate axes X, Y, Z;

- 3 rotations around each of the coordinate axes [9, 13, 15].

Fixing the position of a rigid body in space is carried out by imposing constraints on each degree of freedom. Three bonds limit the plane-parallel movement along the corresponding coordinate axes and three bonds limit the angular displacement of the body around each of the coordinate axes. The level of restriction of the freedom of movement of the body, created by the superimposed connection, is characterized by the rigidity of the connection, or its reciprocal value - the compliance of the connection.

In [9, 13, 15], to describe the displacements of a body in space, taking into account all six degrees of freedom, its position is given by two parameters (Fig. 3) [4]:

- point O (x_0; y_0; z_0) belonging to the body;

- vector $\bar{l}$ of unit length, belonging to the body and directed, for example, along its prevailing direction.

All plane-parallel displacements of the body are characterized by displacements of point O. The angular displacements of the body are described by rotations of the vector $\bar{l}$ around the point O.

The movements of the body occur as a result of the force $\bar{F}$ applied at point A (x, y, z), also belonging to the body.

Let the vector $\bar{r} = (r_x, r_y, r_z)$ be the plane-parallel displacement of the point O, the vector $\bar{\omega} = (\omega_x, \omega_y, \omega_z)$ the angle of rotation of the body, and formally the vector $\bar{l}$, which specifies the orientation of the body in space, relative to the point O. Here r_x, r_y, r_z - are movements along the coordinate axes, ω_x, ω_y, ω_z - are rotation angles around the corresponding coordinate axes.
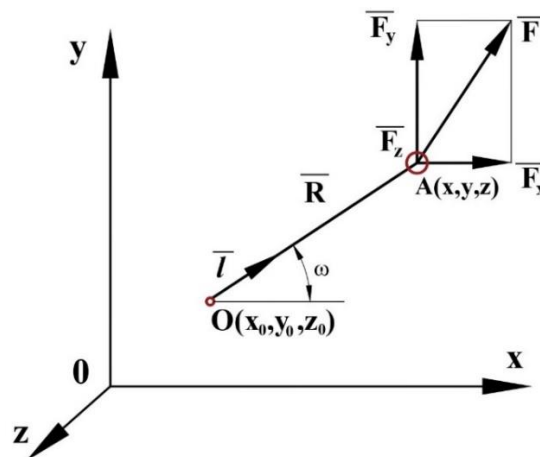
Fig. 3. Design scheme of body displacements under the action of an applied force, taking into account six degrees of freedom [4]

Then the total displacement u of point A is made up of a plane-parallel displacement and an angular displacement:

$$\bar{u} = \bar{r} + \bar{\rho} \tag{32}$$

where the second term describes exactly the angular displacements of the point A:

$$\bar{\rho} = \bar{\omega} \times \bar{R} \tag{33}$$

Vector $\bar{R}$ specifies the orientation of point A (point of application of force $\bar{F}$) relative to point O. It is with respect to this point that the angular displacements of point A are considered:

$$\bar{R} = \overline{OA} = \{x - x_0;\ y - y_0;\ z - z_0\} \tag{34}$$

The plane-parallel displacement of the point O under the influence of the force $\bar{F}$, taking into account the compliance of the superimposed bonds, is determined, in accordance with Eqs. (318), as:

$$\bar{r} = e\bar{F} \tag{35}$$

where e is the compliance matrix $\bar{e} = \begin{pmatrix} e_{xx} & e_{xy} & e_{xz} \\ e_{yx} & e_{yy} & e_{yz} \\ e_{zx} & e_{zy} & e_{zz} \end{pmatrix}$

In coordinate form, Eq. (3.329) takes the form:

$$\begin{pmatrix} r_x \\ r_y \\ r_z \end{pmatrix} = \begin{pmatrix} e_{xx} & e_{xy} & e_{xz} \\ e_{yx} & e_{yy} & e_{yz} \\ e_{zx} & e_{zy} & e_{zz} \end{pmatrix} \begin{pmatrix} F_x \\ F_y \\ F_z \end{pmatrix} \tag{36}$$

The rotation angles given by the vector $\bar{\omega}$ are determined by the angular compliance matrix. $\xi = \begin{pmatrix} \xi_{xx} & \xi_{xy} & \xi_{xz} \\ \xi_{yx} & \xi_{yy} & \xi_{yz} \\ \xi_{zx} & \xi_{zy} & \xi_{zz} \end{pmatrix}$ The governing Eq. is constructed in the image of the Eq. for plane-parallel displacements (18), but instead of force, the moment of force $\bar{M}$ is involved in it:

$$\bar{M} = \bar{R} \times \bar{F} \tag{37}$$

Then for the rotation of the vector $\bar{l}$, which characterizes the orientation of the body in space, we obtain, by analogy with (35):

$$\bar{\omega} = \xi\bar{M} = \xi \cdot (\bar{R} \times \bar{F}) \tag{38}$$

In coordinate form, this Eq. has the form:

$$\begin{pmatrix} \omega_x \\ \omega_y \\ \omega_z \end{pmatrix} = \begin{pmatrix} \xi_{xx} & \xi_{xy} & \xi_{xz} \\ \xi_{yx} & \xi_{yy} & \xi_{yz} \\ \xi_{zx} & \xi_{zy} & \xi_{zz} \end{pmatrix} \begin{vmatrix} i & j & k \\ x - x_0 & y - y_0 & z - z_0 \\ F_x & F_y & F_z \end{vmatrix} \tag{39}$$

For the unity of the form of the Eq.s, it is advisable to bring the moment vector $\overline{M}$ (37), given as a vector product $(\bar{R} \times \bar{F})$, into a matrix form:

$$\begin{vmatrix} i & j & k \\ x - x_0 & y - y_0 & z - z_0 \\ F_x & F_y & F_z \end{vmatrix} = \begin{pmatrix} 0 & -(z - z_0) & y - y_0 \\ z - z_0 & 0 & -(x - x_0) \\ -(y - y_0) & x - x_0 & 0 \end{pmatrix} \begin{pmatrix} F_x \\ F_y \\ F_z \end{pmatrix} \qquad (40)$$

Then Eq. (39) for the rotation angles is reduced to the form:

$$\begin{pmatrix} \omega_x \\ \omega_y \\ \omega_z \end{pmatrix} = \begin{pmatrix} \xi_{xx} & \xi_{xy} & \xi_{xz} \\ \xi_{yx} & \xi_{yy} & \xi_{yz} \\ \xi_{zx} & \xi_{zy} & \xi_{zz} \end{pmatrix} \begin{pmatrix} 0 & -(z - z_0) & y - y_0 \\ z - z_0 & 0 & -(x - x_0) \\ -(y - y_0) & x - x_0 & 0 \end{pmatrix} \begin{pmatrix} F_x \\ F_y \\ F_z \end{pmatrix} \qquad (41)$$

In folded form, it can be written as:

$$\bar{\omega} = \xi a_0 \bar{F} \qquad (42)$$

where a special representation is introduced for the vector $\bar{R} = \overline{OA}$ in the form of a matrix:

$$a_0 = \begin{pmatrix} 0 & -(z - z_0) & y - y_0 \\ z - z_0 & 0 & -(x - x_0) \\ -(y - y_0) & x - x_0 & 0 \end{pmatrix} \qquad (43)$$

In accordance with Eq. (43), the angular displacements of the point A, due to the rotation of the direction vector $\bar{l}$, are determined as the vector product $\bar{\omega} \times \bar{R}$. If we use the representation of the vector $\bar{R}$ in the form of a matrix a_0 (43), then it is impossible to directly perform the vector multiplication $\bar{\omega} \times \bar{R}$ (multiplying a vector by a matrix). Therefore, we first determine the opposite vector $\bar{R} \times \bar{\omega}$ (here, the matrix a_0 is multiplied by the vector $\bar{\omega}$). Taking into account (43), we have $\bar{R} \times \bar{\omega} = a_0 \xi a_0 \bar{F}$. Since the relation $\bar{\omega} \times \bar{R} = -\bar{R} \times \bar{\omega}$ is valid, expression (33) for the angular displacements of the point A will take the form:

$$\bar{\rho} = -a_0 \xi a_0 \bar{F} \qquad (44)$$

For the total displacement of point A (plane-parallel displacement r of the base point O and displacement ρ due to rotation around the point O), in accordance with (3.227), we obtain:

$$\bar{u} = (e - a_0 \xi a_0)\bar{F} \qquad (45)$$

This Eq. describes the elastic displacement of the body from the action of the force $\bar{F}$ taking into account the whole complex of factors characterizing the compliance of the bonds that fix the position of the body in space. We can call this movement full-factorial. The matrix e in this Eq. characterizes the compliance of the bonds that limit the plane-parallel movement of the body. Then the product of three matrices $-a_0 \xi a_0$ can be interpreted as the effective angular compliance matrix for point A. It characterizes the flexibility of the bonds that limit the angular displacement of point A relative to point O.

Conclusion. Matrix models of machining error in single-tool setups with a spatial arrangement of the tool are developed, taking into account the simultaneous action of all components of the cutting forces of the setup tool and elastic deformations of the technological system in all coordinate directions. These models are developed both in the distortion models of performed dimensions and in the scattering field models. A full-factor model of dimension distortion for single-carriage adjustment (setup) has been developed, which allows taking into account not only plane-parallel

movements of technological subsystems, but also their angular movements around base points. Therefore, we believe that Eq. (45) can be used as the basis for a full-factor model of machining error. To do this, we first transform the analytical models of the elastic contact interaction of systems of bodies (18) to the level of full factorial ones. Analytical models (7), (14,15), (18) and (19) describe only plane-parallel displacements of contacting bodies. To take into account the entire range of movements in them, i.e. and angular displacements, it is sufficient to replace the plane-parallel displacement vectors of each contacting body $\overline{r_i}$ with the total displacement vectors $\overline{u_i}$. By applying the developed models to specific machining schemes, the issues of improving machining quality and productivity can be investigated through the management of technological parameters in adjustments used in modern CNC machines with wide technological capabilities. Also, within the technological capabilities of CNC machines, the issues of researching processing quality and durability of the cutting tool with various combinations of technological transitions, developing control matrix models of cutting conditions by fulfilling the requirement for the accuracy of dimensions in adjustments can be investigated.

REFERENCES

[1]. Koshin A.A., Yusubov N.D. *Matrix generalization of the theory of accuracy of turning processing*. Journal «Bilgi» series Technique, 2003, 2, pp. 31−41.

[2]. Kosilova A.G., Meshcheryakov R.K. *Handbook of a mechanical engineering technologist volume 2*, Mechanical engineering, 1986, Moscow.

[3]. Yusubov N. *Multi-tool machining on automatic lathes (Matrix theory of multi-tool machining accuracy on modern CNC lathes)*. AV Akademikerverlag Gmbh & Co. KG, 2013, LAP LAMBERT Academic Publishing, Saarbrücken.

[4]. Yusubov N.D., Abbasova H.M. *Full Factorial Models of Dimensional Accuracy of Multi-Tool Machining on Automatic Turning Machines*. Bulletin of the South Ural State University. Ser. Mechanical Engineering Industry, 2019, vol. 19, no. 1, pp. 56–67.

[5]. Koshin A. *Precision theory and optimization of multi-tool turning*. Dissertation, 1997, University of Chelyabinsk.

[6]. Kudinov V.A. *Machine tool dynamics*, Mechanical engineering, 1967, Moscow.

[7]. Screw-cutting and turning machines. GOST 18097, 1988, Standards Publishing House, Moscow.

[8]. Yusubov N., Movlazade V., Abbasova H. *Accuracy models of machining in multi-tool adjustments*. Proceedings of the 8th International Conference on Control and Optimization with Industrial Applications (COIA 2022), 2022, vol. 2, pp. 477-479.

[9]. Yusubov N.D. *Matrix full-factor model of dimension distortion performed in multi-tool adjustments*. Mechanical engineering. 2008, 1(65), pp.36-39.

[10]. Yusubov N.D. *Matrix models of working accuracy at single-cutter turning.* Journal Tekhnologiya Mashinostroeniya, 2009, 1, pp.41−45.

[11]. Yusubov N.D. *Practical applicability of matrix models of processing accuracy*. Mashinostroitel, 2009, no.2, pp. 37-40.

[12]. Yusubov N.D. Bagirova H.M. *Full factorial matrix models of dispersion fields of the carried out sizes in multi-tools of two-support adjustments*. Modern science-intensive technologies: development priorities and personnel training: Collection of articles of the international scientific-practical conference, 2014, pp.132-137.

[13]. Yusubov N.D., Abbasova H.M. *Full-factor matrix model of accuracy of dimensions performed on multi-purpose CNC machines.* Obrabotka metallov (tekhnologiya, oborudovanie, instrumenty), Metal Working and Material Science, 2021, vol. 23, no. 4, pp. 6–20.

[14]. Yusubov N.D., Abbasova H.M. *Process control model for single-tool adjustments*. 14th international scientific and technical conference "Technological support and quality improvement of mechanical engineering and aerospace products" Bryansk, 2022, pp.95-99.

[15]. Yusubov N.D., Bagirova H.M. *Full-factor model of distortion of the sizes multi-tools two-support adjustments.* Machine science, 2013, no3, pp. 43-48.

[16]. Yusubov N., Abbasova H., Khankishiyev I. *Entwicklung einer Projektierungstheorie für die Mehrwerkzeugbearbeitung mit den Möglichkeiten der modernen CNC-Werkzeug-maschinen.* Forschung im Ingenieurwesen, 2021, 85, pp. 661–678.

[17]. Yusubov N.D. *Matrix Models of the Accuracy in Multitool Two-Support Setup.* Russian Engineering Research, 2009, vol. 29, no. 3, pp. 268-271.

[18]. Koshin A.A., Yusubov N.D. *Analytical foundations of models of force interaction of subsystems of a technological system in cutting processes.* Modern problems of mechanical engineering and instrumentation. Reports of the international scientific and technical conference, Baku, 2005, pp. 67-70.

FEATURES OF PROCESSING AND ASSEMBLY OF COMPOSITE PRODUCTS

Igor DERYABIN[1*], Viktor GUZEEV[2], Alexander KOZLOV[3], Dmitrii ARDASHEV[4]

[1,3]Zlatoust branch of South Ural State University, Department of Engineering Technology, Zlatoust, Russian Federation
[2,4]South Ural State University, Department of the Technology of Automated Mechanical Engineering, Chelyabinsk, Russian Federation

E-mail: deriabin-ip@susu.ru[1], guzeevvi@susu.ru[2], kozlovav@susu.ru[3], ardashevdv@susu.ru[4]

Abstract: The paper examines the assembling of cylindrical products consisting of sector parts with dihedral angles. A crucial issue in the assembly of such parts is the accuracy of dihedral angles during processing. Based on methods of analytical geometry, we proved that in order to achieve gapless assembly of three sectors, the sum of all dihedral angles of the sectors should be less than or equal to 360°. Since it is impossible to ensure the exact equality of the sum of all dihedral angles of 360°, characteristic "flatness deviation" is always formed during assembly. In order t obtain a gapless connection, we propose a new method for the selective assembly of sectors and developed a scheme of the dihedral angle controller. This selective assembly method will allow sectors to be selected in such a way that their "twist" angle in the assembled conditions is minimal.

Keywords: assembly technology, sector parts, dihedral angle control, conditions for gapless connection of three sectors.

Introduction. Product quality, reliability, and durability depend on the accuracy of mating parameters. This can be increased by:

– Increasing the accuracy (reducing tolerances) of the surface treatment of mating parts that form the product;

– Selective assembly based on the complete interchangeability method.

The first option is largely related to the resources of technological equipment. Therefore, in some cases, when these resources are exhausted, then selective product assembly is important. Its essential objectives are to complete and obtain assembly kits. Most of the existing methods are designated for the assembly of two shaft-sleeve parts, i.e., mating of the female face to the male face. The assembly of three or more parts is underexplored. Additional difficulties arise when mating open surfaces, for example, the planes of dihedral angles.

The processing of composite products has its own specific features associated with the errors of some parameters. This is relevant both for the parts themselves and the assembled product [1–4]. Such products include propellers, turbine blades, some types of projectiles, etc. Let us consider these features using the example of processing and assembly of a product consisting of 3-sector parts (hereinafter referred to as sectors) (Fig. 1a). The main sector processing errors which affect the product assembly are errors of the dihedral angle ψ (Δψ is the angle processing tolerance) and the errors of the arc radius R (Fig. 2b).

In order to determine the capabilities of the sector assembly process, let us analyze the conditions for the unambiguous positioning of the assembled form and the very capability of assembling sectors without a gap between the planes of the dihedral angle.

If all the dihedral angles of the sectors ψ are exactly equal to 120°, then we can assume that gapless binding is possible with small deviations from the flat surface accuracy of their side faces (Fig. 1a). In this case, the edges of the side faces are strictly parallel to each other. However, the gapless state during assembly does not per se mean that the mutual position is unambiguous (Fig.

2). Even in the ideal case, i.e. when assembling reference parts, complete unambiguity cannot be achieved either with a three-jaw chuck (Fig. 2a), or with hoops. For example, in the latter case, if the radius of one of the sectors is larger than the radius of the other sectors, then Fig. 2b is possible. When positioning in a three-jaw chuck, any of the positions shown in Fig. 2a can be fixed.
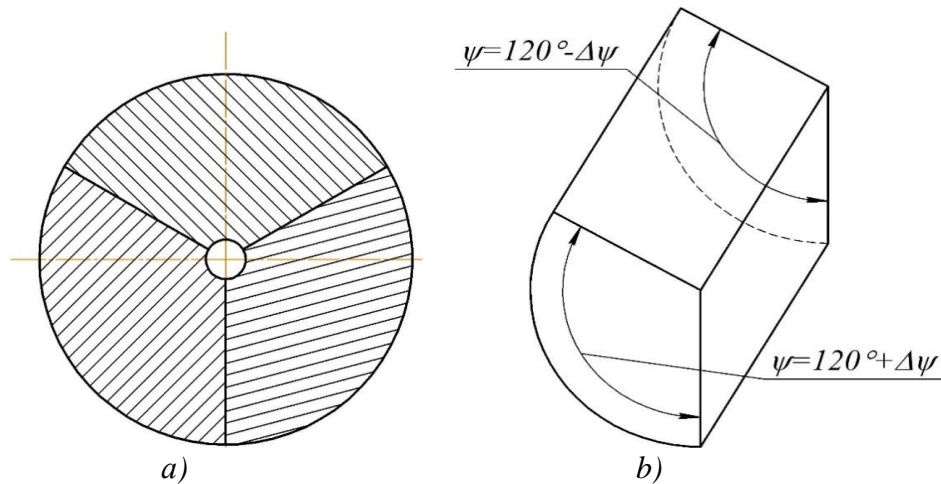
a)   *b)*
Fig. 1. Composite product
a) – sector assembly b) – dihedral angle errors
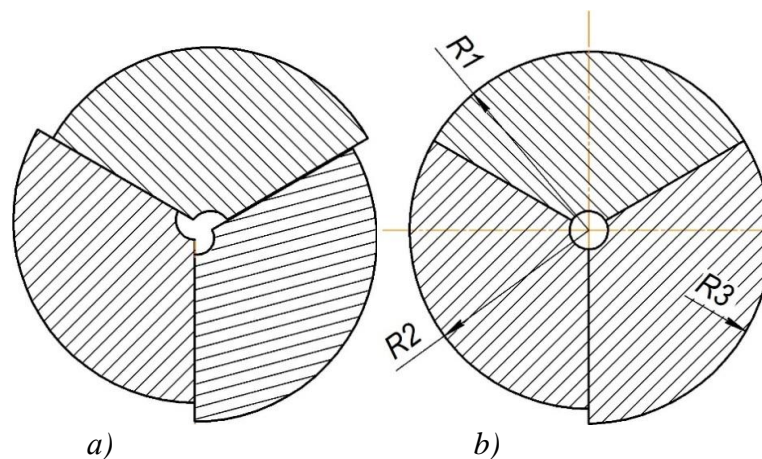
a)   *b)*
Fig. 2. Sector assembly options
a) assembly of reference ("ideal") sectors, b) assembly of sectors with a radius error

Another sector assembly problem is the failure to make absolutely accurate dihedral angles, i.e. angles exactly equal to 120° [5–9]. Let us consider what happens, if the sum angle of the three sectors is less than or more than 360° (Fig. 3). If the sum angle exceeds 360° (Fig. 3b), then assembly is impossible, since it is impossible to ensure engagement of the dihedral angle planes. If the sum angle is less than 360° (Fig. 3c), then assembly is possible but with a noticeable twist angle or "flatness deviation" of the assembled sectors (Fig. 3d), as well as assembly ambiguity before and after processing.

It can be proved mathematically that with a total positive tolerance for sector angles, the product cannot be assembled, while with a total negative tolerance, the product can be assembled. All planes are guaranteed to be tightly stacked on top of each other, but strongly "twisted". This causes major problems both during assembly and control, as well as processing stages of the assembled product (in a satellite device) [10–20]. A dihedral angle controller can be designed based on this principle.

Product assemblability analysis. Gapless assembly does not always ensure the engagement of all three sectors with an angular dimension strictly equal to 120°. Let us assume that the side faces of the sectors are ideally flat. Without loss of generality and for convenient consideration, we

can assume that two of the three sectors have dihedral angles exactly equal to 120°. The third sector has a deviation of 120° (Fig. 4) equal to the total defect of the angle of all the three real sectors. This assumption does not result in a significant error due to the small deviations of the angular dimensions of real sectors.
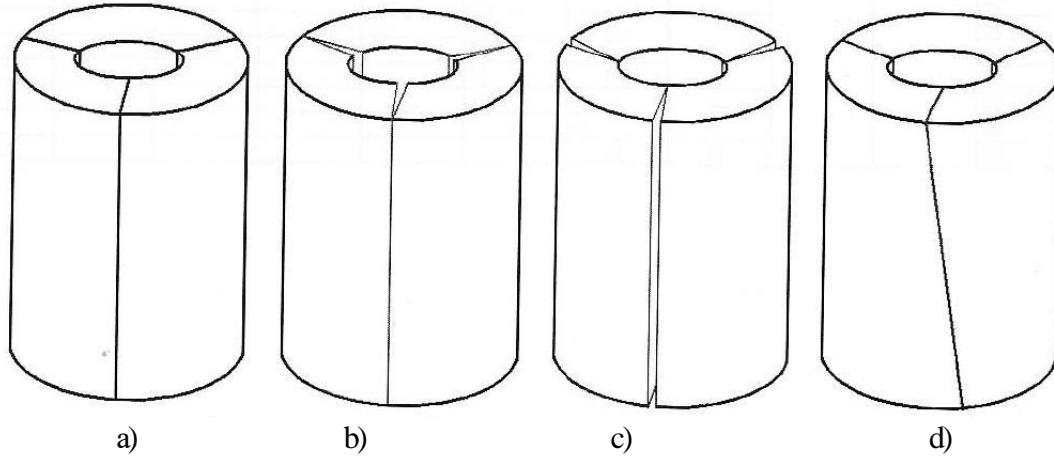
Fig. 3. Assembly options at different tolerances for dihedral angles
a) 3ψ=360°;   b) 3ψ > 360°   c) 3ψ < 360°   d) 3ψ < 360°
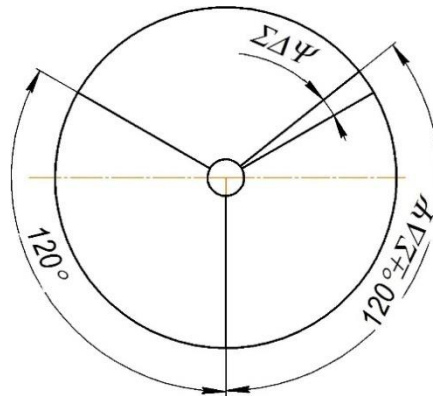
Fig. 4. Assembly with an angle error of one of the sectors

Let two sectors with angular dimensions of 120° contact along a common plane (Fig. 5a). If these sectors are given a small angle of rotation α along the contact plane, then the dihedral angle formed by the other planes of these sectors will differ from 120° (Fig. 5b). Therefore, the third sector with a dihedral angle different from 120° can have gapless contact with them.

Let us make the equations of nonadjacent planes of sectors 1 and 2:

$$3Z - \sqrt{3} \cdot Y = 0 \tag{1}$$

$$3Z + \sqrt{3} \cdot Y = 0 \tag{2}$$

Let us rotate sector 2 around the Y axis by the angle α. Then, in the new coordinate system related to this sector, the equations of non-adjacent planes will take the form:

$$3Z' - \sqrt{3} \cdot Y' = 0 \tag{3}$$

$$3(X'\sin\alpha + Z'\cos\alpha) + \sqrt{3} \cdot Y' = 0 \tag{4}$$

Let us find the dihedral angle between the non-adjacent planes using the analytical geometry formula:

$$\cos\psi = \pm\frac{0\times 3\times \sin\alpha + \sqrt{3}\times\sqrt{3}+3\times\cos\alpha\times(-3)}{\sqrt{0^2+3^2+3}\times\sqrt{3^2\sin^2\alpha+3+3^2\cos^2\alpha}}=\pm\frac{3-9\cos\alpha}{12} \tag{5}$$

Equation (5) implies that if $\alpha{=}0$, $\cos\psi = -\frac{1}{2}$, and if $\alpha{\neq}0$, $\psi < 120°$.

Thus,

$$\psi = \arccos(\frac{1-3\cos\alpha}{4}) \tag{6}$$

The rotation angle α is determined from the equation

$$\alpha = \arccos(\frac{1-4\cos\psi}{3}) \tag{7}$$

In the manufacturing of these products, the following tolerance was set experimentally. It was based on processing capabilities for the angle $\psi = 119,5°\pm15'$, i.e.. $\psi_{max}{=}119°45'$, $\psi_{min}= 119°15'$. At such values of the angle ψ, the rotation angle of the sectors is $\alpha \approx 5°…10°$.

Thus, in the case of gapless assembly of three sectors, the sum of all dihedral angles of the sectors should be less than or equal to 360°. Since it is impossible to ensure that the sum of all dihedral angles is exactly equal to 360°, a characteristic "flatness deviation" is always formed during assembly (Fig. 3d). Furthermore, the "propeller" can be twisted both clockwise and counterclockwise. When turning along the outer surface of the sector assembly, the tangential components of the cutting forces can "untwist" the assembly depending on the direction. Then the gap ΔS is formed on the outer surface of the product (Fig. 6).
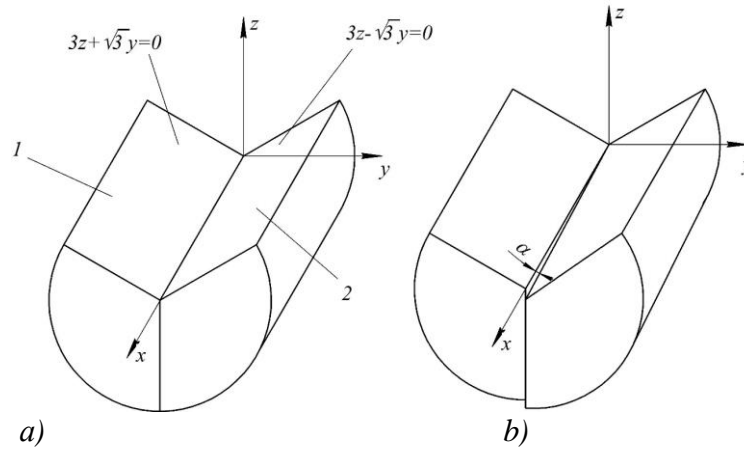
Fig. 5. Assembly of two sectors

For example, with the deviation of the angle of each sector of $-10'$, and the total deviation $\Delta\psi$ of $-30'$, a gap appears during untwisting

$$\Delta S = (R-r)\frac{0,5\pi}{360} \tag{8}$$
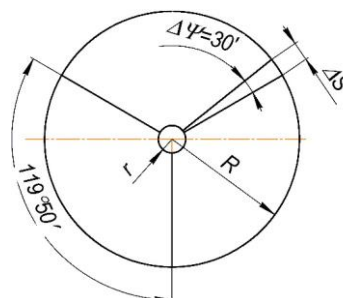
Fig. 6. The appearance of a gap when the assembly is "untwisted" during cutter turning

When assembling sectors with angles $\psi < 120°$, a radial motion variation ΔR may appear. This is due to the radial throw of the sectors (Fig. 7). When the angle is $\psi = 119.5°\pm15'$, the radial motion variation can reach $\Delta R = 0.43$mm, exceeding the allowable value $T = 0.2$mm for these products.
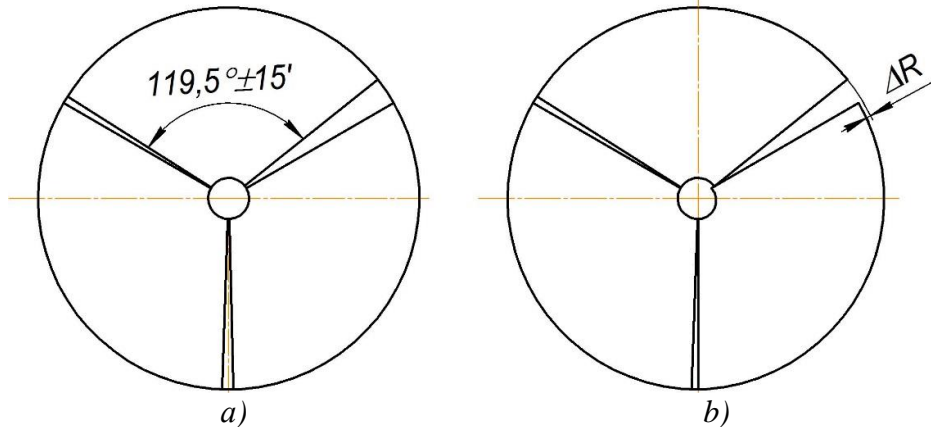
Fig. 7. Appearance of the radial motion variation during sector assembly
a) sector assembly at $\psi = 119,5°\pm15'$, b) radial throw of one of the sectors

Statistical studies carried out on a batch of 30 parts showed that the allowable value of the radial motion variation was exceeded in 27% of the parts (Fig. 8).

The following actions are essential to reduce the above-mentioned assembly errors:

1) Significantly reduce the tolerance for the dihedral angle in the manufacture of sectors;

2) Apply selective assembly using a special control device, which will significantly reduce the total defect of dihedral angles without reducing their processing tolerance.
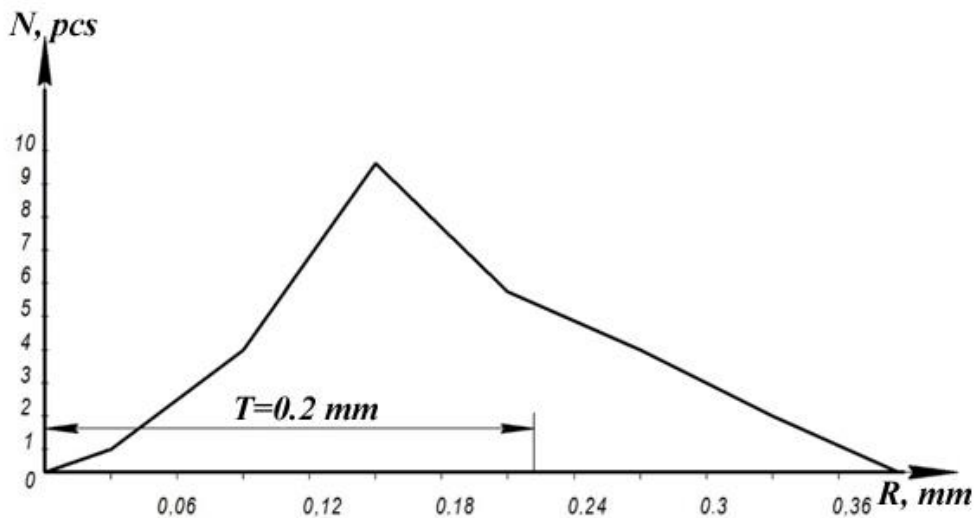
Fig. 8. Results of the radial motion variation measurement

Conclusion. We developed a scheme of a dihedral angle controller for selective assembly (Fig. 9). Sector 1 is mounted on a prism consisting of two "semi-prisms": fixed 2 and rotary 3. By turning "semi-prism" 3 around axis 5, we obtain snug engagement of the planes of "semi-prism" 3 and sector 1. We fix the resulting position of "semi-prism" 3 using adjusting screw 4, and measure the angle of rotation with a goniometer or any other measuring device.

Such control and selective assembly will allow sectors to be selected in such a way that their "twist" angle in the assembled condition is minimal. In this case, when selecting sectors, we can set the clockwise or counterclockwise "twisting" direction, depending on the direction of the cutting forces.
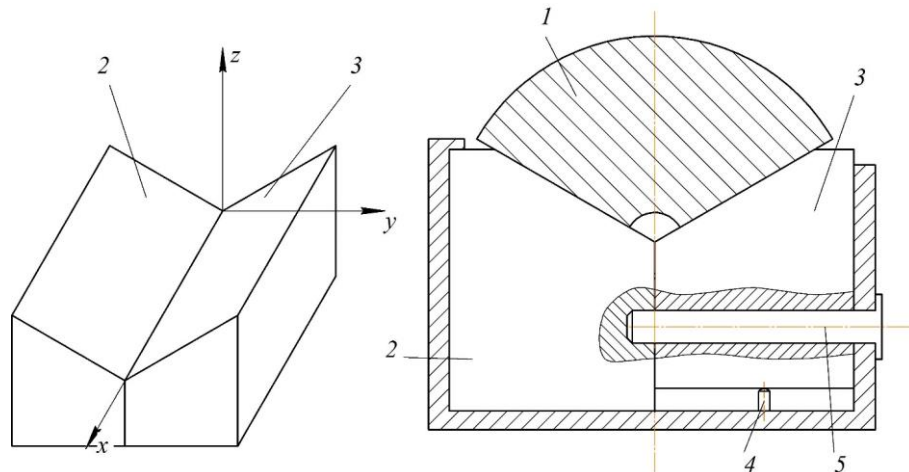
Fig. 9. Scheme of the dihedral angle controller
1 – sector, 2 – fixed "semi-prism", 3 – rotary "semi-prism", 4 – adjustable stop, 5 – axis

REFERENCES

[1]. Zhetesova, G.S., Yurchenko, V.V., Nikonova, T.Yu., Zharkevich O.M., Modelina E.D. *Features of positioning when controlling the accuracy of the machine fixture—tool—part system*. Technology of Mechanical Engineering, 2020, no. 1, pp. 34–42. (in Russ.)

[2]. Bazrov, B.M., Gaynutdinov, T.M. *Factors influencing the choice of technological bases in the manufacture of parts*. Mechanical Engineering Bulletin, 2020, no. 1, pp. 48–51. (in Russ.)

[3]. Bazrov, B.M., Gaynutdinov T.M. *Determination of the minimum number of technological bases of a part*. Mechanical Engineering Bulletin, 2020, no. 9, pp. 73–75. DOI: 10.36652/0042-4633-2020-9-73-75. (in Russ.)

[4]. Filipovich, O.V. *Simulation model of the selective assembly of three elements with sorting by estimated values*. Assembly in Mechanical Engineering and Instrumentation Engineering, 2022, no. 1, pp. 14–17. DOI: 10.36652/0202-3350-2022-23-1-14-17. (in Russ.)

[5]. Rudneva, L.Yu., Pankratova, T.A. *Improving the quality of manufacturing and assembly control of precision mechanics units*. Assembly in Mechanical Engineering and Instrumentation Engineering, 2022, no. 2, pp. 62–64. DOI: 10.36652/0202-3350-2022-23-2-62-64. (in Russ.)

[6]. Vodolazskaya, N.V. *Theoretical foundations for choosing tooling parameters for the assembly process*. Assembly in Mechanical Engineering and Instrumentation Engineering, 2021, no. 5, pp. 198–200. DOI: 10.36652/0202-3350-2021-22-5-198-200. (in Russ.)

[7]. Zadorina, N.A., Nepomiluev, V.V. *Ensuring the quality of assembly of high-precision products based on the method of individual selection of parts*. Assembly in Mechanical Engineering and Instrumentation Engineering, 2020, no. 4, pp. 152–157. DOI: 10.36652/0202-3350-2020-21-3-152-157. (in Russ.)

[8]. Zadorina, N.A., Nepomiluev, V.V., Oleinikova, E.V. *Individual selection of parts during assembly as an alternative to the need to improve their processing accuracy*. Assembly in Mechanical Engineering and Instrumentation Engineering, 2019, no. 5, pp. 225–230. (in Russ.)

[9]. Sorokin, M.N. *Selective assembly: problems and prospects*. Assembly in Mechanical Engineering and Instrumentation Engineering, 2016, no. 5, pp. 3–7. (in Russ.)

[10]. Nepomiluev V.V., Oleinikova E.V., Timofeev M.V. *Ensuring the stability of the assembly process based on the method of individual selection of parts*. Assembly in Mechanical Engineering and Instrumentation Engineering, 2015, no. 11, pp. 7–12. (in Russ.)

[11]. Spiridonov, O.V. *Analysis of the connection of parts in the development of technological assembly parts.* Assembly in Mechanical Engineering and Instrumentation Engineering. 2014, no. 1, pp. 19–23. (in Russ.)

[12]. Ivanov, A.A. *Methods for positioning mating parts during assembly.* Assembly in Mechanical Engineering and Instrumentation Engineering, 2014, no. 11, pp. 14–19.

[13]. Nazaryev, A.V., Bochkarev, P.Yu. *Ensuring the effective assembly of high-precision products of mechanical engineering and instrumentation engineering.* Science-Intensive Technologies in Mechanical Engineering, 2016, no. 12, pp. 28–35.

[14]. Bazrov, B.M. *The problem of assessing the geometric accuracy of a part.* Science-Intensive Technologies in Mechanical Engineering, 2018, no. 4, pp. 8–12.

[15]. Polsky, E.A. *Ensuring the reliability of high-tech assembly units.* Science-Intensive Technologies in Mechanical Engineering, 2018, no. 11, pp. 24–30.

[16]. Booker, J.D., Swift, K.G., Brown, N.J. *Designing for assembly quality: Strategies, guidelines and techniques.* Journal of Engineering Design, 2005, 16(3), pp. 279-295. DOI: 10.1080/09544820500126672

[17]. Judt, D., Lawson, C., Lockett, H. *Experimental investigation into aircraft system manual assembly performance under varying structural component orientations.* Proceedings of the Institution of Mechanical Engineers, Part B: Journal of Engineering Manufacture, 2020, 234 (4), pp. 840-855.
http://pib.sagepub.com/content/by/year DOI: 10.1177/0954405419883047

[18]. Wu, T., O'Grady P. *A concurrent engineering approach to design for assembly.* Concurrent Engineering Research and Applications, 1999, 7(3), pp. 231-243. DOI: 10.1177/1063293X9900700305

[19]. Hsu, H.-Y., Lin, G.C.I. *A design-for-assembly-based product redesign approach.* Journal of Engineering Design, 1998, 9(2), pp. 171-195.

[20]. Gerhardt, D.J., Hutchinson, W.R., Mistry, D.K. *Design for manufacture and assembly: Case studies in its implementation.* The International Journal of Advanced Manufacturing Technology, 1991, 6 (2), pp. 131-140. DOI: 10.1007/BF02601436

COMPARATIVE SERVICE LIFE ANALYSIS FOR WORM GEARS ACCORDING TO DIFFERENT FAILURE CRITERIA

Iftikhar CHALABI

Department of Mechatronics and Machine Design of Azerbaijan Technical University, Baku, Azerbaijan

E-mail: i_chalabi@aztu.edu.az

Abstract: In this paper, a comparative analysis of the service life of worm gear wheels for various failure criteria is carried out. Based on this analysis, a method is proposed for selecting the worm gear wheel material, the values of the modulus, on which the bending strength of the teeth depends. Research has shown that increasing the bending strength of teeth is of great practical importance, both for one-sided and two-sided loads. This also makes it possible to significantly increase the lifetime of one-side loaded gear wheels by replacing their working flanks with non-working ones. it was proposed to replace the working surfaces of the teeth of worm wheels after a certain service life.

Keywords: Worm gear, service life, failure, pitting, tooth breakage, wear

Introduction. Worm gears are very widely used in the structure of many machines and equipment, because they have a large gear ratio, high kinematic accuracy, smooth and silent operation compared to other mechanical transmissions. One of the disadvantages of these gears is the high cost of their material and manufacture. Therefore, the implementation of preventive measures to prevent premature failures and increase the service life of the worm gear is very important.

The reasons for the failure of worm gears are very various. The type of failure generally depends on many factors, such as operating conditions, material properties, geometric dimensions, manufacturing accuracy, etc. For timely elimination of possible failure to the worm gears, as well as increasing the service life, it is particularly important to choose the right materials and geometric dimensions at the design stage and conduct regular maintenance work during lifetime.

In the considered literature [1–5], calculations of worm gears based on the main failure criteria are usually considered separately. And in this case, the corresponding designed life of worm gears for different failure criteria are not compared. Therefore, in most cases, it is not possible to judge which type of failure to the worm gears is more likely and may occur earlier than others. Some types of failure (for example, teeth breakage) are the most dangerous. And other types of worm gear's failure (for example, pitting on the teeth) do not always lead to complete destruction of the worm gear, and they can in some cases be prevented in various ways. Therefore, a comparative lifetime analysis for worm gears according to different failure criteria can be of great practical importance.

In [6, 7], the bending strength of the teeth of various worm gears is studied by modern methods. However, the assessment of the strength and service life of worm gears by other failure criteria is not considered. And in works [8-11], studies of worm gears are carried out according to the criteria for failure of the working flanks of the teeth. A comparative analysis of the service life of worm gears for various failure criteria in these works is also not considered.

An analysis of the literature on worm gears has shown that a comparative analysis of their service life for various failure criteria has not yet been considered. Such an analysis can be of great practical significance, and therefore, this paper is devoted to this important task.

Formulation of problem. The types of damage occurring on the worm gear tooth (Fig. 1) can be divided into two groups. The first group includes flank damage such as pitting, wear, scuffing and grooving, which basically occur on the working flank of the teeth of the worm gear as a result of contact stresses σ_H (Fig. 2). The second group includes damage to the tooth root (overload breakage or fatigue breakage), which occur as a result of the bending stresses (τ_F) occurring there, which are

manifested on the working flank as tensile stresses, on the non-working flank as compressive stresses. Since worm gear wheel is one of the weakest elements of the worm gearing, these damages determine the service life of the entire gearing in the majority of applications.
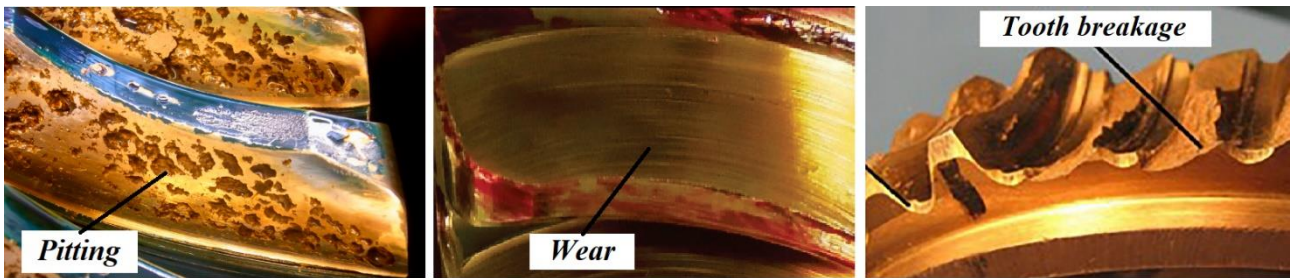
Fig. 1. Tooth damage to worm gear wheel [11, 12, 13]
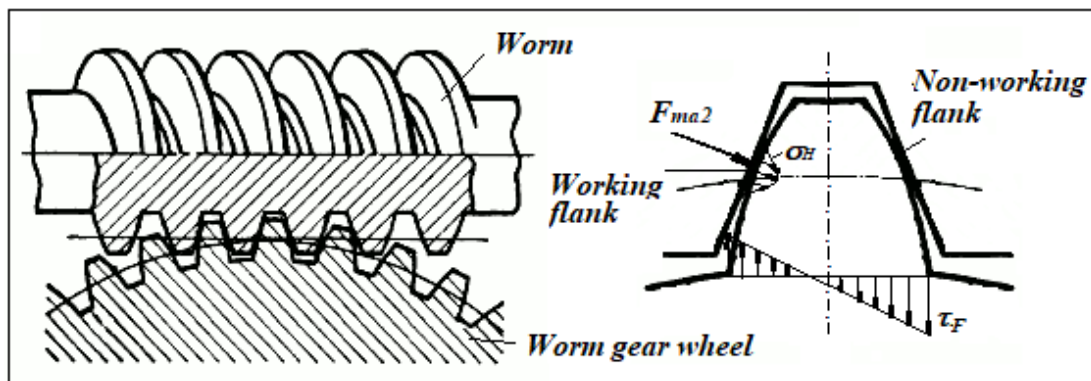
Fig 2. Operating stresses and types of worm gear teeth damage

If the worm gear wheel direction of rotation does not change during the entire operating time, the flank damage occurs only on the working flanks of the teeth. The non-working flanks are not loaded and remain without damage, regardless of the operating time. In [14], the question of increasing the service life of spur gearboxes by activating the non-working flank was considered. Due to the fact that worm gearboxes are characterized by increased sliding wear compared to spur gearboxes, an investigation is carried out in the present work on increasing the service life of worm gearboxes by changing the flank of the worm gear wheel teeth. The flank change of the teeth can be realized either by changing the direction of rotation or by inversion the worm gear wheel. Since tooth breakage can occur both on the tooth root of the working flank and the non-working flank, a comparative life assessment according to failure criteria tooth breakage and pitting (or wear) is required. An increase in service life by changing the tooth flank is only possible if the durability up to the occurrence of the tooth breakage is significantly greater than the service life up to the maximum (permissible) pitting (or wear).

It is known from practice that the main tooth damage of the worm gear wheel made of bronze, such as pitting, wear and tooth breakage, have mutual interactions [1]. When a critical pitting growth is reached, on the one hand, the abrasive sliding wear increases, on the other hand, increased wear can lead to a standstill in pitting development. Due to continuous wear, the pitting can even disappear again in many cases. Due to increased wear, the tooth thickness of the worm gear wheel is gradually reduced, as a result of which the probability of tooth breakage increases significantly. In [8], based on extensive studies, the service life of worm gear wheels was divided into three phases (Fig. 3). In phase I (pitting formation phase with load cycle number N_{LI}), only a small pitting value ($A_{P10} \leq 2\%$) and low mass removal (wear value Δm) are recorded. In the pitting growth phase II (load cycle number N_{LII}), the wear value increases insignificantly, although the pitting increases towards the end of this phase to the maximum value. In the wear phase III (load cycle number N_{LIII}), the pitting decreases and stagnates at a low value. But the wear value increases rapidly and leads to a significant

weakening of the tooth root. This phase usually ends with the total failure of the worm gear set due to tooth breakage or a disturbed torque transmission behavior.
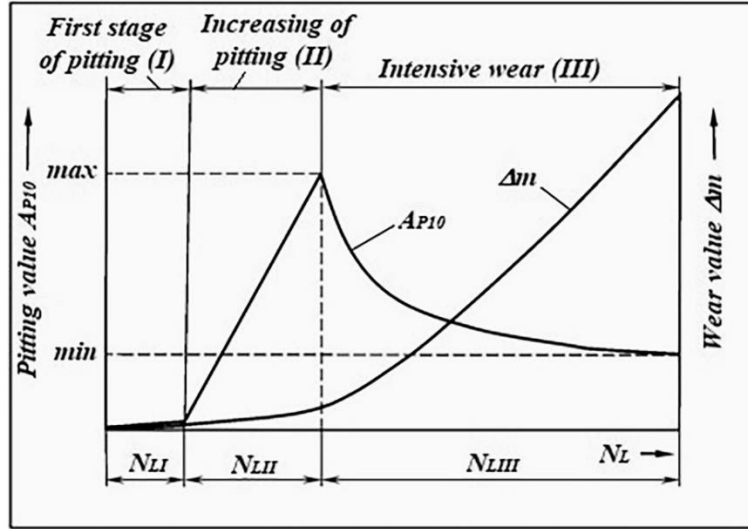
Fig. 3. The stages of failure on worm-gear wheel

Comparative analysis of service life. The activation of the non-working flank at the end of the pitting growth phase can lead to a significant increase in the service life, since at this point the wear value is still low and the teeth are little damaged. The stages of occurrence of failures in the teeth of a worm gearwheel are reflected in Fig. 4, a. As can be seen from the figure, damage to the tooth surface occurs, as a rule, in its working profiles. And non-working opposite profiles is practically not susceptible to damage after prolonged operation. Therefore, at the end of the second stage of operation, it is possible to increase the durability of the worm gear drive by replacing the working profiles with non-working ones. As can be seen from Fig. 4, b, with this method, the resource increase will be approximately in the amount of $N_{LI} + N_{LII}$.

To assess how much the worm gear resource can be increased by the above proposed method, it is of particular importance to conduct a comparative analysis of service life according to the criteria of pitting and wear, as well as according to the criteria of pitting and tooth breakage. Considering that the first two stages of the worm wheel service life are associated with pitting, the following empirical expression was proposed in [1] to determine the maximum limit of the total duration of these two stages:

$$N_{HL} = N_{LI} + N_{LII} = 3 \cdot 10^6 \cdot \frac{v_{gm}}{v_{ref}} \cdot \exp\left[24,924 - 4,047 \cdot \ln\left(520 \frac{\sigma_{Hm}}{\sigma_{Hlim}}\right)\right]. \qquad (1)$$

Where v_{gm} is sliding speed on the center circle in the flank direction; v_{ref} is sliding speed in the test sample (v_{ref}=3 m/s); σ_{Hm} medium contact stress on the flank of worm wheel teeth; σ_{Hlim} is the endurance limit.

Sliding speed on the center circle in the flank direction can be determined on the basis of [1] as follows:

$$v_m = \frac{d_{m1} \cdot n_1}{19098 \cdot \cos \gamma_m}$$

Where d_{m1} is the reference circle diameter of the worm; n_1 is speed of rotation on the worm shaft; γ_m is pitch angle at the center circle of the worm.

According to [3] the current calculated stresses σ_{Hm} can be determined as follows:

$$\sigma_{Hm} = \sqrt{\frac{2T_2 \cdot K_A}{a^3}} \cdot Z_E \cdot Z_0$$
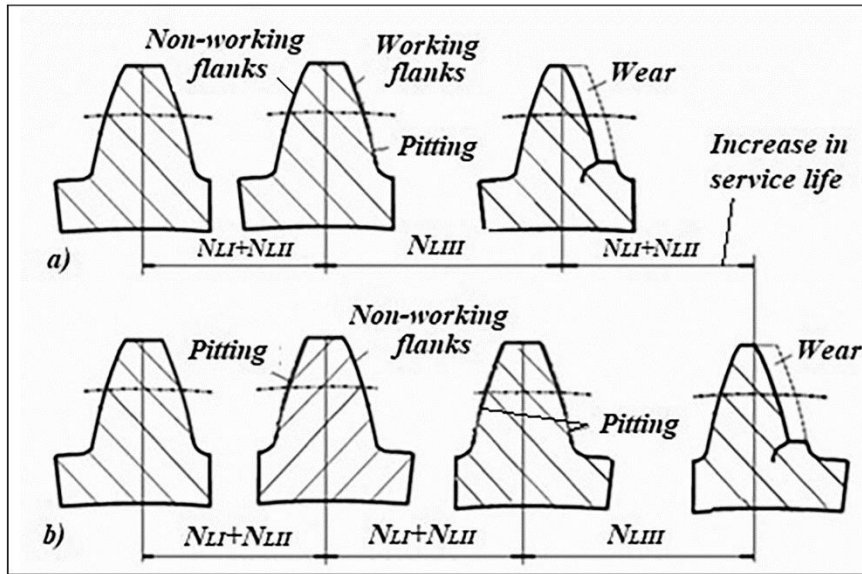
*Fig. 4. The stages of failure on worm-gear wheel without replacing (a)
and with replacing (b) of the working flanks of the teeth*

Where T_2 is the moment on the worm wheel; K_A is the application factor; Z_E is the elasticity factor; Z_0 is coefficient that takes into account the increase in the contact line in the worm gear; a is centre distance of worm gear.

As it was noted, the third and at the same time the last stage of service life of the worm wheel may end as a result of two different reasons. First, let's consider the first case when the worm wheel loses its operability as a result of exceeding the permissible wear limit of the teeth. To determine the resource of the worm wheel by the permissible wear of the teeth, in [6] the following expression was proposed:

$$N_{WL} = N_{LIII} = \frac{\delta_{WD} \cdot E_g}{J_W \cdot s_m^* \cdot \sigma_{Hm} \cdot a} \tag{2}$$

Where δ_{WD} is limit value of flank wear, mm; E_g is the modulus of elasticity in worm gear, N/mm^2; J_W is the wear intensity; s_m^* is the medium glide path, mm.

The limit value of flank wear at the normal cross-section of the worm wheel tooth is determined on the basis of various criteria depending on the field of application of the transmission and operating conditions. In most literature, this measure is taken equal to the thickness of the tooth head $\delta_{WD} = s_{a2}$ (Fig.5). Within the framework of this condition, the permissible wear limit for a normal cross-section of a worm wheel tooth can be determined by the following expression [1]:

$$\delta_{WD} = m \cdot \cos\gamma_m \left(\frac{\pi}{2} - 2tg\alpha_0 \right)$$

Where m is module, mm; α_0 is the gearing angle along the dividing circle of the worm wheel, in standard gears is assumed $a_0 = 20^0$.

The wear intensity of the working flanks of the worm wheel tooth can be determined by the following expression [1]:

$$J_W = J_{OT} \cdot W_{ML} \cdot W_{NS}$$

Where J_{OT} is basic value of wear intensity; W_{ML} is the material-lubricant factor; W_{NS} is the starting factor. (In long-term operation, $W_{NS} = 1,0$ is accepted).

The medium glide path on the tooth of the worm wheel s_m^* is determined depending on the shape of the worm profile and transmission parameters.

A comparative analysis of the predicted service life of the worm wheel according to the criteria of pitting and wear is of great practical importance. For the purpose of comparative analysis, a

47

dimensionless coefficient $K_{WH} = N_{WL}/N_{HL}$ was applied. At the end of the second stage of operation, i.e., at the moment when the pitting effect gets the maximum value, it is possible to increase the transmission life by the value $\Delta N_L = N_{LI} + N_{LII}$ by replacing the working flanks of the worm wheel teeth with non-working flanks (Fig. 4).
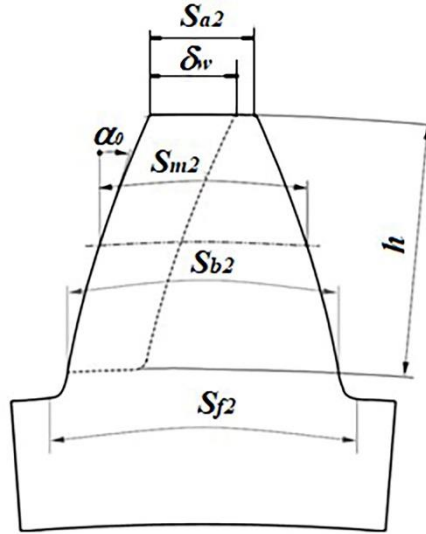
Fig. 5. Worm wheel tooth wear parameters

At this time, the following expression can be used to estimate the relative increase in service life:

$$\Delta L(\%) = \frac{N_{LI} + N_{LII}}{N_{LI} + N_{LII} + N_{LIII}} \cdot 100\% \qquad (3)$$

Using the equations (1) and (2) in (3), calculations were performed on various values of the gear ratio (u) and the number of cycles (n_1) of the worm gear with an center distance a=160 mm, the torque on the shaft of the worm wheel T_2= 4900 Nm. The material of the worm was adopted hardened steel grade 16MnCr5 (surface hardness 58÷62 HRC), and the material of the worm wheel CuSn12Ni2-C-GZ (σ_{Hlim}=520 N/mm^2), obtained as a result of casting by centrifugal method.

The values of other parameters required for calculations are set according to the [1]. The results of the calculations are shown in Fig. 6. As can be seen from the figure, as the number of worm shaft cycles increases, the values of the relative increase in service life time also increases. This is due to the fact that at low worm speeds, the stages of formation and intensive pitting increase (N_{LI} and N_{LII}) are short, and the process of intensive wear (N_{LIII}) begins quickly. Calculations show that by replacing the working profiles of the wheel teeth with non-working profiles, when the rotation speed of the worm shaft n_1=3000 min^{-1}, it becomes possible to increase the transmission life by 40÷55%. Obviously, the gear ratio also has a significant impact on the relative increase in service life. With a large gear ratio, the possibility of increasing the resource becomes greater. At u=20.5, it is possible to increase the resource by 25-45% depending on the rotation speed, and at u=50 - by 30-55%.

One of the main conditions that with the proposed method it is possible to increase the life of the worm gear is the absence of the possibility of tooth breakage under the influence of bending stresses. Intensive wear of the working surface of the tooth at the third stage can lead to a decrease in its thickness and, consequently, breakage as a result of loss of bending strength. For this reason, a comparative analysis of service life according to the criteria of bending and contact stresses of the worm wheel tooth is of particular importance.

To determine the predicted service life by the criterion of bending stress, it is necessary to calculate these stresses. Based on [1], the bending stresses arising in the tooth of the worm wheel can be determined by the following expression:

$$\tau_F = \frac{F_{t2}}{b_2 \cdot m} \cdot Y_\varepsilon \cdot Y_F \cdot Y_\gamma \cdot Y_k . \qquad (4)$$
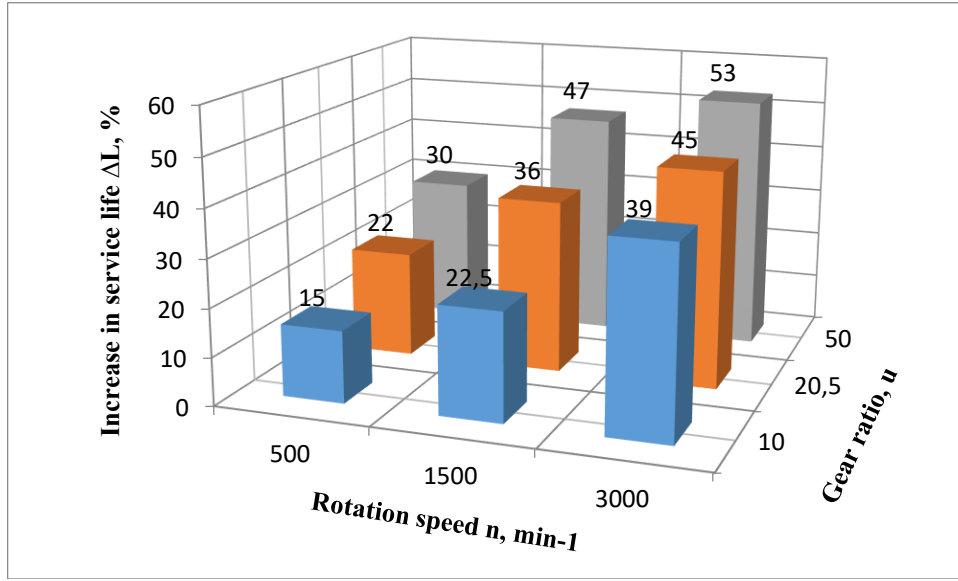
Fig. 6. The relative increase in service life time for worm gear with a=160 mm and T₂= 4900 Nm

Where F_{t2} is tangential force on the worm gear wheel; b_2 is width of worm gear wheel; Y_ε is the contact ratio factor for tooth root stress; Y_γ is the Helix angle factor for tooth root stress; Y_k is wheel rim thickness factor.

As can be seen from equation (4), the bending stress gradually increases from τ_{F1} to τ_{F2} depending on the wear of the tooth (Fig. 7). Where τ_{F1} is the bending stress, in the absence of wear ($\Delta S=0$). Since the wear of the tooth at the first and second stages of operation is insignificant, we can assume that the value of the bending stress at these stages is equal to τ_{F1}. At the third stage of operation (the stage of intensive wear), the bending stress can gradually increase to a value of τ_{F2}, causing tooth breakage (if the wear values before tooth breakage do not exceed the permissible limit). Therefore, to simplify the calculations, we assume that the value of the bending stress at the last stage is equal to τ_{F2}. At the same time, it is also ensured that a certain margin of safety is obtained for bending stress.

In the case when the third stage of operation end due to the breakage of the worm wheel tooth under the influence of bending stresses τ_{F2}, the length of this stage can be approximately determined by the following equations:

$$\dot{\text{I}}f \ \tau_{F2} \geq \tau_{F\lim}, \text{ then } N_{LIII} = N_{FD} \cdot \left(\frac{\tau_{F2}}{\tau_{F\lim}}\right)^k \tag{5}$$

$$\text{if } \tau_{F2} < \tau_{F\lim}, \text{ then } N_{LIII} = N_{FD} \cdot \left(\frac{\tau_{F2}}{\tau_{F\lim}}\right)^{-(2k-1)} \tag{6}$$

Where $\tau_{F\lim}$ is the endurance limit; N_{FD} is the number of cycles, corresponding to fracture of fatigue curve; k is the fatigue curve indicator. For worm wheels made of bronze, k=6 is accepted [6].

The Mayer-Haibach hypothesis [15] was used in equation (6) above when $\tau_{F2}<\tau_{F\lim}$.

Thus, taking into account the recommendations in [16], depending on the values of the bending stress acting at all stages of operation τ_{F1} and τ_{F2}, it is possible to determine on the basis of graph in Fig. 7 the predicted service life of the worm wheel, as follows:

$$\text{if } \tau_{F1} \geq \tau_{F\lim} \text{ and } \tau_{F2} \geq \tau_{F\lim}, \text{ then } N_{FL} = N_{FD} \cdot \tau_{F\lim}^k \frac{N_{LI} + N_{LII} + N_{LIII}}{\tau_{F1}^k \left(N_{LI} + N_{LII}\right) + \tau_{F2}^k N_{LIII}}, \tag{7}$$

$$\text{if } \tau_{F1} < \tau_{F\lim} \text{ and } \tau_{F2} < \tau_{F\lim}, \text{ then } N_{FL} = N_{FD} \cdot \tau_{F\lim}^{2k-1} \frac{N_{LI} + N_{LII} + N_{LIII}}{\tau_{F1}^{2k-1} \left(N_{LI} + N_{LII}\right) + \tau_{F2}^{2k-1} N_{LIII}}. \tag{8}$$

In the latter equations, the value of the $N_{LI}+N_{LII}$ should be determined by the formula (1), and the values of the N_{LIII} should be determined by the formulas (5) and (6).
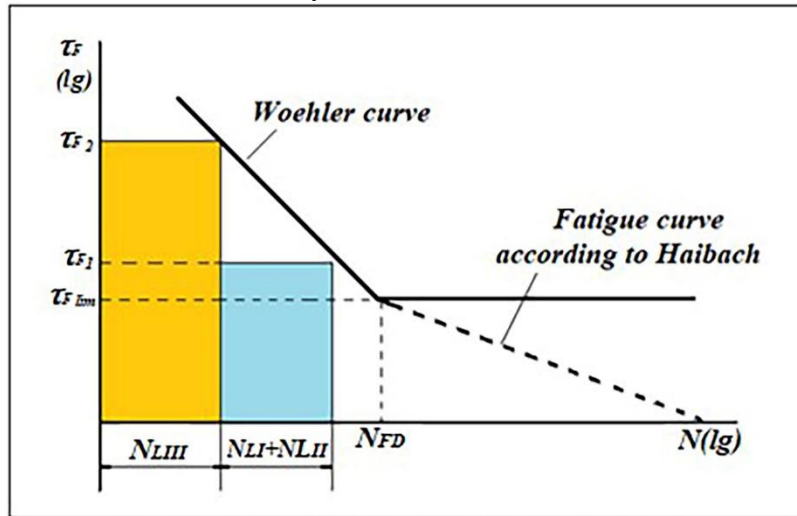
Fig. 7 Bending stress fatigue curves for worm wheel

To increase the service life by replacing the working flanks of the worm wheel teeth with non-working flanks after a certain period of operation, the estimated resource of the teeth according to the bending criterion should be sufficiently large than the predicted resource according to other criteria. Therefore, a comparative analysis of the worm wheel service life by the criterion of bending and contact stresses, as well as by the criterion of bending and wear is of particular importance. Let's consider a comparative analysis of tooth resources by strength conditions by bending stress and by contact stresses. To this end, it becomes necessary to study the dependence of the dimensionless parameter $K_{FH}=N_{FL}/N_{HL}$ on various factors.
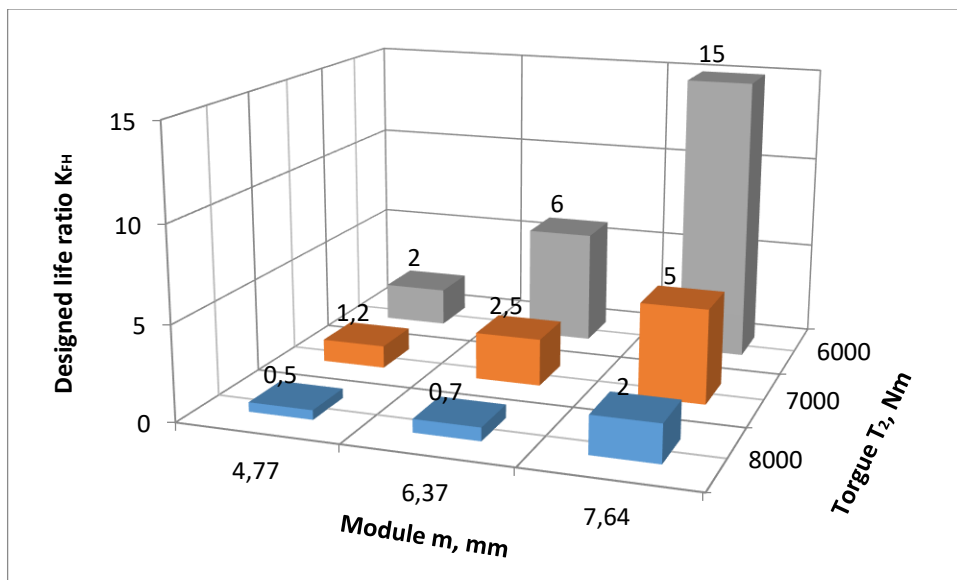
Fig. 8. Service life ratio K_{FH} for worm gear wheel made of CuSn12-Ni2-C-GZ for different modules

For a worm gear with an axial distance $a_w=160$ mm, a gear ratio u=20.5, the values of the K_{FH} parameter are set for various values of the torque (T_2), module (m) and the number of cycles (n_1) of the worm shaft. The material of the worm was adopted hardened steel grade 16MnCr5 (surface hardness 58÷62 HRC), and the material of the worm wheel CuSn12Ni2-C-GZ ($\sigma_{Hlim}=520$ N/mm^2, $\tau_{Flim}=100$ N/mm^2, $N_{FD}=5\cdot10^6$), obtained as a result of casting by centrifugal method. The calculation

results are shown in Fig. 8 and 9. As can be seen from the graphs, with an increase in the load on the worm wheel, the value of the service life ratio decreases. But at nominal load limits, the value of this parameter is greater than 2 with a module m=4,77 mm. At large values of the module (m=6,37 mm and m=7,64 mm), the K_{FH} parameter becomes quite high. And at values of the modulus m<4,77 mm, bending stresses become quite dangerous and the probability of tooth breakage from the effects of these stresses becomes higher. The rotation speed of the worm shaft (n_1) also has a fairly large effect on the service life ratio K_{FH}. Under heavy loads, the K_{FH} parameter decreases when n_1 increases.
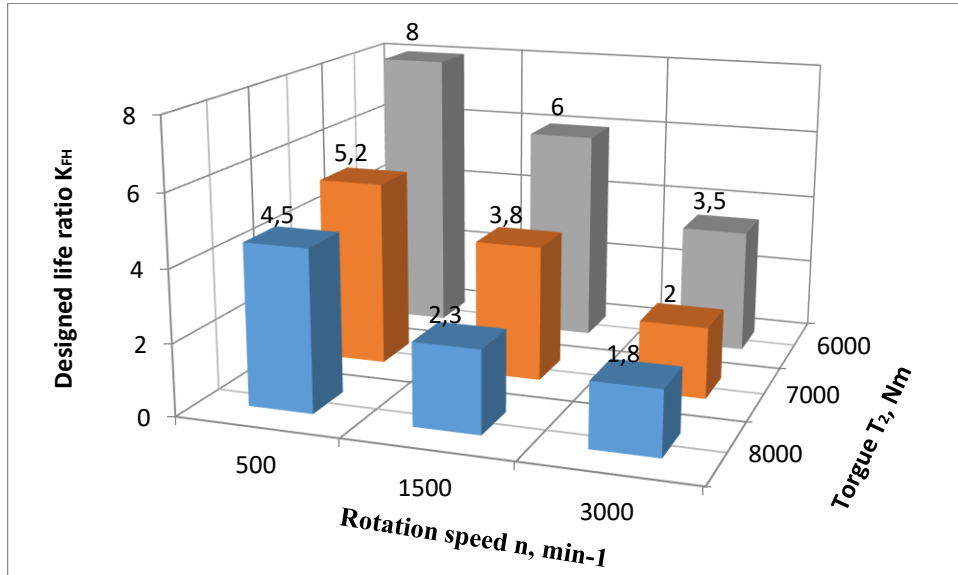
Fig. 9. Service life ratio K_{FH} for worm gear wheel made
of CuSn12-Ni2-C-GZ for different drive speeds

In [8] reflects the results of a large number of experimental tests conducted at different values of the output shaft torque (T_2) and the rotation speed of the worm shaft (n_1) at different values of geometric and kinematic parameters (Table 1). The tests were carried out on a specially designed testing facility in the laboratory of the Institute "Machine Elements" of the Technical University of Munich. These experiments were carried out on worm gears consisting of a cylindrical worm with an involute profile made of steel grade 16MnCr5 and a worm wheel made of bronze grade CuSn12Ni-GZ, obtained by centrifugal casting. The analysis of the obtained results shown that in the worm gear tested, the value of the coefficient K_{FH} is greater than 1.

Table 1. The main parameters and indexes of service life of the tested worm gears

Basic transmission parameters	Rotation speed of the worm shaft n_1, min^{-1}	Output shaft torque T_2, Nm	Amount of wear Δm, q	Service life, 10^6 number of cycles		Service life ratio, K_{WH} (K_{FH})
				N_{HL}	N_{WL} (N_{FL})	
a=65 mm; u=20,5; m=2,5 mm	1470	210	12,36	13,96	27	1,94
	1470	290	47,9	1,99	26,46	13,3
a=100 mm; u=10,3; m=5 mm	500	1180	71,5	0,58	7,3	12,6
	500	1696	124,4	0,29	0,85	2,93
	1500	750	95,5	6,7	42,4	6,33
	1500	750	88,4	4,96	40,68	8,2
	1500	1180	108,8	2,94	10,71	3,64
	1500	1180	118	2,13	12,81	6
	1500	1180	83,98	2,51	6,49	2,6
	1500	1180	159	2,24	12,41	5,54

	1500	1696	88,6	1,31	3,05	2,33
	1500	1696	105,5	1,31	2,61	2
	2800	1180	174,9	5,26	22,26	4,23
	2900	1180	124,7	5,95	13,82	2,32
a=100 mm; u=20,5; m=4 mm	1500	700	81,7	6,06	19,48	3,21
	1500	700	140,2	2,73	13,04	4,77
	1500	700	89,7	5,27	17,93	3,4
a=160 mm; u=20; m=6,25 mm	2900	1470	396,3	2,51	12,54	5
	2900	1470	121	6,64	12,6	1,9

In general, the change in the tooth flanks of the worm gear wheel can be realized with the following procedures:

1.   Change in direction of rotation of the electric motor. This very simple method can only be used in the same cases if the direction of rotation of the motor does not affect the operation of the machine.

2.   Inversion of the gear wheels. This process can only be realized for worm gear wheels in general mechanical engineering, if the wheels are not made with shaft from one piece. In this procedure, the necessary maintenance work (disassembly, inversion and installation of the gearwheels) is to be implemented, and the direction of rotation of the electric motor is not required.

Conclusions. Based on the research conducted, the following conclusions can be made:

1. The service life ratio of worm gear wheels according to the criteria of bending and contact stresses depends on the geometric and kinematic parameters of transmission, mechanical characteristics of materials. Increasing the module and wheel width allows you to increase the service life ratio;

2. Replacing the working profiles of the teeth with non-working ones after a certain period of operation, ensuring the necessary strength for bending stresses by the correct choice of geometric parameters and materials, increases the lifetime of the worm wheel gears;

3. It has been proved by calculations that due to this procedure, the service life of the worm gear can be increased up to 60%. For this, the flank change must be realized at the end of the pitting growth phase.

REFERENCES

[1]. DIN 3996: *Tragfähigkeitsberechnung von Zylinder-Schneckengetrieben mit sich rechtswinkling kreuzenden Achsen.* Beuth-Verlag, 2012, Berlin, Köln. (in German)

[2]. Khurmi, R.S., Gupta, J.K. *Machine Design*, Eurasia Publishing House, 2005, Ram Nagar, New Delhi.

[3]. Decker, K. *Maschinenelemente: Funktion, Gestaltung und Berechnung*. 2018, Carl Hanser Verlag, München, Wien. (in German)

[4]. Monz, A. *Tragfähigkeit und Wirkungsgrad von Schneckengetrieben bei Schmierung mit konsistenten Getriebefetten.* (Load capacity and efficiency factor of worm gears lubricated with consistent gear greases), 2012, Ph.D. thesis TU Munich. (in German)

[5]. Kishore, K., Mukhopadhyay, G., Adhikary, M. *Metallurgical Analysis of Premature Failure of a Phosphor Bronze Worm Wheel*. J. Fail. Anal. Prev. 2018, 18, pp. 1321–1326. https://doi.org/10.1007/s11668-018-0554-x

[6]. Thiele, R. *Untersuchungen zur Zahnfußbeanspruchung von Schneckenrädern und Entwicklung eines Tragfähigkeitsnachweises auf Basis der Zahnfußschädigungshypothese*. (Investigations on the tooth

root stress of worm gears and development of a load-bearing capacity verification based on the tooth root damage hypothesis). 2006, Ph.D. thesis TU Chemnitz:. (in German)

[7]. Reißmann, J., Leidich, E. *Calculation of the tooth root strenght of worm wheels on local stresses. Garching: International conference on gears*, VDI-Berichte, 2013. ISBN: 978-3-18-092119-0

[8]. Rank, B. *Versuche zur Grübchentragfähigkeit von Schneckengetrieben: Untersuchungen an Zylinder-Schneckengetrieben* - Grübchenbildung, Verschleiß. – München: TU München. FVA-Forschungsvorhaben 12/IV. Heft 494, 1996. (in German)

[9]. Heilemann, J. *Tragfähigkeit und Wirkungsgrad bei unterschiedlichen Schnecken-Zahnflankenformen unter Berücksichtigung der Oberflächenhärte und Härtetiefe* (Bearing capacity and efficiency for different worm tooth flank shapes, taking into account the surface hardness and hardness depth), 2005, Ph.D. thesis TU Munich. (in German)

[10]. Weisel, C. *Schneckengetriebe mit lokal begrenztem Tragbild* (Worm gearboxes with locally limited tooth bearing), 2009, Ph.D. thesis TU Munich. (in German)

[11]. Sigmund, W. *Untersuchung und Simulation des Verschleißverhaltens von Schneckengetrieben mit unvollständigem Tragbild* (Investigation and simulation of the wear behavior of worm gears with incomplete tooth bearing). 2015, Ph.D. thesis TU Munich. (in German)

[12]. Mautner, E.M., Stemplinger, J.P., Stahl, K.: FVA-Nr. 503 II - Heft 1162 - *Schnecken-getriebe-Baugrößeneinfluss II Abschlussbericht - Verschleiß- und Grübchentragfähigkeit von großen Zylinder-Schneckengetrieben mit optimierter Radbronze*. 2015, Forschungsvereinigung Antriebstechnik e.V., Frankfurt/Main.

[13]. Tschalabi, I. *Lebensdauererhöhung von Schneckengetrieben durch Flankenwechsel der Radzähne* / I. Tshalabi, E. Leidich, J. Reißmann //ANT Journal. 2012, Nr. 12, pp. 14-17.

[14]. Chalabi, I. *Comparative Service Life Analysis for Gears According to Different Failure Criteria.* J. Fail. Anal. Prev. 2020, 20. pp. 2137-2144. https://doi.org/10.1007/s11668-020-01029-y

[15]. Haibach, E. *Betriebsfestigkeit-Verfahren und Daten zur Bauteilrechnung*, 2006, VDI-Verlag GmbH, Dues seldorf.. (in German)

[16]. Naunheimer, H., Bertsche, B., Ryborz, J., Novak, W. *Automative Transmissions: Fundamentals, Selection, Design and Application*, 2011, Springer-Verlag, Berlin Heidelberg.

A CONSTANT VOLUMETRIC-FAILURE-STRAIN EROSION FOR DETERMINING THE EFFECT OF INERTIA AND STRAIN RATE ON THE CRUSHING STRENGTH OF A CELLULAR CONCRETE

Burak AKYOL[1], Mustafa GÜDEN[2*]

[1,2]Dynamic Testing and Modeling Laboratory and Department of Mechanical Engineering, Izmir Institute of Technology, Izmir, Turkey

E-mail:bakyol@iyte.edu.tr[1], mustafaguden@iyte.edu.tr[2]*

Abstract: The effect of inertia and strain rate on the failure of a cellular autoclaved aerated concrete (600 kg m^{-3}) was investigated using MAT_096 material model together with a constant volumetric-failure-strain erosion criterion in the LSDYNA. A rate insensitive, constant compressive yield stress, and a rate sensitive, variable compressive yield stress, model were implemented and the results of models were compared with those of experimental compression tests conducted at similar strain rates, between 2x10^{-3} s^{-1} and ~4150 s^{-1}. Results have shown an "s-type" compressive strength relation with strain rate, broadly composing of three distinct regions: a lower-velocity-dependent-strength region at the quasi-static velocities, a higher-velocity-dependent-strength region at intermediate velocities and again a lower-velocity-dependent-strength region above ~1150 s^{-1}. In experimentally tested samples, a shock fracture strength was presumed to be reached in the higher velocity-dependent strength region, resulting in a cut-off DIF value (2.78), while in numerically tested samples, the compressive strength increased with increasing strain rate in the third region. One dimensional state of strain condition above a critical velocity was also shown numerically. The stress triaxiality increased to 0.66 between 1 and 30 m s^{-1}, reaching a fully constraint 1D state of strain condition above 30 m s^{-1}. In accord with this, the numerical failure mode, as with that of experiments, switched from an axial- to a radial-dominated cracking after ~20 m s^{-1}. Finally, the strain rate dependent compressive strength was numerically shown as partly arising due to the change of deformation state from a 1D state of stress to a 1D state of strain and partly due to the intrinsic rate sensitivity of cellular concrete.

Keywords: Autoclaved aerated concrete, modelling, compressive strength, inertia, strain rate

Introduction. There have been numerous experimental and numerical investigations on the strain rate dependent compressive strength of concrete. A summary on the strain rate dependent compressive strength of concrete can be found in a recent review article [1]. Briefly, the dynamic increase factor (DIF=dynamic facture strength/static fracture strength) of concrete varies between 1 and 2.5, from static to dynamic strain rates, with a sudden increase after about 100 s^{-1} [1]. A relatively low dependence of DIF on strain rate until about 100 s^{-1} was ascribed to both the strain-rate dependent growth of tensile micro cracks, known as thermally activated facture mechanism, and the viscous behavior of the bulk material between cracks known as Stefan effect [2-4]. The thermally activated facture mechanism is explained as follows. The energy needed for crack opening is much higher than the energy needed for crack growth at quasi-static strain rates. While, there is less time at high strain rates for both crack opening and growth, causing an increase in fracture strength and the number of micro cracks formed as compared with quasi-static strain rates. It was argued that inertial effects become predominant at the strain rates higher than 10 s^{-1} [5]. At increasing strain rates, an elastically deforming structure cannot expand in transverse direction (Poisson's expansion) due to radial inertia restraint. Radial inertia imposes a confinement pressure on deforming structure, transforming the deformation from a uniaxial state of stress to a uniaxial state of strain. The rapid increase of the strength of concrete after about a critical strain rate is therefore ascribed to the development of a

uniaxial state of strain [6-10]. The variations in the DIF values of different studies performed at similar strain rates were further attributed to the variations in the extent of radial and axial inertia between the concrete samples tested [11, 12]. The reported data on the compressive strength of concrete included the forces due to both axial and radial inertia.

An "s-type" dependence of the fracture strength of brittle materials on strain rate was reported [13]. On an "s-type" curve, there are two turning points: (1) from a low-strain rate-dependent strength region to a high-strain rate-dependent strength region and (2) from a high-strain rate-dependent strength region to again a low-strain rate-dependent strength region. The strength of limestone increased slowly with increasing strain rate up to 10^3 s^{-1}; thereafter, increased sharply, approaching the shock fracture strength [6]. The strain rate dependent fracture strength well above 10^3 s^{-1} was proposed to resemble the strain dependent fracture strength below 10^3 s^{-1}, while the rapid increase of fracture strength around 10^3 s^{-1} was ascribed to the transformation of deformation from a uniaxial state of stress to a uniaxial state of strain. The first and second turning points were reported sequentially 10^2 and 10^4 s^{-1} for concrete [14]. Also, in accord with above, the current concrete models have recently adapted a cut-off value of 2.94 to cap DIF above 300 s^{-1} [15]. But, it is not clear whether or not this capping occurs in or after the high-strain rate-dependent strength region. Alternatively, it is proposed that the capping may occur because concrete reaches its ultimate dynamic strength before the second turning point in the high-strain rate-dependent strength region [4].

The aim of this study was to experimentally and numerically investigate the strain rate sensitive compressive strength of an aerated autoclaved concrete (AAC) using a constant volumetric-failure-strain erosion criterion in the MAT_096 material model of the LSDYNA. Once an element reached a critical volumetric-failure-strain corresponding to that of quasi-static strain rate it was eroded. The used erosion criterion and the associated material model were relatively simple, requiring few experimental input parameter and noted to predict the trends of experimental stress-strain curves with strain rate. The model results were further verified with the compression test results between quasi-static ($2x10^{-3}$ s^{-1}) and dynamic (~4150 s^{-1}) strain rates. Modified Split Hopkinson Pressure Bar (SHPB) tests, so called the direct impact tests, were performed to achieve strain rates above 1000 s^{-1}. Two different modelling approach called Model 1 and Model 2 were investigated. In the first, a strain rate independent material model was implemented to determine the effect of axial and radial inertia on the fracture strength merely. In the second, a strain rate dependent compressive strength was used as an input to the material model to show the effect of strain rate. Since the investigated upper dynamic strain rates were higher than those of the second turning point of concrete on an "s-type" curve, the model and experimental results allowed the analysis of the strain rate dependent-fracture strength at above these critical strain rates using both approach. Finally, as there has been, so far, no numerical studies on the strain rate dependent compressive strength of these materials and few experimental investigation on the dynamic response [16-19], the results of present study are expected to contribute to the knowledge on modelling dynamic mechanical response of such brittle cellular materials.

Tests and models.

Tests

Quasi-static and dynamic compression test samples were ~19.4 mm in diameter and 26 mm in length. The test samples' diameter was determined by the bar diameter of the used SHPB. Quasi-static compression tests were performed in a Shimadzu AG-X Universal Test machine at $5x10^{-5}$, $5x10^{-4}$, and $5x10^{-3}$ m s^{-1}, corresponding to strain rates of ~$2x10^{-3}$, ~$2x10^{-2}$ and ~$2x10^{-1}$ s^{-1}, respectively. Low-velocity compression tests were performed in a FRACTOVIS drop-weight test device using a flat-ended striker at about 1 m s^{-1}, corresponding to a strain rate of ~35 s^{-1}. The dynamic compression tests were performed in a SHPB apparatus, having 19.4 mm-diameter Inconel 718 incident (3110 mm) and transmitter (2050 mm) bars. Conventional SHPB compression tests were performed at 8 m s^{-1} corresponding to ~185 s^{-1}. In the direct impact tests, the striker bar (Inconel bar 500 mm-long and

aluminum bar 200 mm-long) directly impinged on the test sample inserted to the end of the SHPB incident bar. The direct impact SHPB tests were performed at 10, 30 and 108 m s^{-1} corresponding to ~385, ~1150 and ~4150 s^{-1}, respectively. At least 8 samples were tested at each strain rate. The details of the direct impact tests and the used SHPB test device are given elsewhere [20-22]. The tensile strength of AAC sample was determined by the indirect tensile Brazilian tests. In these tests, the cylindrical compression test samples (3 tests), 19.4 mm in diameter and 26 mm in length, were compressed laterally in a Shimadzu AG-X Universal Test Machine. The tensile strength (σ_t) was then calculated as

$$\sigma_t(t) = \frac{2P}{\pi DL} \tag{1}$$

where *P*, *D* and *L* are sequentially the fracture load and the diameter and thickness of sample.

Models

The quasi-static and high strain rate compression and direct impact tests were simulated in the non-linear explicit finite element code of LS-DYNA. The quasi-static model was briefly composed of top and bottom compression test platen (tool steel) and sample as seen in Figure 1(a). Each compression platen was modelled using 6 mm-long and 2 mm–wide 19200 solid elements and MAT020_RIGID material model (E=210 GPa and ν=0.3). The rotations and the translations of compression test platens were restricted in all directions, except the axial translation of the top platen in z-direction was kept constant by PRESCRIBED_MOTION_RIGID card at 5x10^{-3} m s^{-1}, the same as the quasi-static tests. The contacts between compression test platens and sample were defined by AUTOMATIC_SURFACE_TO_SURFACE. The mass scaling was implemented in the quasi-static simulation by using CONTROL_TIMESTEP card. The model was initially simulated without mass scaling in order to determine time-step. The determined time-step was then multiplied by a factor until kinetic energy became much smaller than internal energy. A mass scaling factor of 1000 was determined by following above procedure. In the SHPB test model, the striker, incident and transmitter bars were modelled using 15x2 mm 7000, 28980 and 19180 solid elements, respectively (Figure 1(b)). The striker bar velocities in the SHPB model were 1 and 8 m s^{-1}. The drop-weight test at ~1 m s^{-1} was also modelled with the SHPB compression test model. The lengths of Inconel 718 striker, incident and transmitter bar were sequentially 500 mm, 3110 mm and 2050 mm, the same as the used SHPB. The contacts between the bars and sample and between the striker and incident bar were defined by AUTOMATIC_SURFACE_TO_SURFACE and AUTOMATIC_SINGLE_ SURFACE, respecttively. The impact velocities in the SHPB direct impact simulations were 10, 20, 30, 60 and 108 m s^{-1}. The models at 10 and 20 m s^{-1} were implemented with 500 mm-long Inconel 718 striker bar, while the tests at 30, 60 and 108 m s^{-1} were implemented using 200 mm-long aluminum striker bar, the same as the tests. The incident and striker bars in these tests were again modeled using 15x2 mm solid elements, whereas aluminum striker bar was modelled using 5x2 mm 10080 solid elements (Figure 1(c)). The contact between the sample and incident bar was defined by AUTOMATIC_SURFACE_TO_SURFACE and the contact between the striker and incident bar was defined by AUTOMATIC_SINGLE_SURFACE. The velocity of striker bar was defined by the VELOCITY_GENERATION card in LS-DYNA. Inconel 718 striker, incident and transmitter bar and aluminum striker bar were simulated using MAT001_ELASTIC material model (Inconel 718: E=207 GPa, ν=0.33 and ρ=7850 kg m^{-3} and aluminum: E=71.7 GPa, ν=0.33 and ρ=2810 kg m^{-3}). The static and dynamic friction coefficients were taken 0.2 and 0.1 for lubricated surfaces and 0.3 and 0.2 for non-lubricated surfaces, respectively.

The cylindrical AAC sample was modelled using 38400 solid elements and MAT096_BRITTLE_DAMAGE material model. The used material model was also previously applied to simulate the failure of concrete [23]. The material model allowed to admit progressive degradation of tensile and shear strengths across smeared cracks initiated under tensile loads [24]. The compressive failure was governed by a simplistic J2 flow correction [25]. The damage occurred was handled by treating 4-rank elastic stiffness tensor as an evolving internal variable. The main material model parameters are the Elastic modulus, Poisson's ratio, the initial principal tensile strength (f_n), the initial shear traction (f_s), the fracture toughness of the material (g_c), shear retention factor (β), the viscosity of the material (η) and uniaxial compressive yield stress (σ_y) [26]. ERODING_SINGLE_SURFACE was applied to AAC sample by MAT000_ADD_EROSION parameter in both SHPB and direct impact test models. The volumetric-failure-strain (corresponding to compressive strength) at a quasi-static strain rate (0.0117) was used as the erosion parameter in MAT_ADD_EROSION. The volumetric strain (Δ) is

$$\Delta = \varepsilon_x + \varepsilon_y + \varepsilon_z \qquad (2)$$

where ε_x, ε_y and ε_z are the normal strains in x, y and z-axis. The model stresses were determined at the distal-end and impact-end contact areas, at the center and surface elements at the contact areas and on the incident bar at the strain gage location of the test (Figure 1(d)). The determined material parameters of AAC are tabulated in Table 1.
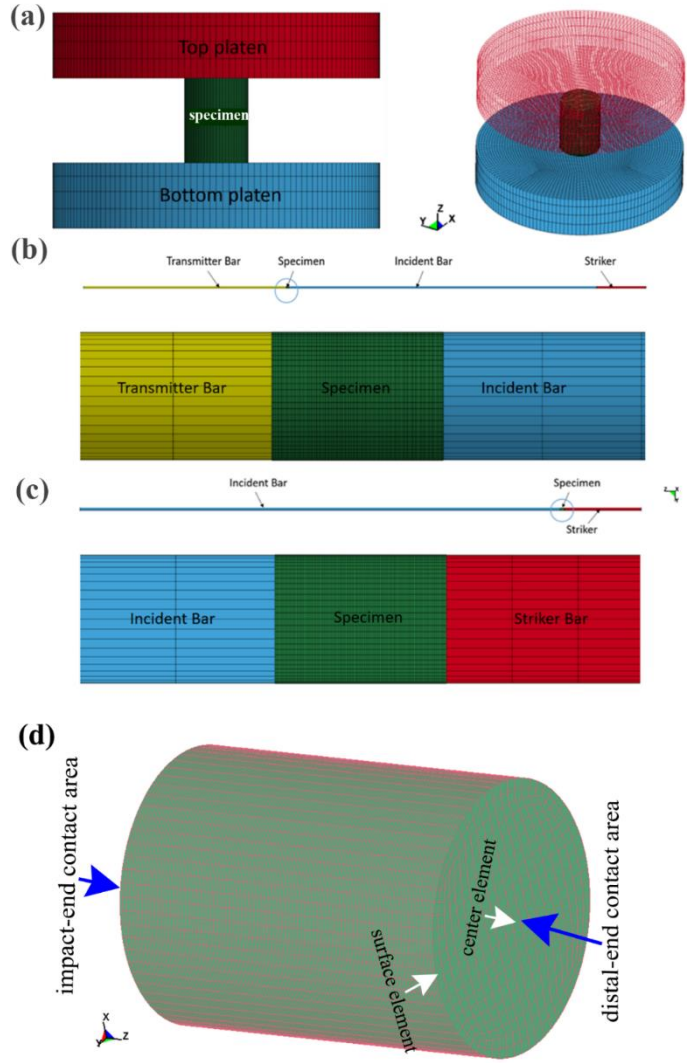
Fig. 1. 2D and 3D models of (a) quasi-static compression, (b) SHPB compression, (c) SHPB direct impact tests and (d) sample with the location of numerical stress measurement

Table 1. Material model parameters of AAC

Parameter	Value
Density, ρ (kg m^{-3})	600
Young's Modulus, E_B (GPa)	0.32
Poisson's Ratio, v	0.2
Tensile Limit (MPa)	1
Shear Limit (MPa)	2.56
Compressive yield stress (MPa)	5.11
Fracture Toughness (N m^{-1})	3.47
Shear retention factor	0.03

A shear retention factor of 0.03, typical for concrete, was taken from reference [23] and all other material parameters were extracted for the tests at a quasi-static strain rate of 0.002 s^{-1}. The viscosity was taken zero in order to exclude the effect of strain rate in Model 1, while the compression yield stress corresponding to each velocity were entered in the material model for the strain rate sensitive model, Model 2.

Results and Discussion.

Quasi-static and high strain rate tests

Three representative stress-strain curves of quasi-static compression tests at 5x10^{-5} and 5x10^{-3} m s^{-1}, drop-weight compression tests at 1 m s^{-1} and SHPB direct impact tests at 8 m s^{-1} are shown in Figure 2(a). Note that in the SHPB direct impact tests, the stress was measured from a strain gage 1 m away the sample/incident bar contact area. The equilibrium in SHPB test was further checked by using the following relation [27]: $3t_{tr} = \varepsilon_f l/v$; where t_{tr} and ε_f are the transit time ($l/\sqrt{E/\rho}$) and facture strain of the sample and v, l, E and ρ are the impact velocity and the length, elastic modulus and density of sample, respectively. Using ε_f=0.012, l=26 mm, ρ=600 kg m^{-3} and E=0.7 GPa (Figure 2(a)), one can arrive a critical velocity of ~5 m s^{-1} (t_{tr}=22 μs) above which there will be no stress equilibrium in the SHPB test. In the SHPB compression tests at 8 m s^{-1}, an aluminum disc of 1 mm thick and 10 mm in diameter was used as a pulse shaper [9] in the front of the incident bar to attain stress equilibrium. In these tests, the failure time (100 μs) was more than 4 times the wave transit time, showing nearly a stress equilibrium condition and corresponding to a strain rate of 185 s^{-1} at failure strain (Figure 2(b)). While, the tests at 10 m s^{-1} as seen in Figure 2(b) ($\varepsilon_f l/v$=45 μs) and above are non-equilibrium tests. In these tests, the deformation is represented by $\frac{v}{l}t$ instead of strain. Figure 2(c) shows representative equilibrium stress-$\frac{v}{l}t$ curves at 5x10^{-5} and 1 m s^{-1} and representative non-equilibrium stress-strain curves at 10, 30 and 108 m s^{-1}. Non-equilibrium stress-$\frac{v}{l}t$ curves in the same figure are shown for the comparison between compressive stresses. The maximum stresses in the stress-strain curves of Figures 2(a) and in the stress-$\frac{v}{l}t$ curves of Figure 2(c) are taken as the compressive strengths. As noted in the same figures, the compressive strength increases as the velocity increases between 5x10^{-5} to 30 m s^{-1}, while, the compressive strengths at 30 and 108 m s^{-1} are very much similar. The elastic modulus was determined from the initial slopes of the curves, from 5x10^{-5} to 8 m s^{-1}. The elastic modulus increases from ~0.32 GPa at quasi-static velocity to ~0.7 GPa at 8 m s^{-1} (Figure 2(a)). The slopes of stress-$\frac{v}{l}t$ curves of the tests at 30 and 108 m s^{-1} are comparatively lower as these are non-equilibrium tests. The variation of compressive failure strain (corresponding to the compressive strength) with velocity until about 8 m s^{-1} (SHPB compression equilibrium test) is shown in Figure 2(d). The compressive failure strain starts to decrease at 8 m s^{-1} and an average compressive failure strain of 0.017 is taken for the quasi-static tests. Assuming the SHPB test at 8 m s^{-1} is confined state (no lateral expansion of sample), the volumetric fracture strain are calculated for the tests below this velocity. As shown in Figure 2(d), the average volumetric facture strain is about 0.0117 and this value was used in the modelling. Three tensile stress-displacement curves of the Brazilian tests are shown in Figure 2(e), together with the picture of an undeformed and a deformed, centrally-fractured test sample. The mean tensile strength was determined ~1 MPa at 2x10^{-3} s^{-1}. Dynamic tensile fracture tests were also performed in the SHPB at 10 m s^{-1} (not shown here) and the mean tensile strength in these tests increased to ~1.5 MPa, showing a strain rate dependent splitting behavior of tested AAC samples.
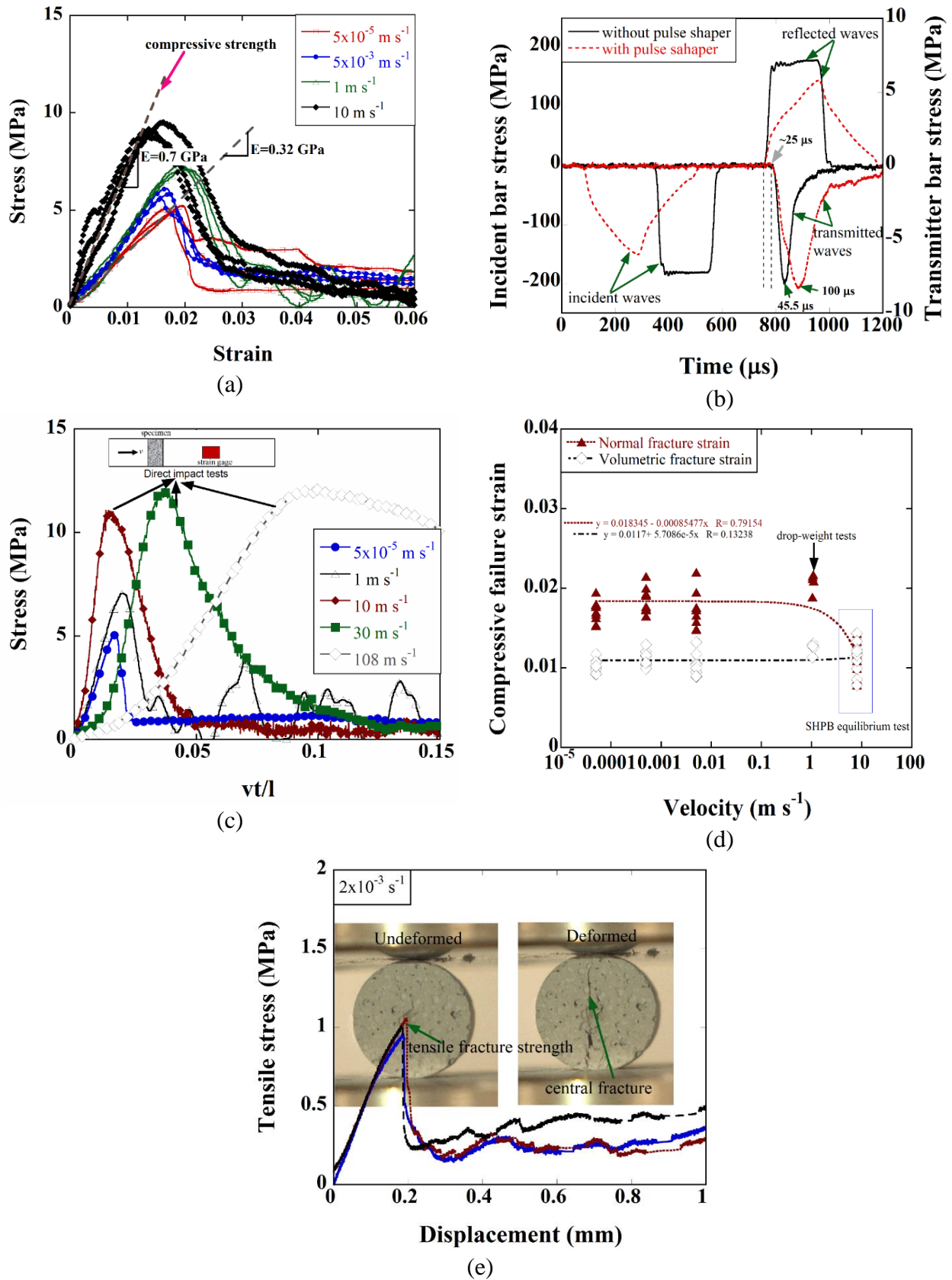
Fig. 2. (a) three stress-strain curves at 5x10⁻⁵, 1 and 10 m s⁻¹, (b) SHPB tests bar stresses with and without pulse shaper at 8 m s⁻¹, (c) typical stress-strain curves at 5x10⁻⁵, 1, 8, 30 and 108 m s⁻¹, (d) the variation of compressive strain with velocity and (e) the quasi-static tensile stress-displacement curves of three Brazilian tests

The failure at quasi-static velocities occurs by the initiation of a single large axial cracks at the bottom compression test platen as shown by the arrows in Figure 3(a). Additional axial cracks are then formed as the upper compression platen continues to compress the sample until about large displacements.

The samples tested at 1 and 10 m s^{-1} also fail similarly, forming few axial cracks starting at the impact-end and/or striker bar/sample contact area, respectively (Figure 3(b) and (c)). However, the extensive cracking of the sample at the impact-end composing of both axial and radial cracks is seen at 30 and 108 m s^{-1} (Figures 3(d) and (e)). The number of cracks also significantly increase at these velocities, clearly indicating the effect of inertia on the fracture behavior of the tested AAC.

Fig. 3. The deformation pictures of the samples tested at (a)5x10^{-5}, (b)1, (c)10, (d)30 and (e)108 m s^{-1}

The variation of the compressive strength with strain rate is shown in Figure 4(a) and may be considered in three sequential distinct regions: a lower velocity-dependent strength region (Region 1) at quasi-static and low velocities, a higher velocity-dependent strength region (Region 2) at intermediate velocities between broadly 10 and 30 m s^{-1} and a constant strength region (Region 3), likely above 30 m s^{-1}. These regions are shown by the numbered-circles in Figure 4(a). The International Federation for Structural Concrete (CEB) recommended two empirical equations to define the DIF of concrete strength as [28]

$$DIF = \frac{\sigma_d}{\sigma_s} = \left(\frac{\dot{\varepsilon}_d}{\dot{\varepsilon}_s}\right)^{1.026\alpha} \qquad \dot{\varepsilon}_d \leq 30 \ s^{-1} \tag{3}$$

$$DIF = \frac{\sigma_d}{\sigma_s} = \gamma \dot{\varepsilon}_d^{1/3} \qquad \dot{\varepsilon}_d > 30 \ s^{-1} \tag{4}$$

where, $\dot{\varepsilon}_d$ and $\dot{\varepsilon}_s$ are the dynamic and static strain rates, respectively. The value of $\dot{\varepsilon}_s$ is 3x10^{-5} s^{-1}, $\gamma = 10^{6.156\alpha-2}$ and $= \frac{1}{(5+\frac{\sigma_s}{10})}$. Fitting the compressive strength values with Eqn. 3, between the lowest quasi-static strain rate and 35 s^{-1} (1 m s^{-1}), and with Eqn. 4 between 35 s^{-1} (1 m s^{-1}) and 1150 s^{-1} (30 m s^{-1}) yield a fracture strength of 4.225 MPa at the reference strain rate, 0.381 for the value of γ and 0.037 for the value of α as depicted in Figure 4(a). As shown in the same figure, the critical strain rate is predicted broadly 100 s^{-1} (~5 m s^{-1}) for rapidly increased compressive strength and 380 s^{-1} (~18 m s^{-1}) or the constant stress region by using Eqn. 4. The compressive strength in Region 2 is also fitted with the following more general equation: $\frac{\sigma_d}{\sigma_s} = \beta \dot{\varepsilon}_d^{n}$, where n=1.113 and β=0.134, resulting in a critical strain rate of ~20 s^{-1} (~1 m s^{-1}) for increased compressive strength in Region 2 and ~760 s^{-1} (~30 m s^{-1}) for the constant stress Region 3. This power equation is noted to be better fitted in Region 2 with the mean DIF values than Eqn. 4 proposed by the CEB as shown in Figure 4(b). A cut-off DIF value of 2.78 above ~1000 s^{-1} (18-30 m s^{-1}) corresponding to a compressive strength of ~11.5 MPa, is also determined for the tested AAC. Figure 4(c) shows the determined compressive strength values of the tested AAC sample using Eqn. 3 at quasi-static velocities and 1, 10, 20, 30, 60 and 108 m s^{-1}. The strength values corresponded to specific test velocities by excluding strength enhancement in Region 2 were used as compressive strength input to the model (Model 2) to determine the strain rate effect on the compressive strength. The experimental mean compressive

strength values are further tabulated in Table 2 together with the corresponding velocity and strain rate.

(a)

(b)

(c)
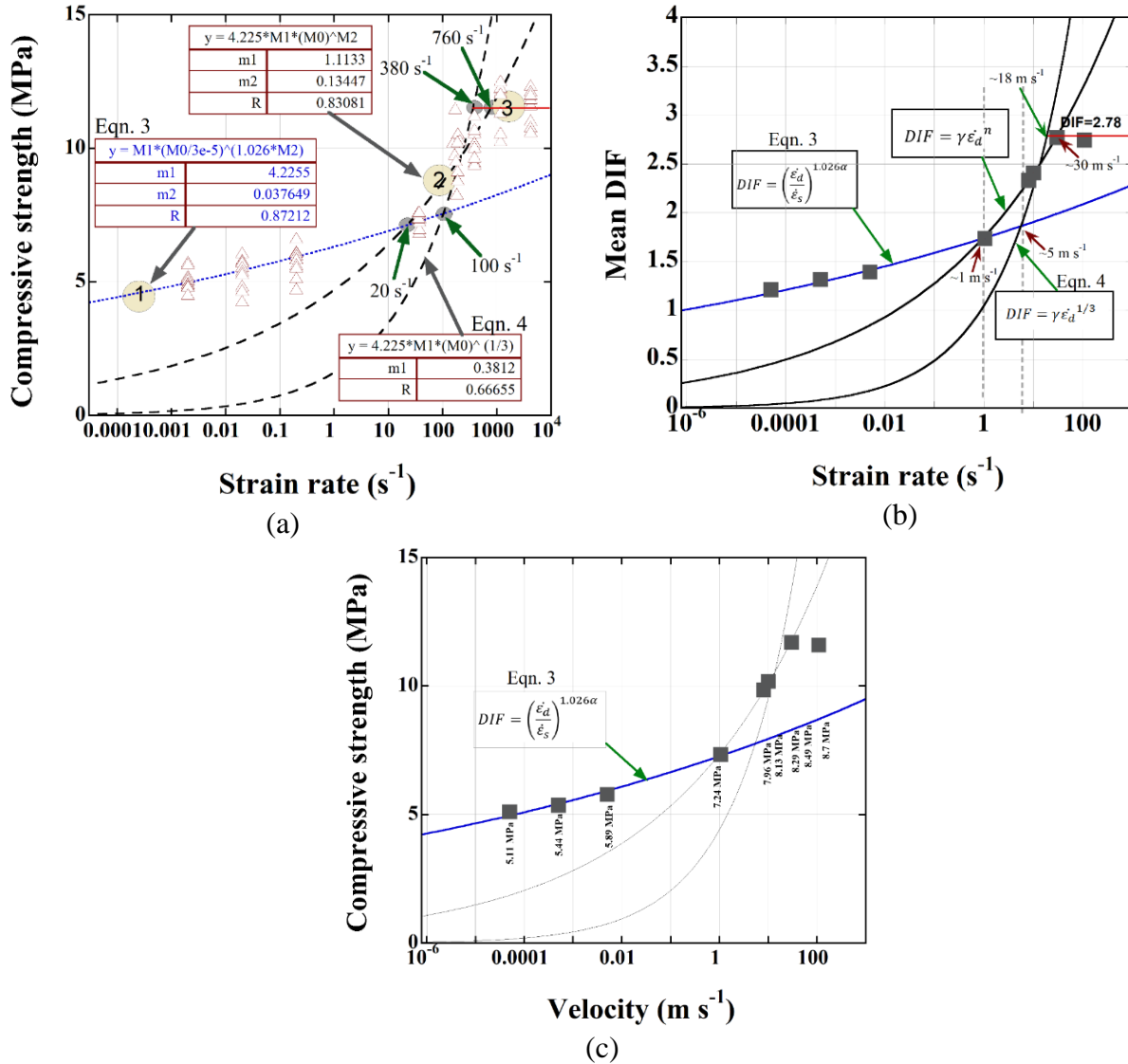
Fig. 4. Experimental (a) compressive strength versus strain rate and fitting with Eqns. 1 and 3, (b) mean DIFs versus velocity and (c) the predicted compressive yield stress of Model 2 at various velocities

Numerical quasi-static and high strain rate compression tests

Figure 5(a) shows the Model 1 numerical stress-$\frac{v}{l}t$ curves at different velocities using a constant compressive strength material model (5. 11 MPa) determined at the quasi-static strain rate of 5×10^{-5} m s^{-1}. Note that only quasi-static compression test at 0.005 m s^{-1} was quasi-statically modelled and the stress in the direct impact SHPB tests were measured both numerically and experimentally 1 m away the sample/incident bar contact area   As similar with experiments, the numerical compressive strength increases with increasing velocity until about 30 m s^{-1}; then it increases slightly with increasing velocity above 30 m s^{-1}. The reduction of the slopes of stress-$\frac{v}{l}t$ curves after about 10 m s^{-1} is also seen numerical stress-$\frac{v}{l}t$ curves but the extent of reduction declines as compared with the tests. The strain gage read numerical compressive strength values are 6, 6.11, 7.2, 8.64, 8.82 and 9.05 MPa sequentially at 1, 10, 20, 30, 60 and 108 m s^{-1}. Compare to experimental

strengths tabulated in Table 2, Model 1 numerical compressive strength values are significantly lower at the same velocities.

Table 2. The mean fracture strength of the quasi-static, drop-weight, SHPB and direct impact compression tests

Velocity (m s^{-1})	Approximate strain rate (s^{-1})	Test	σ_m (MPa)
5x10^{-5}	2x10^{-3}	Quasi-static compression	5.11
5x10^{-4}	2x10^{-2}	Quasi-static compression	5.37
5x10^{-3}	2x10^{-1}	Quasi-static compression	5.89
1	35	Drop-weight	7.34
8	185	SHPB	9.9
10	385	Direct impact	10.2
30	1150	Direct impact	11.70
108	4150	Direct impact	11.60

When the compression strength is taken strain rate dependent that is the corresponding to compressive strength values at each velocity are input to the material model (Model 2), the numerical compressive strengths increase as seen in Figure 5(b).
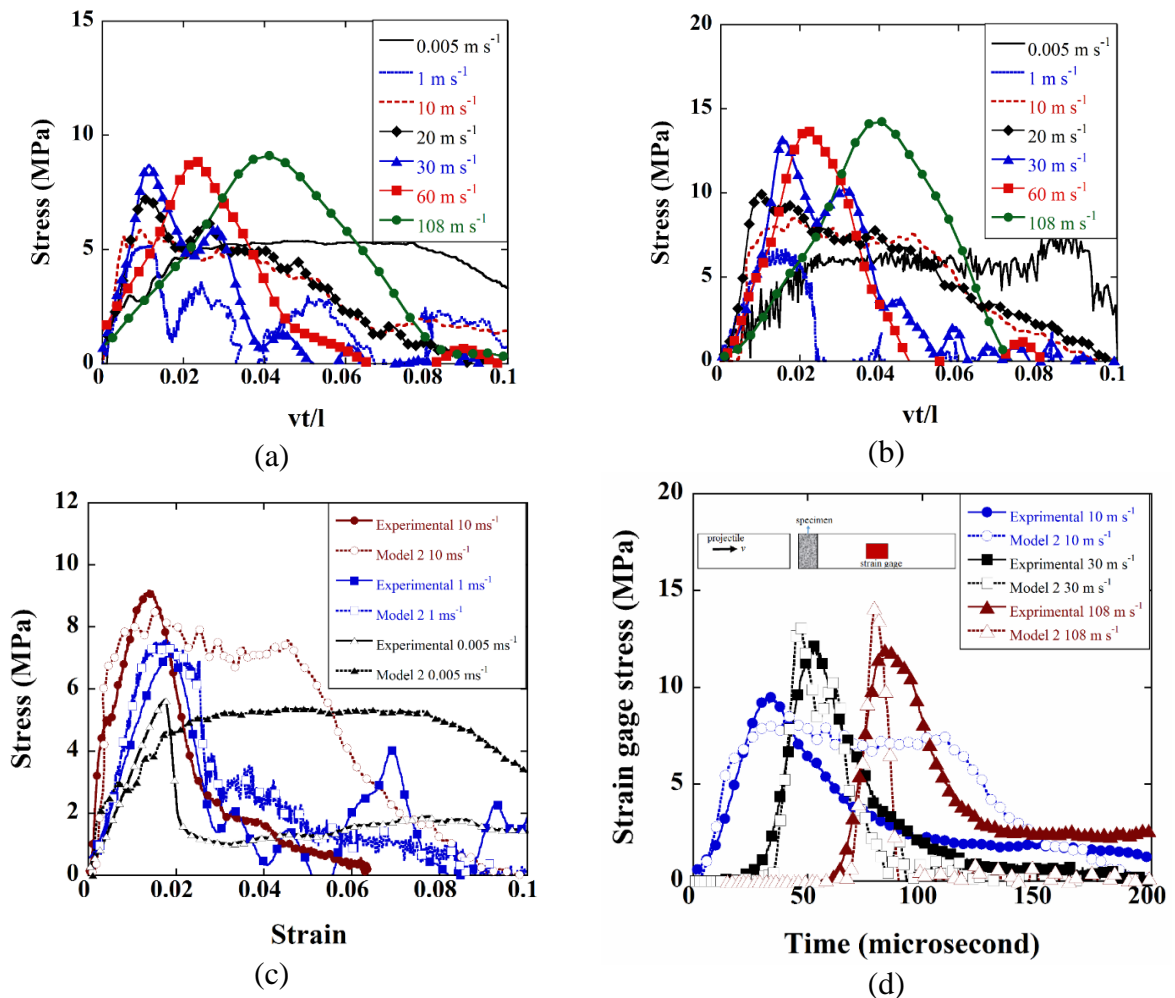
Fig. 5. The numerical stress-strain curves at different velocities; (a) Model 1 and (b) Model 2 and comparison of experimental and model 2 (c) stress-strain and (d) strain gage stress-time curves

Figures 5(c) and 5(d) show the stress-strain and stress-time curves between 0.005 and 8 m s^{-1} and between 10 and 108 m s^{-1}, respectively. The strain gage read numerical compressive strength values in Model 2 increase to 6.4, 6.7, 8.48, 10, 13.1, 13.68 and 14.2 MPa sequentially at 0.005, 1, 10, 20, 30, 60 and 108 m s^{-1} and become much more comparable with the experimental compressive strength values tabulated in Table 2. Also noted in Figures 5(c) and (d), the experimentally measured gage compressive strength values are higher than those of Model 2 until about 10 m s^{-1}; thereafter, Model 2 strength values becomes higher at 30 and 108 m s^{-1}. The post-failure regions of experimental and model curves are also different, Model 2 show a more progressive failure than the experiments. Despite these differences between the gage-measured stress of models and experiments, Model 2 and Model 1 show pretty well the trends of compressive strength

Fig. 6. The numerical deformation pictures of the samples tested at (a)quasi-static, (b)1, (c)10, (d)20, (e) 30, (f) 60, and (g) 108 m s^{-1}

variation with velocity. After this verification, the model compressive strength values were determined at the distal-end and impact-end contact areas as well as the elements at the center and surface of the sample at both distal-end and impact-end.

Figures 6(a-g) show Model 1 numerical deformation pictures (at various deformation times) at 0.005, 1, 10, 20, 30, 60 and 108 m s^{-1}, respectively.

The corresponding 3D views of the characteristic damage progression modes (after about compressive strength) between 1 and 108 m s^{-1} are also depicted in Figure 7. As marked by arrows in Figure 6(a-c), the cracks initiate either at one end or at both ends of the samples, while later these initial cracks turn to one or two large axial cracks at increasing times at 0.005, 1 and 10 m s^{-1}. This explained numerical axial cracking behavior also seen in Figure 7 at 1 and 10 m s^{-1}, and is pretty much comparable with the experimental fracture behavior at the same velocities, as depicted in Figure 3. However, the cracks initiate at the impact-end and are proceeded by radial cracking at 20 m s^{-1} and above as shown in Figures 6(d-g) and Figure 7. Again, the numerical facture shows well matching with the experimental facture at 30 and 108 m s^{-1} shown in Figure 3. Model 2 deformation and failure

modes at varying velocities were also found very similar with Model 1, except the facture occurred at higher stresses.

Figure 8 shows the variation of numerical distal-end DIFs with the logarithm of velocity. In the same figure, the experimentally measured strain-gage DIFs are also shown for comparison. A rapid increase in the experimental and numerical DIFs after about 1 m s^{-1} is clearly seen in the same figure. The increase in the DIFs is noted to continue until about 30 m s^{-1}. The experimental DIFs however show a sudden cut-off at about 30 m s^{-1}, while both Model 1 and Model 2 DIFs increase with increasing velocity above 30 m s^{-1}. The DIFs of Model 1 however increases relatively slowly above 30 m s^{-1}, while the increase in Model 2 is comparably higher. This difference is attributed to the velocity dependent compressive yield stress used in Model 2. As Model 1 uses a constant compressive yield stress it shows merely the effect of axial and radial inertia on the DIF values, while Model 2 shows both the effects of inertia and strain rate. The modeling results tend to conclude that inertia is effective with increasing velocity between 1 and 30 m s^{-1}. Experimentally, it is presumed that AAC sample reaches a shock compressive strength in Region 2 without entering Region 3. A similar conclusion may be made for Model 1. While, in Model 2, the compressive yield stress also increases in Region 3. Although Model 1 resembles the experimental DIFs by a constant compressive strength in Region 3, Model 2 resembles the experimental DIFs in both Region 1 and Region 2. Nevertheless, both models show an "s-type" DIF-velocity graph, proving the transformation of the deformation state form 1D stress to 1D strain. Lastly, although the proposed power law equation shows well matching with the experimental and model DIFs at lower velocities in Region 2, Eqn. 4 better predicts Model 2 DIFs at higher velocities, ~30 m s^{-1}.
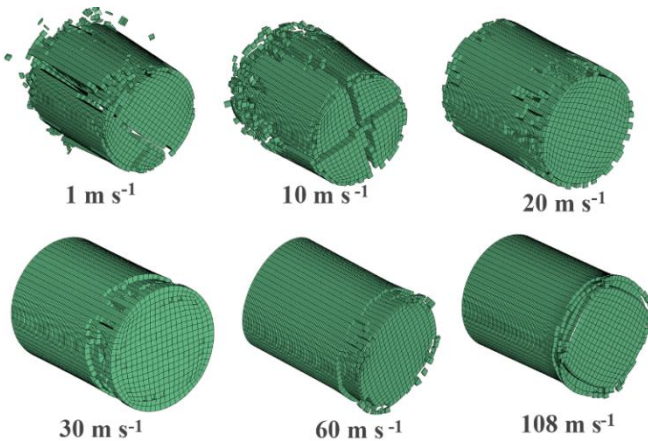
Fig. 7. Model 1 numerical failure modes at different velocities
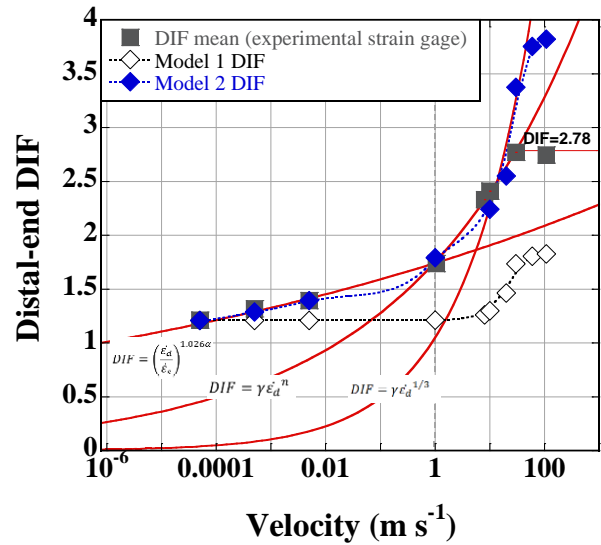
Fig. 8. The variations of experimental and numerical DIFs and numerical contact stresses with velocity

Figures 9 (a-e) show the variation of Model 1 impact-end, distal-end and distal–end center and surface element stresses with time sequentially at 1,10, 20, 30 and 60 m s^{-1}. The element stresses were determined from the selected center and surface element at the distal-end, while impact-end and distal-end stresses were calculated from all elements at the surface of the sample. The time difference between the impact and distal-end stresses in the same figures is due to the wave-transit-time of AAC sample. Figures 9(a-e) clearly indicate that the impact-end and distal-end stresses are similar until about 20 m s^{-1}, while the center and surface element stresses starts to differentiate at about 10 m s^{-1}. The center element stress is higher than the surface element stress until about 20 m s^{-1}, then the surface element stress increases over that of the center element stress at higher velocities, proving the transformation of the failure from an axial to a radial fracture.
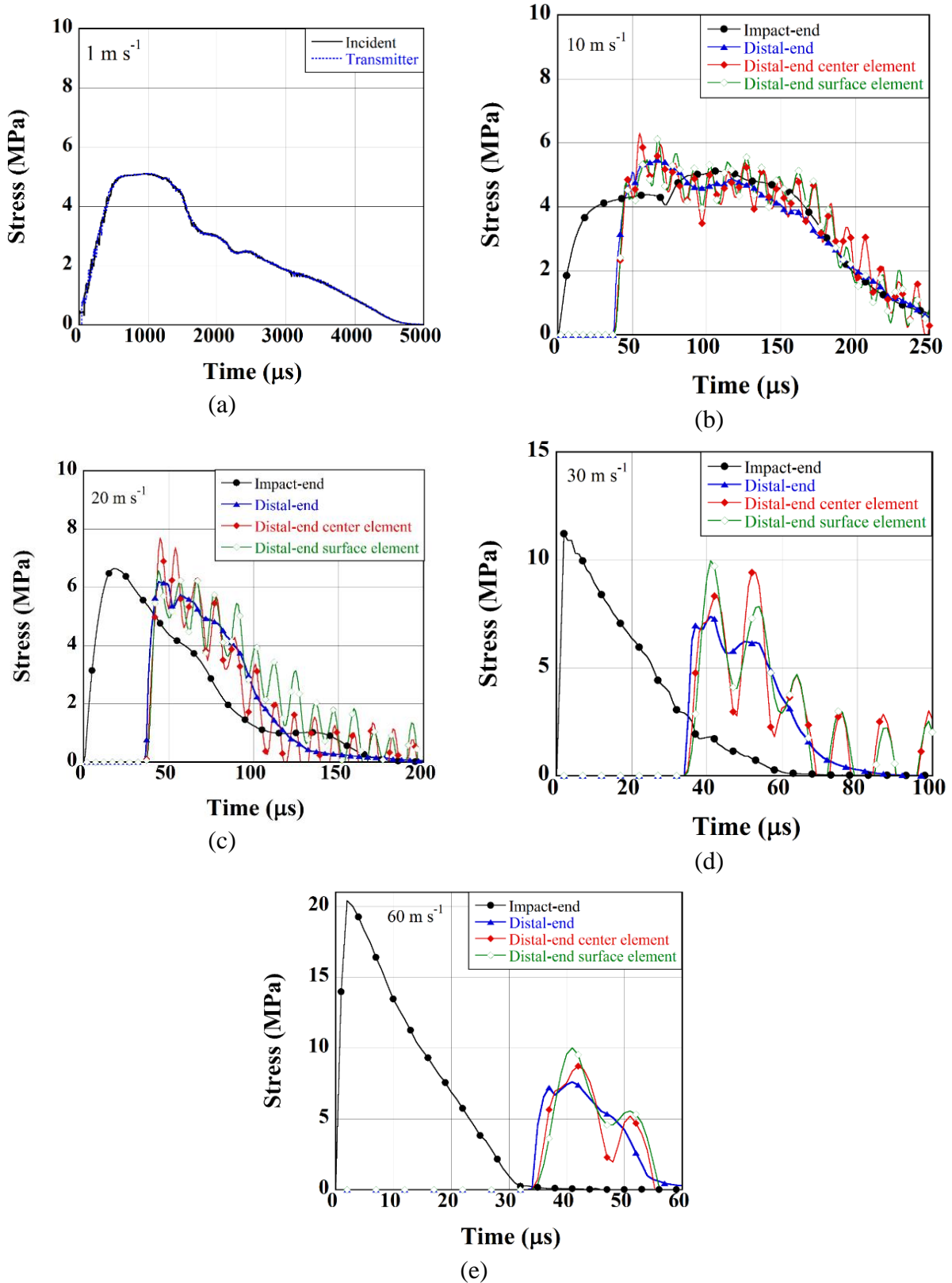
Fig. 9. The variation of Model 1 impact-end, distal-end, distal–end center and surface element and strain gage location stresses with time at (a)1, (b)10, (c) 20, (d) 30 and (e) 60 m s⁻¹

The stress triaxiality is defined as

$$\eta_{1D\ stress} = \frac{\sigma_x + \sigma_y + \sigma_z}{3\sigma_{eq}} \qquad (5)$$

where σ_x, σ_y and σ_z are stresses on x, y and z directions and σ_{eq} is equivalent stress. The equivalent stress is

$$\sigma_{eq} = \frac{1}{\sqrt{2}}\left[(\sigma_x - \sigma_y)^2 + (\sigma_y - \sigma_z)^2 + (\sigma_z - \sigma_x)^2 + 6(\tau_{xy}^2 + \tau_{yz}^2 + \tau_{xz}^2)\right]^{\frac{1}{2}} \tag{6}$$

Since $\sigma_{eq} = \sigma_x$ in the quasi-static test, $\eta_{1D\,stress} \approx 0.33$. Assuming fully confined elastic state at high strain rates, the stress triaxiality is

$$\eta = \frac{1+v}{3(1-2v)} \tag{7}$$

By taking the Poisson's ratio equals to 0.2, the stress triaxiality approaches to ~0.66 for a full 1D state of strain. Figure 10 shows the Model 1 and Model 2 distal-end and impact end DIFs together with the Model 1 impact-end surface element stress triaxiality (non-eroded element). The numerical stress triaxiality increases with increasing velocity after about 10 m s^{-1} (35 s^{-1}) and reaches a steady value of 0.66 at about 30 m s^{-1} (marked by an arrow in Figure 10). The result clearly indicates a full uniaxial state of strain attainment in the numerically tested samples after about 30 m s^{-1} (1000 s^{-1}). Modelling SHPB tests on a concrete using a pressure dependent strength model previously showed a stress triaxiality (η) was near 1D state of stress ($\eta = -0.33$) at 47 s^{-1}, while it reached 1D state of strain ($\eta = -0.66$) at ~795 s^{-1} when $v = 0.2$ [15]. Above this critical strain rate, the sample deformation was completely 1D state of strain. Furthermore, the critical strain rate for the passage to 1D state of strain was shown to depend on the diameter of sample, larger diameter samples showed larger inertial effects hence lower critical strain rate for the complete 1D state of strain [15]. In the present study relatively small samples were used, 19.4 mm in diameter and 26 mm in length. The transformation strain rate from the uniaxial state of stress to the uniaxial state of strain is found 1150 s^{-1}, which is also very much consistent with the previous numerical simulations on concrete [15].

Assuming cellular concrete deforms in 1D state of strain by forming a shock front depicted in Fig. 11, the impact end-stress (σ^*) is governed by the following rigid-perfectly-plastic-locking (r-p-p-l) model, based on mass and momentum conservation as [29],
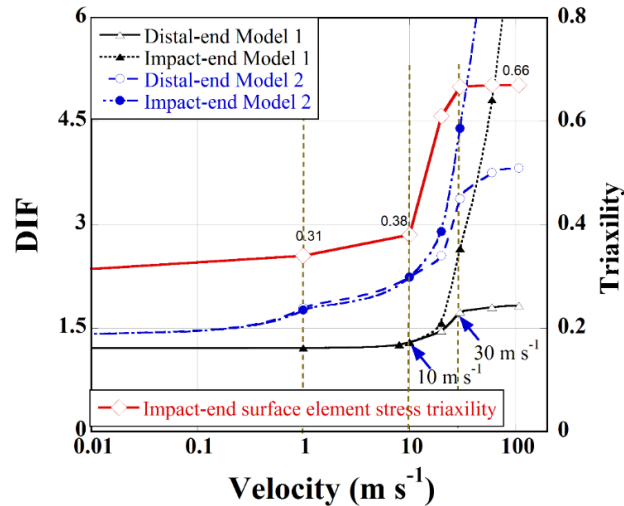
Fig. 10. Experimental and numerical DIFs together with distal-end stress triaxiality

$$\sigma^* = \sigma_p + \frac{\rho_o}{\varepsilon_d}v_o^2 \tag{8}$$

In above equation, σ_p is the plateau stress, v_o is the initial velocity, ρ_o is the initial density and ε_d is the densification strain. The plateau stress of present AAC sample is determined using Eqn. 3 for the strain rate sensitive case (Model 2) as

$$\sigma_p = \sigma_s \left(\frac{v}{v_s}\right)^{1.026\alpha} \tag{9}$$

where, v is the impact velocity and v_s is the reference velocity corresponding to the reference strain rate. The determined experimental values of σ_s and v_s are 4.225 MPa and 7.8×10^{-7} m s^{-1}, respectively. A constant plateau stress of 5.11 MPa is taken for the strain rate insensitive case (Model 1). The densification strain was determined from confining compression tests on AAC samples. Simply, a cylindrical sample was tightly fitted inside a cylindrical tube, then the sample was compressed with a flat end punch. Figure 11(a) shows the confinement stress-strain curves of these tests together with the picture of tested sample before and after the test. The densification of the sample is clearly seen in these pictures, showing a nearly full confined state. The densification strain is determined 0.28 by using a liner intercept method as shown in Figure 11(a).
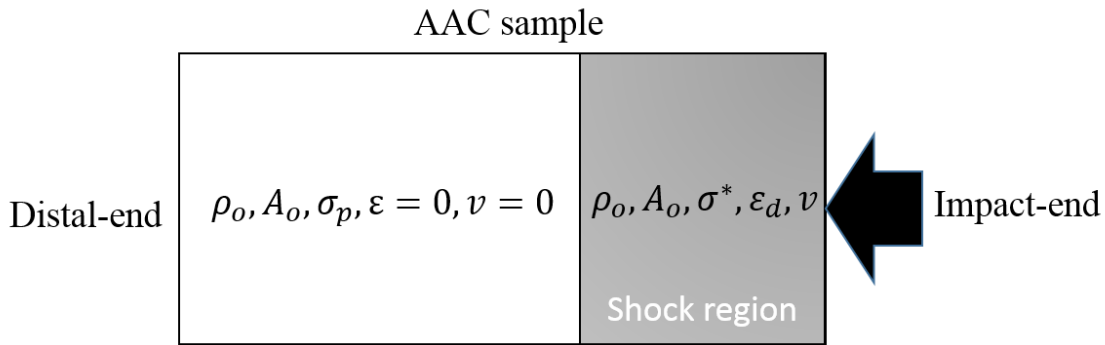
AAC sample

Fig. 11. Schematic of shock formation in AAC sample

The predicted impact-end stresses using Eqn. 8 and Eqn. 9 are shown as function of the logarithm of velocity in Figure 11(b) and (c) together with experimental and numerical distal-end and impact end DIFs, respectively. The predictions result in critical velocities near 10 m s^{-1} for the increased impact-end stresses for 1D state of strain as shown in the same figures. This also shows a good match with the experimental and numerical results.

Conclusions. The effect of inertia and strain rate on the failure of a cellular concrete (600 kg m^{-3}) was investigated using a constant volumetric-failure-strain erosion criterion in LSDYNA. Two modelling approach, namely rate insensitive (constant compressive yield stress) and rate sensitive (variable compressive yield stress) were implemented and the results were compared with the experimental compression tests performed at similar strain rates, between 2×10^{-3} s^{-1} and ~ 4150 s^{-1}. The effect of inertia in increasing the compressive strength of cellular concrete at increasing strain rates was shown both experimentally and numerically. An "s-type" compressive strength relation with strain rate was also found, composing of three different distinct regions: a lower velocity-dependent strength region at the quasi-static velocities (Region 1), a higher velocity-dependent strength region at intermediate velocities (Region 2) and again a lower velocity-dependent strength region above about 1150 s^{-1} (Region 3). In experimentally tested samples, a shock compressive strength was presumed to be reached in Region 2 or just at the beginning of Region 3, resulting in a cut-off DIF value (2.78), while in numerically tested samples, the compressive strength (Model 2) increased even in Region 3 with a rate very much similar to that of Region 1. One dimensional state of strain condition above a critical velocity was also shown numerically and the stress triaxiality increased to 0.66 within 1 and 30 m s^{-1}, reaching a fully constraint 1D state of strain condition above 30 m s^{-1}. In accord with this, the numerical fracture mode, as with the experiments, switched from an axial-dominated to a radial-dominated cracking after about 20 m s^{-1}. A simple shock analysis also proved 1D state of strain after about 10 m s^{-1}. Finally, the strain rate dependent compressive strength was numerically presented as partly due to the change of the deformation state from a 1D state of stress to an1D state of strain and partly due to the intrinsic rate sensitivity of cellular concrete.

Burak AKYOL, Mustafa GÜDEN
A constant volumetric-failure-strain erosion for determining the effect of inertia and strain rate on the crushing strength of a cellular concrete
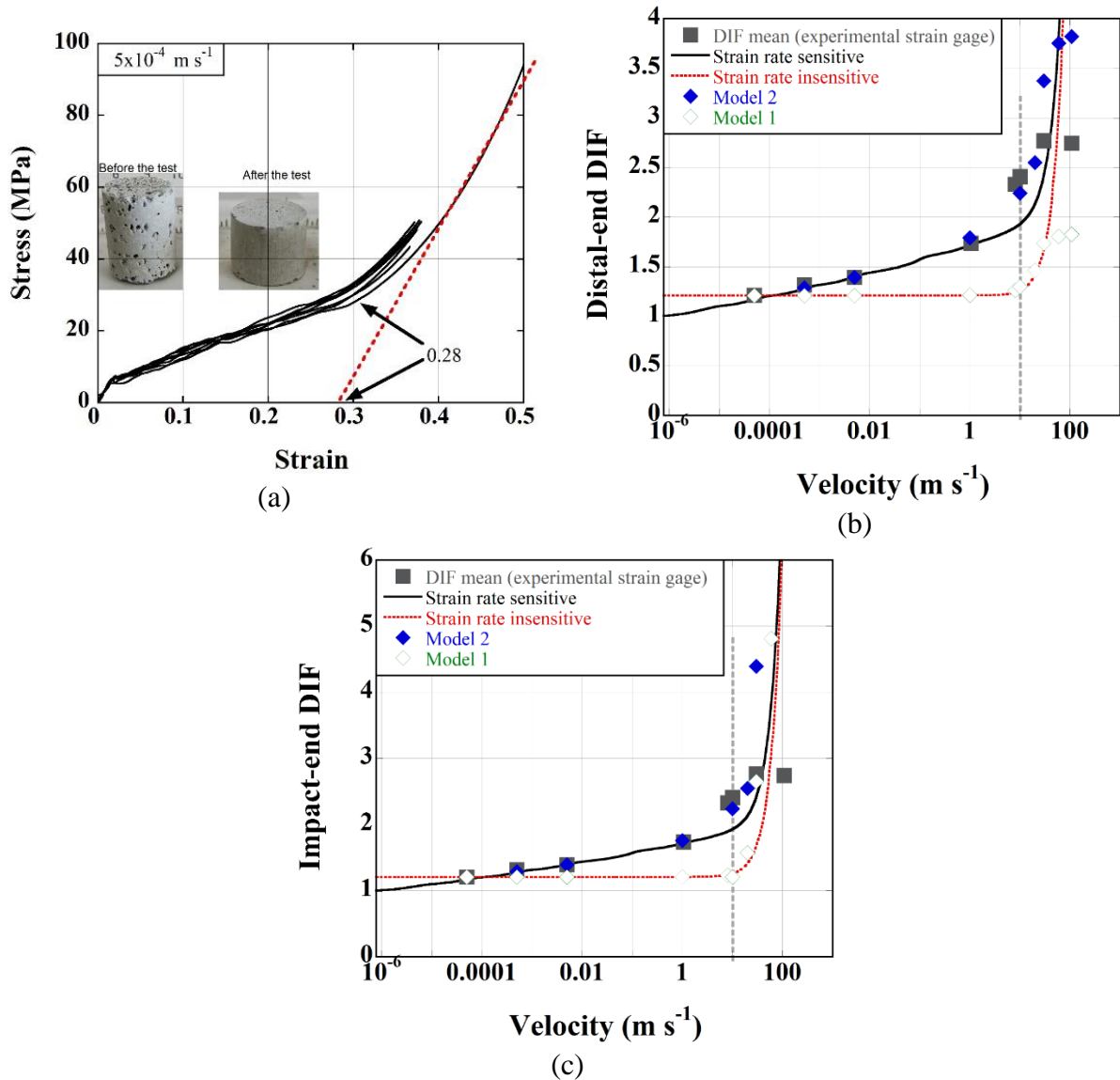
Fig. 12. (a) confined compression stress-strain curves and (b) distal-end and (c) impact-end stress prediction based on r-p-p-l model

REFERENCES

[1]. Khosravani, M.R., Weinberg, K. *A review on split Hopkinson bar experiments on the dynamic characterisation of concrete.* Construction and Building Materials, 2018, 190, pp. 1264-1283.

[2]. Bischoff, P.H., Perry, S.H. *Compressive behavior of concrete at high-strain rates.* Materials and Structures, 1991, 24, 425-450.

[3]. Zhang, Q.B., Zhao, J. *A Review of Dynamic Experimental Techniques and Mechanical Behaviour of Rock Materials.* Rock Mechanics and Rock Engineering, 2014, 47, pp. 1411-1478.

[4]. Lu, D.C., Wang, G.S., Du, X.L., Wang, Y., 2017. *A nonlinear dynamic uniaxial strength criterion that considers the ultimate dynamic strength of concrete.* Int. J. Impact Eng., 2017, 103, pp. 124-137.

[5]. Rossi, P., Toutlemonde, F.J.M. *Effect of loading rate on the tensile behaviour of concrete: description of the physical mechanisms.* Materials and Structures, 1996, 29, pp. 116-118.

[6]. Brace, W.F., Jones, A.H. *Comparison of uniaxial deformation in shock and static loading of three rocks.* Journal of Geophysical Research, 1971, 76, pp. 4913-4921.

[7]. Zeng, S.J., Ren, X.D., Li, J. *Triaxial Behavior of Concrete Subjected to Dynamic Compression.* Journal of Structural Engineering, 2013, 139, pp. 1582-1592.

[8]. Legeron, F., Paultre, P. *Uniaxial confinement model for normal- and high-strength concrete columns.* Journal of Structural Engineering-Asce, 2003, 129, pp. 241-252.

[9]. Sfer, D., Carol, I., Gettu, R., Etse, G. *Study of the behavior of concrete under triaxial compression.* Journal of Engineering Mechanics-Asce, 2002, 128, pp. 156-163.

[10]. Lahlou, K., Lachemi, M., Aitcin, P.C. *Confined high-strength concrete under dynamic compressive loading.* Journal of Structural Engineering-Asce, 1999, 125, pp. 1100-1108.

[11]. Li, X.G., Liu, Z.L., Lv, Y., Cai, L.X., Jiang, D.B., Jiang, W.G., Jian, S.W. *Utilization of municipal solid waste incineration bottom ash in autoclaved aerated concrete.* Construction and Building Materials, 2018, 178, pp. 175-182.

[12]. Lee, S., Kim, K.M., Park, J., Cho, J.Y. *Pure rate effect on the concrete compressive strength in the split Hopkinson pressure bar test.* Int. J. Impact Eng., 2018, 113, pp. 191-202.

[13]. Grady, D.E., 1998. *Shock-wave compression of brittle solids.* Mechanics of Materials, 1998, 29, pp. 181-203.

[14]. Yu, S.S., Lu, Y.B., Cai, Y. *The strain-rate effect of engineering materials and its unified model.* Latin American Journal of Solids and Structures, 2013, 10, pp. 833-844.

[15]. Liu, F., Li, Q.M. *Strain-rate effect on the compressive strength of brittle materials and its implementation into material strength model.* Int. J. Impact Eng., 2019, 130, pp. 113-123.

[16]. Yankelevsky, D.Z., Avnon, I., 1998. *Autoclaved aerated concrete behavior under explosive action*, Construction and Building Materials, 1998, 12, pp. 359-364.

[17]. Serrano-Perez, J.C., Vaidya, U.K., Uddin, N. *Low velocity impact response of autoclaved aerated concrete/CFRP sandwich plates.* Composite Structures, 2007, 80, pp. 621-630.

[18]. Mespoulet, J., Plassard, F., Hereil, P.L., *Strain rate sensitivity of autoclaved aerated concrete from quasi-static regime to shock loading.* Dymat 2015 - 11th International Conference on the Mechanical and Physical Behaviour of Materials under Dynamic Loading, E D P Sciences, Cedex A.

[19]. Nian, W., Subramaniam, K.V., Andreopoulos, Y. *Experimental investigation on blast response of cellular concrete.* Int. J. Impact Eng., 2016, 96, pp. 105-115.

[20]. Odac, I.K., Guden, M., Klcaslan, C., Tasdemirci, A. *The varying densification strain in a multi-layer aluminum corrugate structure: Direct impact testing and layer-wise numerical modelling.* Int. J. Impact Eng., 2017, 103, pp. 64-75.

[21]. Sankaya, M., Tasdemirci, A., Guden, M. *Dynamic crushing behavior of a multilayer thin-walled aluminum corrugated core: The effect of velocity and imperfection.* Thin-Walled Struct., 2018, 132, pp. 332-349.

[22]. Sarikaya, M., Tasdemirci, A., Guden, M. *Impact loading and modelling a multilayer aluminium corrugated/fin core: The effect of the insertion of imperfect fin layers.* Strain, 2019, 55, p. 17.

[23]. Li, Z., Chen, L., Fang, Q., Hao, H., Zhang, Y., Chen, W., Xiang, H., Bao, Q. *Study of autoclaved aerated concrete masonry walls under vented gas explosions.* Engineering Structures, 2017, 141, pp. 444-460.

[24]. Oliver, J., 1989. *A consistent characteristic length for smeared cracking models.* International Journal for Numerical Methods in Engineering, 1989, 28, pp. 461-474.

[25]. Govindjee, S., Kay, G.J., Simo, J.C. *Anisotropic modeling and numerical-simulation of brittle damage in concrete.* International Journal for Numerical Methods in Engineering, 1995, 38, pp. 3611-3633.

[26]. Halquist, J. *LS-DYNA keyword user's manual version 971*. Livermore Software Technology Corporation, 2007, Livermore, CA.

[27]. Ravichandran, G., Subhash, G. *Critical-appraisal of limiting strain rates for compression testing of ceramics in a split hopkinson pressure bar*. Journal of the American Ceramic Society, 1994, 77, pp. 263-267.

[28]. CEB, *Concrete structures under impact and impulsive loading*. Bulletin d'information, 1998, No 187, CEB Comite´ EuroInternational du Be´ton, Lausanne.

[29]. Reid, S.R., Peng, C. *Dynamic uniaxial crushing of wood*. Int. J. Impact Eng., 1997, 19, pp. 531-570.

INDIRECT INK TRANSFER FOR OFFSET PRINTING, TAKING INTO ACCOUNT THE ROUGHNESS OF THE OFFSET PRINTING PLATE SURFACE

Eldar ALIYEV[1], Isa KHALILOV[2], Shabnam ISMAILOVA[3*]

[1,2,3]Department of Mechatronics and Machine Design, Azerbaijan Technical University
Baku, Azerbaijan

E-mail: elab57@mail.ru[1] , khalilov@aztu.edu.az[2], shebinem.ismayilova@aztu.edu.az[3]*

Abstract: This article is devoted to the study of the influence of the surface roughness of an offset printing plate on the form-decal contact and deckle-printed material. Taking into account the deepening of micro protrusions of the surface roughness of the printing plate into the body of the deckle, which lead to additional displacements and deformation of the deckle, the amount of ink on the surface of the form is determined. The separation and transition of the paint layer in the contact zone has been studied. It has been established that the ink layer located in the free space of the roughness of the surface of the printing plate is also involved in the transfer of ink. The proposed method of indirect ink transfer in offset printing allows you to determine more accurate values of consumables in the design of printing processes, also predict the quality of printed prints, determine the runtime of printing plates, and correctly configure the printing machine before the printing process.

Key words: offset printing, contact area, roughness, deckle, ink transfer

Introduction. To obtain prints in any number of copies in the printing process, the printing ink is transferred from the ink apparatus to the printing plate and from the form to the printed material [1-3]. The printing apparatus is one of the main components of the printing machine. It serves to transfer a certain amount of ink from the printing elements of the form to the printed material at sufficient specific pressure and to guide the printed material through the printing zone.

The actions of printing devices are associated with the type of printing form and the type of printed material [1,2].

The transfer of information from the printed form to the material can occur directly or indirectly [2]. Indirect ink transfers during offset printing is carried out in two stages. The ink layer located on the printing form comes into contact with the rubber-cloth plate (with the decal) of the offset cylinder. In this case, part of the layer remains on the surface of the plate. After that, the ink transfers to the printed material when the offset cylinder plate comes into contact with it, where the adhesive forces that act between the printing ink and the printing plate as well as the blanket of the offset cylinder and the printed material are always less than the cohesive forces acting in the printing ink [3]. The above makes the necessary separation of ink into layers possible.

It has been established that with an increase in the specific printing pressure of ink-absorbing materials, the ink transfer coefficient and the amount of ink transferred increase to a maximum value [2].

In [4, 5], the frictional interaction of a two-layer elastic body and a rough indenter was studied, which corresponds to the phenomena occurring in the printed contact zone. The research results show that the contact of a rough body with an elastic one leads to additional displacements. These

displacements, which are determined by the deepening of the micro roughness of the surface roughness, affect the values of the deformation of the elastic body.

Based on the foregoing, it can be concluded that when studying a printed pair, it is necessary to take into account the roughness of a more rigid surface, i.e., the surface roughness of the printing plate. This, in turn, will make it possible to obtain more accurate values of the specific pressure, as well as the ink transfer coefficient and the amount of ink transferred, which determine the quality of prints and the runtime of the printing plate.

The study of the influence of the geometric parameters of the printing pair, therefore, the micro-geometry of the printing plate surface on the ink transfer coefficient and the amount of ink transferred, as well as on the quality of the prints is a very topical task.

The purpose of this article is to investigate the indirect transition of ink in offset printing, taking into account the roughness of the printing plate surface.

In order to achieve the goal, the following tasks were set:

- To determine the scheme of ink layer separation, also the interaction of elastic deckle and printing plate, taking into account the roughness of the surface of the printing plate. To determine theoretically the influence of printing plate surface roughness on ink quantity and on ink layer separation and transfer;

- to choose a method of estimation of ink quantity and ink layer separation taking into account micro geometry of printing plate surface.

Literature review and problem statement. In work [2], ink separations in the areas of printing form - offset plate and offset plate - printed material were studied. For this purpose, a scheme for ink separation is proposed and the amount of ink transferred from the printing plate to the deckle and from the deckle to the printed material is determined. For ink transfer, the Reynolds equation was derived based on the theory of elastohydrodynamic lubrication, and a model of the relationship between roller parameters, speed, pressure, and ink thickness in the ink roller gap was established using Hertz's contact theory [6]. The influence of speed, pressure and roller size on the thickness of the ink in the gaps of the ink rollers was analyzed. In addition, the ink transfer model was modified to take into account ink retention in the gaps of the ink rollers. The effect of print speed on ink performance was analyzed using a computer simulation method.

An ink apparatus [7] was used to study the effect of adding and evaporating a stabilized alcohol solution and a thin-film emulsion of offset inks on emulsion transfer. It has been found that by introducing a certain non-absorbent substrate in a single pass between the rollers, emulsion transfer can be achieved. By expressing the behavior as a function of the ratio of the emulsion component to the inks, it became possible to study the effect on the optical properties of the final thin layer in the form of a print.

Numerical simulations were used to evaluate the applicability and limitations of optical micro-roughness measurement for coated paper and ink [8]. Experimental results are presented for a number of inks on substrates of different macro-roughness.

The evaluation of a series of commercial raw, semi-matte and glossy coated papers for multi-color sheet offset printing is presented [9]. This research is aimed at better understanding the mutual influence of the free energy of the surface, the roughness of the paper surface and the fountain solution on the print spotting that occurs in full-format printing conditions.

The results of studies of the relationship between the properties of paper and the optical density or color coverage of printed paper have shown that the basic density increases with an increase in the amount of ink before the basic density reaches saturation [10].

The uniformity of water absorption and the structure of the coating on pilot-coated paper with different types and dosages of dispersants have been studied [11]. It was found that most of the samples with uneven water-moisture absorption and uneven reflectance to burn-in tended to have more severe printing problems related to surface moisture/water.

The effect of paper surface properties, including surface free energy, smoothness and gloss of some standard papers used in lithography, on ink transfer was analyzed by comparing the colorimetric values defined by ISO 12647-2:2013 [12]. Determination of the amount of ink transfer, optical density, mottling and difference in color of prints was performed to evaluate the interaction of paper with inks. The results showed that the amount of ink used to obtain a standardized print varies for different types of paper (even within the same ISO classification).

The mechanism of formation of serious bulk-type defects in a system with reverse offset printing operating at high speed was discussed [13]. A mathematical formula is proposed describing the temperature distribution in the ink block of an offset printing machine caused by the phenomenon of friction between cylinders that remain in contact [14].

It has been established that with an increase in the surface roughness of the printing plate, the value of the relative gear ratio α for elastic decals decreases, which contributes to the transfer of ink [15]. One of the most important criteria for print quality is the control of the point gain level. A CtP calibration method used for the manufacture of a printing plate is proposed, which calibrates the point gain in accordance with the recommendations of ISO 12647-2:2013 completely automatically in parallel with printing [16].

The printing mechanism and performance of the high-precision depth-shift printed circuit technology has been investigated from the point of view of the main printing parameters through experimental and theoretical analysis [17]. The ink transfer mechanism is theoretically analyzed for different solvent content using Surface Evolver. The calculation results are compared with the experimental results.

It has been established that within the standardization of the offset printing process, one of the most important tasks is the correct choice of the components of the printing system, taking into account the peculiarities of their interaction and behavior during the printing process [18]. For this purpose, a software product has been developed to calculate the ink transfer to the printed material between the contacting cylindrical surfaces of a sheet-fed offset printer with deformation boundaries.

In offset printing, a process of transfer of a viscous incompressible liquid (ink) is observed [19]. Simulation of the ink flow between rotating cylinders with subsequent crushing of the ink film is carried out using finite difference methods.

It has been established that differences in the values of viscosity, stickiness and fluidity of inks affect such parameters as adhesion, transferability and print stability [20].

Special experimental tests of coatings and industrial printing were carried out, designed to obtain fundamental knowledge about the violation of the adhesion of paints on coated paper [21].

Theoretically, the ink transfer to the printing plate was studied taking into account the surface roughness of the printing plate [22]. However, the paper does not consider and does not compare theoretical data with experimental ones.

Based on the analysis of published scientific papers, the following conclusions can be drawn about the state of the problem of ink transfer and the interaction of an elastic deckle with a printing plate in offset printing:

In studies (except work 22), the assessment of the amount of ink and the separation of the ink layer, as well as the interaction between the elastic deckle and the printing plate, were determined without taking into account the surface roughness of the printing plate.

Influence of mold surface (7) roughness on the amount and transfer of paint.

To study the influence of the surface roughness of the printing plate on the separation of ink in an indirect printing method, the scheme (Figure 1), which is proposed in work [22], is considered.

Eldar ALIYEV, Isa KHALILOV, Shabnam ISMAILOVA
Indirect ink transfer for offset printing, taking into account the roughness of the offset printing plate surface
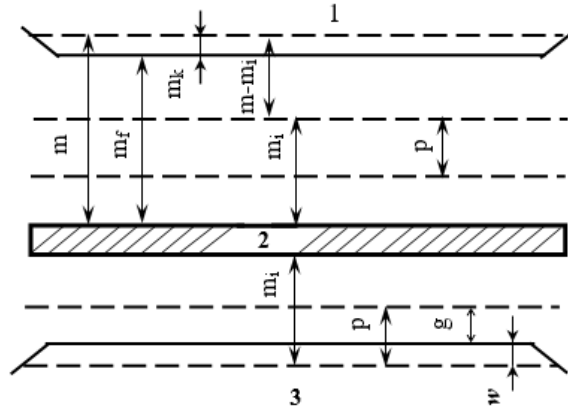
Fig 1. Scheme of separation of the ink layer with an indirect printing method

The diagram (Figure 1) shows the following designations:

1 - printing form; 2 - offset rubber-fabric plate; 3 - paper; m is the amount of ink on the printing plate before printing; $m_f -$ is the amount of ink lying freely on the surface of the printing plate, without regard to roughness; $m_k -$ is the amount of ink that is in the free space of the surface roughness of the printing plate. $p -$ the amount of ink transferred to the printed material; mi is the amount of ink on the blanket of the offset cylinder before transferring to the printed material; g is the amount of ink lying freely on the material; w is the amount of ink absorbed by the printed material during the printing process. Given the parameters m_f and m_k the amount of ink m on the printing plate before printing is defined as follows.

$$m = m_f + m_k \tag{1}$$

According to this scheme (Figure 1), ink separations in two contact zones were studied: printing plate - offset plate and offset plate - printed material. Therefore, two ink layer separation coefficients are defined for them.

First zone: printing plate - offset plate (deckle)

$$v = \frac{m_i}{(m_f + m_k) - m_i} \tag{2}$$

second zone: offset plate - printed material

$$v_i = \frac{p}{(m_i - p)} \tag{3}$$

The transfer of ink from the printing plate to the rubber fabric plate (to the deckle) corresponds in principle to printing on non-absorbent material.

The ink transfers from the printing plate to the blanket cylinder plate (deckle) has been found to be.

$$m_i = \alpha(m_f + m_k)\left(1 - e^{-\alpha^2 (m_f + m_k)^2}\right) \tag{4}$$

Transferring ink from the offset plate (from the deckle) to the printed material

$$p = \left(1 - e^{-\alpha_i^2 m_i^2}\right)\left[(1 - \alpha_i)w_{max}\left(1 - e^{-\frac{m_2}{w_{max}}}\right) + \alpha_i m_i\right] \tag{5}$$

Eldar ALIYEV, Isa KHALILOV, Shabnam ISMAILOVA
**Indirect ink transfer for offset printing, taking into account the roughness of the offset
printing plate surface**

Where w_{max} - the maximum possible amount of paint, g/m^2;

α, α_i − separation coefficients of the paint layer.

$$\alpha = \frac{g}{(m_f + m_k) - w}; \alpha_i = \frac{g}{m_i - w} \tag{6}$$

The amount of ink in the free space of the surface roughness of the printing plate in the contact strip can be determined by the formula

$$m_k = \rho V_k \tag{7}$$

where ρ is the ink specific gravity, V_k is the volume of ink in the free space of the surface roughness of the printing plate.

To determine the amount of ink on the printing plate in the contact strip, taking into account the micro geometry of the surface of the printing plate, we use the contact scheme of the printing pair (Figure 2) proposed by the authors [23].
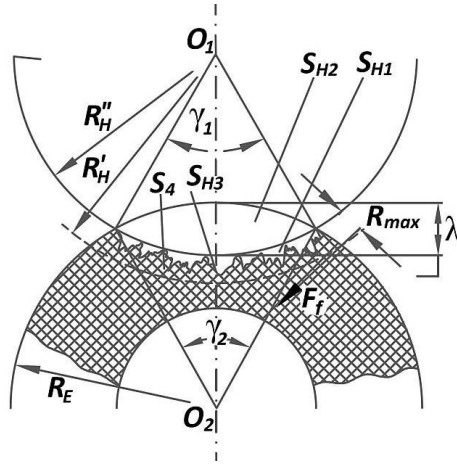
Fig 2. Scheme of contact of the printed pair, taking into account the roughness of the surface of the printing plate

According to this scheme, the volume of free space of the roughness of the printing plate in the contact strip is determined as

$$V_k = S_4 \cdot l \tag{8}$$

Or

$$V_k = \frac{\pi R'_H L}{180°} \gamma_1 \left[\frac{R_{max}(2R'_H - R_{max})}{2R'_H} - R_a \right] \tag{9}$$

Where S_4 − is the free space area of the surface roughness of the printing plate in the contact strip; L − is the contact length along the generatrix of the contacting cylinders; R'_H − the radius of the plate cylinder, taking into account the thickness and roughness of the surface of the printing plate; γ_1 − the central angle of the sector of the contact zone; R_{max} − is the maximum height of micro roughness of the surface of the printing plate; R_a − is the arithmetic mean height of microroughness of the surface of the printing plate.

Taking into account formula (9), formula (7) can be written as:

$$m_k = \frac{\rho \pi R'_H L}{180°} \gamma_1 \left[\frac{R_{max}(2R'_H - R_{max})}{2R'_H} - R_a \right] \tag{10}$$

75

Taking into account (10), formulas (1), (2), (4) and (6) can be written in the following forms:

$$m = m_f + \frac{\rho \pi R_H' L}{180°} \gamma_1 \left[\frac{R_{max}(2R_H' - R_{max})}{2R_H'} - R_a \right] \tag{11}$$

$$v = \frac{m_i}{(m_f - m_i) + \frac{\rho \pi R_H' L}{180°} \gamma_1 \left[\frac{R_{max}(2R_H' - R_{max})}{2R_H'} - R_a \right]} \tag{12}$$

$$m_i = \alpha \left\{ m_f + \frac{\rho \pi R_H' L}{180°} \gamma_1 \left[\frac{R_{max}(2R_H' - R_{max})}{2R_H'} - R_a \right] \right\} \times \left(1 - e^{-\alpha^2 \left\{ m_f + \frac{\rho \pi R_H' L}{180°} \gamma_1 \left[\frac{R_{max}(2R_H' - R_{max})}{2R_H'} - R_a \right] \right\}^2} \right) \tag{13}$$

$$\alpha = \frac{g}{(m_f - w) + \frac{\rho \pi R_H' L}{180°} \gamma_1 \left[\frac{R_{max}(2R_H' - R_{max})}{2R_H'} - R_a \right]} \tag{14}$$

As can be seen from the above formulas, the amount of ink on the printing plate in the contact strip before printing, the separation factor of the ink layer and the transfer of ink from the printing plate to the deckle depend both on the radius of the plate cylinder, the length of the contact, as well as on the angle of contact arc wrapping and the parameters of the micro geometry of the surface of the printing plate.

The presented formulas are valid for plates, and the surface of the printing plate is filled with 100 percent ink. In this case, the filling factor of the form by printing elements is equal to one (k=1), i.e. the nominal surface area as a whole is the printing element. It is known that k is the coefficient of filling the form with printing elements for line images and text k = 0.13-0.15; for raster k = 0.4-0.6; for the plate k = 1 [24]. Taking into account k - the coefficient of filling the form with printing elements, we write the formula (11) in the following form:

$$m = k \left\{ m_f + \frac{\rho \pi R_H' L}{180°} \gamma_1 \left[\frac{R_{max}(2R_H' - R_{max})}{2R_H'} - R_a \right] \right\} \tag{15}$$

Also taking into account the fact that the number of contact strips that can be located on the nominal surface area of the printing plate $k_1 = \frac{B}{b}$, where B is the width of the nominal area of the printing plate and b is the width of the contact strip, we write the formula (15) for the nominal area of the printing plate in the following form:

$$M = kk \left\{ m_f + \frac{\rho \pi R_H' L}{180°} \gamma_1 \left[\frac{R_{max}(2R_H' - R_{max})}{2R_H'} - R_a \right] \right\} \tag{16}$$

Method for assessing the indirect transfer of ink in offset printing, taking into account the surface roughness of the printing plate

To conduct research and make calculations, an offset printing machine Rapida KBA 105 was chosen, which has the following parameters of a printed pair: $R_E = 14,68 sm, R_H = 14,94 sm$ are the radii of the elastic and rigid shafts, respectively. Thickness of deckle brand CONTI-AIR-3,1mm; thickness of the metal printing plate of PRO-V brand from Fujifilm company $\delta_F = 3,1 mm, R_{max} = 2,19 mkm, R_a = 0,317 mkm-$ parameters of the surface roughness of the printing plate, determined from the profilogram taken by the profilometer mod. 130.

Eldar ALIYEV, Isa KHALILOV, Shabnam ISMAILOVA
Indirect ink transfer for offset printing, taking into account the roughness of the offset printing plate surface

Table 1. Examples of calculating the amount of ink transferred to the printing plate

№	Experimentally determined weight of the printing plate without applying ink	Roughness parameters mkm		Estimated weight of the printing plate with ink applied, excluding roughness	Estimated weight of the printing plate with ink applied, taking into account the roughness	Experimentally determined weight of the printing plate with ink application	Difference between values
	M, g	R_a	R_{max}	M_1, g	$M_{2, g}$	M_f, g	$M_f - M_1, g$
1	610	0,317	22,19	615,7	640,1	627,3	11,6
2	607	0,466	22,9	612,7	644,9	638,5	25,8
3	604	0,351	22,72	609,7	636,1	630,4	20,7
4	602	0,414	22,18	607,7	627,7	618,9	11,2
5	599	0,396	22,5	604,7	628,5	619,1	14,4

The amount of ink transferred to the printing plate is determined gravimetrically by calculating the difference between the masses of the printing plate before and after the ink is rolled onto the surface of the printing plate. For this, a sample printer and an analytical electronic balance of the KERN FTB 3Ko.1 model were used. When determining the amount of paint by calculation, the experimental data given in [25] were used as the layer thickness. The calculation results and experimental data are shown in Table 1. The given data show that with an increase in the surface roughness of the printing plate, the amount of ink on the printing plate increases. Based on the results of the research, it can be concluded that the surface roughness of the printing plate really affects the amount of ink transferred to the surface of the printing plate.

Results and discussion. As a result of the research the influence of micro geometry of the printing plate surface on the amount of ink on the printing plate before printing on ink layer separation coefficients and ink transfer from the printing plate to the deckle was established. To investigate the effect of micro geometry on the above parameters, the deepening of micro-roughness of the printing plate surface into the body of the deckle, which leads to additional displacements and deformations of the deckle among other things, is taken into account.

The difference between the values confirms that the surface roughness of the printing plate significantly affects the amount of ink transferred to the surface of the printing plate. The results of experimental studies and their comparison with calculated data show that with an increase in the surface roughness of the printing plate, the amount of ink transferred to the surface of the printing plate before printing increases.

Considering the purpose of the deckle, also the deepening of micro protrusions of the surface roughness of the printing plate into the body of the deckle, it can be said that in the zone of printed contact, the ink layer, located in the free space of the surface roughness of the printing plate, also participates in the transfer and division of ink.

The advantages of this study in comparison with analogues are the following: knowing the parameters of the printing pair and the micro geometry of the surface of the printing plate, it is possible to determine the amount of ink on the printing plate before printing, the separation coefficients of the ink layer and the transfer of ink from the printing plate to the deckle.

The proposed calculation method allows you to determine the amount of ink consumption, predict the quality of printed prints and the runtime of printing forms, as well as correctly set up the printing machine before the printing process.

Conclusions.
1. It has been found that the amount of ink transferred to the surface of the printing plate before printing is largely dependent on the surface roughness of the printing plate.

2. Theoretically determined that with increasing surface roughness of the printing plate, the amount of ink transferred to the surface of the printing plate increases. The results obtained by calculation are confirmed experimentally.

3. It has been established that the deepening of micro protrusions of the surface roughness of the printing plate into the deckle body leads to additional displacements and deformation of the deckle, which perceives part of the ink layer of the roughness of the surface of the printing plate located in the free space.

4. The results of the research show that the proposed methodology for the indirect transition of ink in offset printing differs from existing methods and allows you to determine more accurate values of consumables in the design of printing processes.

REFERENCES

[1]. Tyurin, A.A. *Printing machines are automatic*. Moscow, "Book", 1980, 416 p.

[2]. Germanies, E. *Reference book of a printing technologist*. Moscow, "Book", 1982, 336 p.

[3]. Helmut, K. *Encyclopedia of printed media*. Technologies and methods of production, M.: MGUP, 200, pp. 214-226

[4]. Goryacheva, I.G. *Mechanics of frictional interaction*. M.: Nauka, 2001, 478 p.

[5]. Torskaya, E.V. *Modeling the frictional interaction of a rough indenter and a two-layer elastic half-space* // Physical Mesomechanics, 2012, V.15, No. 2, pp. 31-36.

[6]. Liu, L.L., Li, K.K., Lu, F. *Dynamic Simulation Modeling of Inking System Based on Elastohydrodynamic Lubrication.* International journal of heat and technology. Vol. 34, No. 1, March, 2016, pp. 124-128. https://doi: 10.18280/ijht.340118.

[7]. Tag, C.M, Silfsten, P, Peiponen, K.E, Gane, PAC, Ridgway, C.J. *Impact of fountain solution addition level on tack and optical properties of the print of a mechanically distributed water-in-oil thin film emulsion*. Nordic pulp & paper research journal. Vol: 32. No: 3. https://doi.org/10.3183/NPPRJ-2017-32-03-p436-443.

[8]. Elton, N.J. *Optical measurement of micro roughness of pigment coatings on rough substrates. Measurement science and technology*. Vol: 20. No: 2. 2009 https://doi.org/10.1088/0957-0233/20/2/025303.

[9]. Gigac, J, Kasajova, M, Stankovska, M. *The influence of paper surface energy on multicolor offset print mottling.* Tappi journal. Vol: 13. No: 2. 2014, pp. 55-64. https://doi.org/10.32964/TJ13.2.55.

[10]. Liu, Z., Peng, F., Liu, X. *The Influence of Offset Paper Properties on Printing Effect*. Advanced Materials Research, 2012, Vol: 550-553. 2nd International Conference on Chemical Engineering and Advanced Materials (CEAM 2012) Guangzhou, Peoples R China. pp. 3295-3298.

[11]. Thorman, S., Strom, G., Gane, PAC. *Impact of non-uniform water absorption on water-interference print mottle in offset printing.* Nordic Pulp & Paper Research Journal. Vol: 33. No:1. 2018, pp. 150-163. https://doi.org/10.1515/npprj-2018-3011.

[12]. Cigula, T., Tomasegovic, T., Hudika, T. *Effect of the paper surface properties on the ink transfer parameters in offset printing.* Nordic Pulp & Paper Research Journal, 2019, Vol: 34. No: 4, pp. 540-549. https://doi.org/10.1515/npprj-2019-0018.

[13]. Kusaka, Y., Mizukami, M., Yamaguchi, T., Fukuda, N., Ushijima, H. *Patterning defects in high-speed reverse offset printing: lessons from contact dynamics*. Journal of Micromechanics and Microengineering. 2019, Vol: 29. No: 4, https://doi.org/10.1088/1361-6439/ab024b.

[14]. Pyr'yev, Y. *Analytical solution of thermal conduction in a two-layer cylinder modeling oscillator roller in an offset machine*. International Journal of Thermal Sciences.Vol: 136, 2019, pp. 433-443. https://doi.org/ 10.1016/j.ijthermalsci. 2018. 11.004.

[15]. Khalilov, I.A., Aliev,, E.A., Huseynzadze, E.M. *Influence of the surface roughness of the printing plate on the relative gear ratio of the friction printing pair*. Bulletin of SUSU. Series "Engineering". 2021, V. 21, No. 2, pp. 23–32.

[16]. Hauck, S., Gooran, S. *Automated calibration system in offset printing workflow*. Journal of Print and Media Technology Research. 2018, Vol: 7.No: 3, pp. 115-125. https://doi.org/10.14622/JPMTR-1808

[17]. Cheng, H.C., Chen, Y.W., Chen, W.H., Lu, S.T., Lin, S.M. *Assessing Ink Transfer Performance of Gravure-Offset Fine-Line Circuitry Printing*. Journal of Electronic Materials. 2018, Vol: 47, No: 3, pp. 1832-1846. https://doi.org/10.1007/s11664-017-5967-x

[18]. Varepo, L. G., Trapeznikova, OV., Panichkin, AV., Roev, BA., Kulikov, GB. *Software for Quantitative Estimation of Coefficients of Ink Transfer on the Printed Substrate in Offset Printing*. Metrology, Standardization, Quality: Theory and Practice, (MSQ -2017) International Scientific and Technical Conference on Metrology, Standardization, Quality - Theory and Practice (MSQ) Omsk, Russia Nov 14-16, 2017, Vol. 998. UNSP 012041. https://doi.org/ 10.1088/1742-6596/998/1/012041.

[19]. Panichkin, A.V., Varepo, LG. *The Numerical Calculation of the Viscous Incompressible Fluid Transfer onto Porous Surface Between Rotating Cylinders*. 1st International Multidisciplinary Microscopy Congress (INTERM). Springer Proceedings in Physics. Antalya, TURKEY. Vol: 154. Oct.10-13, 2013, pp. 79-83 https://doi.org/10.1007/978-3-319-04639-6_11.

[20]. Aydemir, C., Yenidogan, S., Karademir, A., Arman, E. *Effects of color mixing components on offset ink and printing process*. Materials and Manufacturing Processes. 2017, Vol. 32. No11, pp. 1310-1315. https://doi.org/10.1080/10426914. 2017.1279323.

[21]. Alm, H.K., Strom, G., Schoelkopf, J., Gane, P. *Ink-lift-offduring offset printing: a novel mechanism behind ink-paper coating adhesion failure*. Journal of Adhesion Science and Technology. 2015, Vol. 29, No.5, pp. 370-391. https://doi.org/10.1080/01694243.2014.989650.

[22]. Aliyev, E.A. *Influence microgeometry offset printing plates for transfer ink from the printing form on dekel*. Proceedings of the International Symposium of Mechanism and Machine Science, 2017, AzCIFToMM-Azerbaijan Technikal University, Baku, Azerbaijan, pp. 201-202.

[23]. Khalilov, I.A., Aliev, E.A., Huseynzadze, E.M. *The phenomenon of ink dusting, taking into account the surface roughness of the offset printing plate*. Problems of conservation of food in Ukraine, 2021, 37(2), pp. 16–24.

[24]. Litunov S.N. *Fundamentals of Printing Processes*. ISBN 978-5-8149-2493-3. Ministry of Education and Science of Russia, OmSTU. - Omsk: OmSTU Publishing House, 2017, 166 p.

[25]. Nechitailo, A.A., Tikhonov, N.T. Shokov, E.V. *Technology of printing processes*, Samara, Publishing house of SSAU, 2013, 168 p.

CONSTRUCTION AND REGULATION OF STATIC CHARACTERISTICS FOR CONTROL OBJECTS

Victor ARTEMYEV [1*], Evgeny NAZOIKIN [2]
Vitaly PANKOV [3]

[1,2]Federal State Budgetary Educational Institution of Higher Education Russian Biotechnological University Moscow, Russia
[3]Moscow University of Industry and Finance, Moscow, Russia

E-mail: artemyevvs@mgupp.ru[1]; NazojjkinEA@mgupp.ru[2]; 9220775959@mail.ru[3]

Abstract: This article discusses the issues of digitalization in stream generation systems, as well as their shortcomings in existing Industrial Ethernet solutions, which were addressed using a new innovative approach. In addition, such solutions are often limited in their flexibility. However, these aspects are becoming increasingly important in the future. Existing control systems are characterized, as a rule, by branched hierarchical structures, and the quality of their functioning is assessed according to vector criteria. Such systems include the national economy as a whole, its branches, industrial enterprises, information systems, targeted programs in various subject and applied areas. It should also be noted that from the point of view of the system approach, any systematization is a fragment of a more general hierarchy of such systems. Automation of control processes and their analysis of modern complex control systems more and more often uses hierarchical models, which makes the problem of their development and research more relevant today. The method proposed by the authors for solving such problems does not seem unnecessarily cumbersome, since it is necessary not only to automate processes at each level, but also to carry out interlevel control. The conclusion is that none of the existing solutions is suitable for meeting the challenges of the future regarding scalability, flexibility or reliability.

Keywords: Resource security, modified protocol, digitalization

Introduction. Already today, the implementation of control issues in the field of automation requires additional specialized equipment to guarantee reliable operation in real time. On the other hand, in P2P networks, the premise of the TDMA-based timeslot method is a single time base for all participating nodes. Therefore, all nodes in the CAD network must be synchronized.

This can be done using the NTP or PTP protocol, or directly in Kad. After running the IDST algorithm and synchronizing all nodes, each node can determine when it is allowed to communicate access to the common Ethernet communication medium [1, 2, 3].

It is recommended that you export the IDST algorithm immediately after the DST algorithm, since only the termination criterion is different and the previous calculations are identical. Thus, it is possible to save a significant part of the time for export [4].

Since the presented approach is intended for automation scenarios, it is necessary not only to guarantee deterministic data exchange between nodes. Rather, it is also necessary to provide real-time behavior of the CAD nodes regarding data processing.

Under these conditions, the chosen form of the target platform must be supported by the real-time operating system. Embedded system was chosen according to the industrial automation use case. The target platform for ZedBoard will be an ARM processor clocked at 680 MHz Avn. With the help of the developed prototype for the digitalization of resource security, it is possible to determine at all times what corresponds to the TDel in relation to the creation, sending, receiving and processing of exchanged UDP packets. Software Stack: As the basis for the software, ZedBoard serves as an ARM-based system. FreeRTOS was chosen as the operating system because it allows tight control of Rea's real-time CAD nodes [5, 6].

In particular, LwIP is used as part of FreeRTOS as a lightweight implementation of the TCP/IP stack to enable communications over Ethernet Free [7]. At the ninth level is the resource security digitization application, which manages media access and thus enables real-time communication through the implementation of time slots. At this level, a new approach is being implemented. At the same time, the digitalization of resource security is understood not only as an application, but also as middleware for other applications that are not related to the digitalization of resource security.

Formulation of problem. After starting other threads, it goes into a waiting state. External control is given second priority in responding to external triggers, such as a human-caused fire alarm. External triggers can also be dedicated lines/devices used to perform highly critical processes such as connected sensors on a digitalization site to further secure our resources. The CAD communication thread has the n-th lower priority and is responsible for processing CAD packets. The following are at most three threads that monitor Kad lookup objects and delete them when the appropriate conditions are met. Because three lookup objects are actively maintained, there can be at most three threads in this regard. The network stream buffers packets from the network interface and forwards them to the application to digitize resource security. Three service flows are responsible for keeping the network up to date. Finally, there is a waiting thread, which serves to generate new threads.

Let's try to find the correlation function $R_{xx}(\tau)$ and the spectral density $S_{xx}(\omega)$ of the variable $x = x_m \sin(\beta t + \varphi)$, if the amplitude is $x_m = 16$ and the angular frequency is $\beta = 1,5 \ c^{-1}$. Find also the variance of this variable from its spectral density.

The correlation function

$$R_{xx}(\tau) = \lim_{T \to \infty} \frac{1}{2T} \int_{-T}^{T} x(t)x(t+\tau)dt. \tag{1}$$

In this case, the function $x(t)$ is periodic, so expression can be replaced by the formula

$$R_{xx}(\tau) = \frac{1}{2T_0} \int_{0}^{T_0} x_m^2 \sin(\beta t + \theta)\sin(\beta t + \beta\tau + \theta)dt = \frac{x_m^2}{2}\cos\beta\tau, \tag{2}$$

where $T_0 = 2\pi / \beta$ — is the period. Substituting th enumerical values, we obtain $R_{xx}(\tau) = 128\cos 1,5\tau$, $R_{xx}(0) = 128$.

The spectral density is determined by the Fourier transform

$$S_{xx}(\omega) = \int_{-\infty}^{\infty} R_{xx}(\tau)e^{-j\omega\tau}d\tau. \tag{3}$$

Taking into account (2), we get

$$S_{xx}(\omega) = \int_{-\infty}^{\infty} \frac{x_m^2}{2}\cos\beta\tau e^{-j\omega\tau}d\tau.$$

The integral in this expression is determined by the equation

$$\int_{-\infty}^{\infty} \frac{x_m^2}{2}\cos\beta\tau e^{-j\omega\tau}d\tau = \pi[\delta(\omega-\beta)+\delta(\omega+\beta)],$$

where $\delta(\omega-\beta)$ and $\delta(\omega+\beta)$ — are shifted δ-functions dependent on the frequency of ω.

Therefore,

$$S_{xx}(\omega) = \frac{\pi x_m^2}{2}[\delta(\omega-\beta)+\delta(\omega+\beta)], \tag{4}$$

i.e., the spectral density of the harmonic variable $x = x_m \sin(\beta t + \varphi)$ represents two infinitely short pulses located at frequencies $\omega_1 = -\beta$ and $\omega_2 = \beta$, the area of each of which is equal to $\pi x_m^2 / 2$.

The variance of some quantity $x(t)$ with spectral density $S_{xx}(\omega)$ can be determined by the formula:

$$D_x = \frac{1}{2\pi} \int_{-\infty}^{\infty} S_{xx}(\omega) d\omega. \tag{5}$$

Therefore, in this case

$$D_x = \frac{1}{2\pi} \int_{-\infty}^{\infty} \frac{\pi x_m^2}{2} [\delta(\omega - \beta) + \delta(\omega + \beta)] d\omega = \frac{x_m^2}{2} \int_{0}^{\infty} [\delta(\omega - \beta)] d\omega = \frac{x_m^2}{2},$$

since the integral of the δ-function is 1. By substituting numerical values, we obtain $D_x = 256/2 = 128$.

Comparing with the value of $R_{xx}(0)$, we conclude $D_x = R_{xx}(0)$.

A random stationary process $\varphi(t)$ has spectral density $S_{\varphi\varphi}(\omega)$. Calculate its mean value $\bar{\varphi}$, variance D_φ and correlation function $R_{\varphi\varphi}(\tau)$.

Since $S_{\varphi\varphi}(\omega)$ of a given process does not contain the δ-function $\delta(\omega)$ at $\omega = 0$, the average value $\bar{\varphi} = 0$. Therefore, the variance D_φ is equal to the mean square of the random process, i.e., $D_\varphi = \sigma_\varphi^2$, where σ_φ is the standard deviation of the process $\varphi(t)$. On the contrary, according to formula (3.59), we have:

$$D_\varphi = \frac{1}{2\pi} \int_{-\omega_n}^{\omega_n} N d\omega = \frac{N}{2\pi}(\omega_n - (-\omega_n)) = \frac{N\Delta\omega_\varphi}{2\pi}, \tag{6}$$

where $\Delta\omega_\varphi = 2\omega_n$ — is the angular frequency band (in radians/s) of the random process $\varphi(t)$. The formula (6) can be written as follows:

$$D_\varphi = N\Delta f_\varphi, \tag{7}$$

where $\Delta f_\varphi = \Delta\omega_\varphi / 2\pi$ is the bandwidth in hertz of the random process in $\varphi(t)$.

Let us find the correlation function $R_{\varphi\varphi}(\tau)$ by the formula

$$R_{\varphi\varphi}(\tau) = \frac{1}{2\pi} \int_{-\infty}^{\infty} S_{\varphi\varphi}(\omega) e^{-j\omega\tau} d\omega = \frac{1}{\pi} \int_{0}^{\infty} S_{\varphi\varphi}(\omega) \cos \omega\tau d\omega$$

Or

$$R_{\varphi\varphi}(\tau) = \frac{1}{\pi} \int_{0}^{\omega_n} N \cos \omega\tau d\omega = \frac{N}{\pi\tau} \sin \omega_n \tau.$$

Therefore, we once again have

$$R_{\varphi\varphi}(0) = \lim_{\tau \to 0} \frac{N\omega_n}{\pi} \frac{\sin \omega_n\tau}{\omega_n\tau} = \frac{N\omega_n}{\pi} = D_\varphi,$$

Time τ_1 is defined by the equality $\sin \omega_n\tau_1 = 0$, i.e., $\tau_1 = \pi / \omega_n$. As can be seen, at $\omega_n \to \infty$ the amplitude of the correlation function $R_{\varphi\varphi}(0) \to \infty$ and the time $\tau_1 \to 0$, i.e. the correlation function $R_{\varphi\varphi}(\tau)$ tends to the δ-function, which corresponds to the white noise correlation function.

Analysis of the obtained results. The use of a modified Kademlia protocol and real-time CAD nodes enables the creation of demanding real-time applications based on P2P technology.

To determine the performance of the system, it is necessary to prototype the scenario using the resource security digitalization nodes. The two nodes accurately represent a discrete period of the time interval during which they have exclusive access to the media. Thus, it can be concluded that of the NSLOT time slots, two instances per discrete time slot are best suited for the entire system. Thus, all n different parameters can be defined. This setup supports two operations between two flanges. These are read and write operations that can be performed in a resource security digitalization application.

When the user performs a read operation, a series of integer values is requested. The number of values is specified by the user in the UserRequest packet. It also specifies the hash value of the node that should provide the cumulative values. The first ZedBoard accepts and processes a batch of user requests. Because the first ZedBoard is not designed for a read request, it searches the Kad network for the node that, according to the hash value in the user's request packet, is responsible for the request request. Therefore, the first ZedBoard communicates with the second one with a kad request, because it is designed for requests, and checks if this node exists [8].

The second ZedBoard responds with a Kad response package. When the first ZedBoard receives the Kad response packet, it can contact the second board again and perform a read action. The action is performed using an action request packet, which in this case is a read request packet. After receiving the first Read Action Response Packet, ZedBoard sends the integer values to the user using the User Response Packet.

When performing a write operation, a number of integer values are passed in the user request packet. As with the read operation described earlier, the Kad network searches for the responsible node for the write operation. In this case, it is also the second ZedBoard. It will now receive an action request packet, which is a record action request packet from the first ZedBoard. The package includes integer values that will be stored on the second ZedBoard. The second ZedBoard sends a Write Action Response packet as an acknowledgment in uck, which is transmitted from the first ZedBoard to the user as a user response packet [9, 10].

Time was measured for both operations, including cad operations and packet processing. The first measurement point is taken when the first ZedBoard receives a packet of user requests. The second time value is received when the user response packet is sent back to the PC. Clearly, results can be achieved in less than a millisecond. In addition, there is a linear behavior depending on the amount of requested and unsolicited data, respectively, to recognize integer data values.

The use of business intelligence software today often makes the difference between winners and losers. The existing industry in software methods uses analytics to monitor and optimize all aspects of their operations - from marketing to the supply chain - in real time. They rely on analytics to make fast, data-driven decisions, drive revenue growth, develop new business models, deliver best-in-class customer service, support employees, gain a competitive edge, and more. Economics in software methods without analytics - or without good analytics - are forced to make decisions based solely on intuition and experience.

This growth has been accelerated by issues of digitalization, which has forced many existing solutions to explore new business opportunities, cut costs and navigate the turbulent "new normal". Analytics, business intelligence and data science are the most common use cases, which have become even more important as a result of the pandemic, overtaking the Internet of things and cloud applications. Problem-solving capabilities and predictive analytics are helping organizations address urgent pandemic-related challenges, such as accurately forecasting demand, protecting vulnerable workers, and identifying potential supply chain disruptions.

This simple form of analysis uses basic mathematical calculations such as averages and percentage changes to show what has already happened in our sector. Descriptive analysis, also known as business intelligence, is the first step in the analysis process and serves as a starting point for further research.

But continuing the descriptive analysis, identifying, examining and correlations between the available data in order to get to their essence and determine the causes of events and behavior.

This advanced analysis sub-discipline uses the results of descriptive and diagnostic analysis—along with sophisticated predictive models, machine learning, and deep learning techniques—to predict what will happen next.

This modern form of analysis is based on the results of descriptive, diagnostic and predictive analysis and uses modern tools and methods to assess the impact of possible solutions and determine the best course of action in a situation.

Business intelligence includes many different components and tools. The most common components include:

Data aggregation: Before data can be analyzed, it must be collected, organized and cleaned from many different sources. A solid data management strategy and a modern data warehouse are essential for analytics.

Data mining uses statistical analysis and machine learning algorithms to search large databases, analyze data from different angles, and look for previously unknown trends, patterns, and relationships.

Big data analytics uses sophisticated techniques such as data mining, predictive analytics, and machine learning to analyze large amounts of structured and unstructured data in databases, data warehouses, and Hadoop systems.

Text mining examines unstructured text datasets such as documents, emails, social media posts, blog posts, call center scripts, and other text sources for qualitative and quantitative analysis.

Data visualization and storytelling: With data visualizations such as charts and graphs, trends, outliers, and patterns in data can be better captured and made understandable. These visualizations, taken together in context, can provide a more complete picture and support decision making.

Conclusion. Analytics are used by companies of all sizes in all industries – retailers, healthcare, and even sports clubs. Many analytics solutions are tailored to a specific industry, purpose, or business area.

The explosive growth of e-commerce, increasing market volatility, globalization and other factors have made supply chains even more complex. With supply chain analytics, companies can prevent supply disruptions, ensure a steady flow of goods, and optimize supply chain stability and agility. They use real-time data from various sources such as IoT sensors to optimize everything from purchasing to manufacturing and inventory to transport and logistics.

The results are TDel, which corresponds to the creation of the search object, the search phase, and the exchange of integer values. These results can be used for further consideration.

REFERENCES

[1]. Artemyev, V.S., Klementyev, A.J., Kusjakov, A.S. *Techno-economic reasoning of recycled energy resources introduction*, Federal State Budgetary Education Institution of Higher Professional Education "Chuvash State Agricultural Academy", Cheboksary, October 20–21, 2015. - Cheboksary: Chuvash State Agricultural Academy, 2015, pp. 567-571.– EDN WBVFGT.

[2]. Alekseev, V.A., Artemyev, V.S., Kolosov, S.P. *Increasing competitiveness of industrial enterprises by reducing costs on power energy production,* Automation and IT in the energy sector. 2017, № 4(93), pp. 46-52. – EDN YITOXV.

[3]. Belova, N.N., Belov, V.V., Artemyev, V.S. *Modern CAD systems in the agro-industrial complex*, Scientific, educational and applied aspects of production and processing of agricultural products: Collection of materials of the International scientific and practical conference dedicated to the 20th anniversary of the first graduation of agricultural production technologists, Cheboksary, November 15, 2018. - Cheboksary: Chuvash State Agricultural Academy, 2018, pp. 394-399. – EDN MKNHVB.

[4]. Artemyev, V.S., Zakharov, A.Y. *Implementation of unified energy centers for single-industry towns*, Progressive technologies and processes: Collection of scientific articles of the 2nd International

Youth Scientific and Practical Conference: in 3 volumes, Kursk, September 24–25, 2015, Managing editor: Gorokhov A.A .. - Kursk: Closed Joint Stock Company "University book", 2015, pp. 73-77. – EDN UKGHOH.

[5]. Artemyev, V.S. *Reconstruction of the energy facilities of the cities of the Republic*, Young researchers of the agro-industrial and forestry complexes - to the regions: II International Youth Scientific and Practical Conference, Vologda-Molochnoe, April 27, 2017. – Vologda-Dairy: Vologda State Dairy Academy named after V.I. N.V. Vereshchagin, 2017, pp. 8-14. – EDN YTMSAB.

[6]. Alekseev, V.A., Artemyev, V.S., Kolosov S.P. *Prospects and ways of introduction of energy-saving technology in agriculture* / Scientific and educational environment as the basis for the development of the agro-industrial complex and the social infrastructure of the village: materials of the international scientific and practical conference (dedicated to the 85th anniversary of the Chuvash State Agricultural Academy), Cheboksary, October 20–21, 2016,– Federal State Budgetary Education Institution of Higher Education «Chuvash State Agricultural Academy». pp. 366-370. – EDN XBZLQD.

[7]. Mokrushin, S.A. *Sterilization process control system based on PLC*, Natural and technical sciences. - M .: Publishing house "Sputnik +", 2010- №4 (48), pp.309-314.

[8]. Mokrushin, S.A., Khoroshavin, V.S., Filatova, E.S., Rusyaeva, T.L. *Management of processes of thermal processing of foodstuffs* // Modern problems of science and education. 2012, №6;

URL: http://www.science-education.ru/106-7935

[9]. Mokrushin, S.A., Okhapkin, S.I., Khoroshavin, V.S. *Study of the process of sterilization of canned food for the purpose of further automation*. Scientific journal NRU ITMO. Series "Processes and apparatuses of food production". 2015, №4, pp. 62–72.

[10]. Mokrushin, S.A., Okhapkin, S.I., Moskvin, E.V. *Features of building a control system for the process of thermal processing of food products in autoclaves*, Izvestiya SPb ETU. Thematic direction "Automation and control". - St. Petersburg: Publishing house of St. Petersburg Electrotechnical University "LETI", 2015 - №10, pp. 45–49.

SUBMISSION GUIDELINES

General requirements.
Article should not be earlier published in any edition, stated in the short form and edited. The scientific article maintenance should correspond to one of the following scientific directions: Designing of machines; Materials technology; Mechanics; Manufacturing engineering; Economy and management; Automatics and ICT; Technical information.

The documents applied to article.
The conclusion of the corresponding organization (chair, etc.); The expert opinion on expediency of the publication of the article; The covering letter; The Information on the authors (name, patronymic, surname, the exact address, place of work and position, scientific degree, area of scientific activity, contact phones, e-mail address ,etc.).

Preparation rules.
Format - A4; *Margins from each party* - 20 mm; *Program* - Microsoft Office Word; *Font* - Times New Roman, a font size - 12, an interval - 1.
The scientific article can be written only in English language, and it is represented in duplicate.
 Article volume - 5 … 8 pages.

Sequence of compilation:
1. Article name - on the center;
2. Names and surnames of the authors - on the center;
3. Full addresses of a place of work of authors - on the center;
4. Co-ordinates of authors: e-mail address, phone numbers.
5. The abstract: not less than two-three offers, and no more than 100 words. In the summary: article summary, problem statement, and the information on the received results should be reflected.
6. Keywords: often used $3 \div 5$ terms under the article.
7. The basic text.
8. The references.

The main text of article should be divided as follows:
For example: "*Introduction*", "*Problem statement*", "*Decision or test methods*", "*Results of the decision or tests and their estimation*".
In introduction: the description of the problem statement, the work purpose and etc.;
In the main part: formation of problem statements; research and methods of the decision, their advantage and difference from existing methods; examples confirming efficiency of the offered method of the decision and the results received.
In the conclusion: evaluation of the results.
Drawings. *Formats* - DOC, JPEG, TIFF and PDF (600 dpi). *The size* – min. 5×5, max. 10×15. *Arrangement* - ("In the text", in the center). Images of drawings should be accurately visible, and all symbols well are read.
Drawings, paintings, schedules and algorithms should correspond to standard requirements.
Tables are located in the text and are numbered, and the name of each table should be specified in the right top corner.
Formulas should be written down in format *Equation* in the separate line. It is not recommended to use special symbols in the text written on the same line in format *Equation*. Formulas should be written down in certain sequence and are numbered on the right.
The references should correspond to the text and sequence of article. It is recommended to refer to sources published in last 10 years.
The additional information. Edition has the right to spend necessary updating and reductions. Authors bear a scientific article maintenance responsibility. To the publication those articles which have received a positive response are represented only. If article is not published, the edition decision is possible to data of authors, the manuscript and disks do not come back.

MACHINE SCIENCE № 2, 2022